Dissertation
submitted to the
Combined Faculties for the Natural Sciences and for Mathematics
of the Ruperto-Carola University of Heidelberg, Germany
for the degree of
Doctor of Natural Sciences

presented by

Diplom-Phys.:	Nikolai Kryzhevoi
born in:	Furmanov, Russia

Oral examination: 31st October, 2001

Perturbation Approach for the Radiative Transfer Equation for 3D Moving Media and Application to Accretion Disks

Referees: Prof. Dr. Rainer Wehrse
Prof. Dr. Rolf Rannacher

Störungstheoretische Behandlung der Strahlungstransportgleichung in dreidimensionalen, bewegten Medien und Anwendung auf Akkretionsscheiben

Die mehrdimensionale Strahlungstransportgleichung wird mit Hilfe einer störungstheoretischen Methode gelöst, wobei sich die vollständige Lösung durch eine Reihe von 1D Lösungen ergibt. Da die Lösungen von Störungen höherer Ordnung explizit angegeben werden können und die Verfahren, die für die Lösung der Gleichung 0. Ordnung verwendet werden, größtenteils analytisch sind, ist der entsprechende Code effizienter als gewöhnliche mehrdimensionale Strahlungstransportprogramme. Um den dabei involvierten iterativen Prozeß zu untersuchen, wird das Strahlungsfeld einer geometrisch dünnen, langsam rotierenden Akkretionsscheibe berechnet. Die Methode stellt eine Verbesserung gegenüber solchen Methoden dar, die die Akkretionsscheibe als ein System von unabhängigen Ringen betrachtet, da die Wechselwirkung der Ringe bei den Störungen höherer Ordnung berücksichtigt wird. Der Einfluß von radialen Gradienten, Geschwindigkeitsfeldern u.a. auf das Linienprofil wird diskutiert.

Desweiteren wird unter der Annahme der Zwei-Strom-Näherung, die analytische Lösung der planparallelen Strahlungstransportgleichung für eine Vielzahl von Verteilungen des Abregungskoeffizienten ϵ gefunden. Eine neue Methode für die Lösung dieser Gleichung mit stochastisch verteiltem ϵ wird vorgeschlagen. Außerdem erlaubt uns eine verbesserte Separationsmethode ("separable approximation"), die Lösung der planparallelen Strahlungstransportgleichung ohne Winkel- und Raumdiskretisierung schnell und genau zu finden.

Perturbation approach for the radiative transfer equation for 3D moving media and application to accretion disks

The multidimensional radiative transfer equation is solved by means of a perturbation approach in which the full solution is represented by a sequence of 1D solutions. Since the solutions of the higher perturbation orders are given explicitly, and the methods used for the solution of the zero order equation are largely analytical, the corresponding code is more efficient than general multidimensional radiative transfer codes. To examine this iterative procedure the radiation field of a geometrically thin slowly rotating accretion disk is calculated. The method is the improvement of those methods which treat the accretion disk as a system of independent rings because the interaction of the rings is taken into account in the higher perturbation orders. The influences of radial gradients, velocity field etc. on the line profile are discussed.

Furthermore, under assumption of the two-stream approximation the analytical solution of the plane-parallel radiative transfer equation is found for a large variety of the internal distribution of the de-excitation coefficient ε. A new method for the solution of the equation with the stochastic ε is proposed. In addition, an improved separable approximation method enable us to obtain fast and accurate solution of the basic plane-parallel radiative transfer equation without angle and space discretization.

Contents

1 Introduction **1**

1.1 Accretion disks 1

1.2 Multidimensional radiative transfer equation 4

1.3 Why the perturbation approach ? 6

2 Basic notions **9**

2.1 Radiation 9

2.1.1 Specific intensity and its moments 9

2.1.2 Radiation – matter interaction 10

2.2 Radiative Transfer Equation 11

2.2.1 Transport along a ray in a static medium 11

2.2.2 Radiative transfer equation in a rotating disk. 12

3 Perturbation approach **15**

3.1 Applicability 15

3.2 Perturbation equations 16

3.3 Zero order 16

3.4 First order 17

3.5 Second order 18

4 Two-stream approximation **19**

4.1 Constant ε 20

4.1.1 Matrix form of the transfer equation and its solution . 20

4.1.2 Limit of large optical depth 25

4.1.3 Isothermal media 25

4.2 Depth-dependent $\varepsilon(\tau)$ 28

4.2.1 General solution 28

4.2.2 Examples 30

4.2.3 Diagnostics of $\varepsilon(\tau)$ 33

4.2.4 Stochastic ε 35

5 Separable approximation **41**
5.1 Basic equations 42
5.2 Evaluation of the matrix elements 44
5.3 Separable representation of the solution 47
5.4 Efficiency of the method 50

6 Results **55**
6.1 Homogeneous accretion disk 55
6.2 General case 62

7 Discussion and conclusions **75**

A Solution of equation (4.39) **79**

B Approximation of $E(t)$ **83**
B.1 Stieltjes-Markov method 83
B.2 "Points method" 85

Chapter 1

Introduction

1.1 Accretion disks

Accretion disks are ubiquitous in the Universe (cf. Meyer et al. 1989). They are believed to provide the source of radiation of many objects, ranging from active galactic nuclei (AGN), cataclysmic variables (CV) to young pre-main sequence stars (T Tauri type stars). Therefore, studying accretion disks is very important in many branches of modern astrophysics.

The best studied accretion disk objects are low-mass binaries which are systems composed typically of a compact degenerate object (white dwarf in the case of dwarf novae and novalike variables; or a neutron star or a black hole (Fig. 1.1) in the case of low-mass X-ray binary systems) and a late-type star filling its Roche lobe. The matter lost by the companion star via Roche lobe overflow is captured in the gravitational field of the compact object. Because of an excess of angular momentum it is not immediately accreted on the compact star, but rather forms an accretion disk. Viscosity operates in the disk and transports the angular momentum outwards. The nature of viscosity, one of the most important problem in the theory of accretion disks, is not discussed in the framework of this thesis.

One of the most direct methods of detecting an accretion disks is to observe the line profiles produced by it. An obvious feature is double-peaked profiles (Fig. 1.2). They are produced by separate rings of gas rotating, as assumed of many of the authors, with Keplerian velocities around a compact object. The rings closer to the central object have higher velocities and contribute to the outer wings of the profile, whereas those at large radii move slowly and form the bulk of the line core. The velocities of the outer rings largely determines the separation of the peaks. A central dip occurs because of gas having zero radial velocity.

An accretion disk is a complicated 3D structure and strictly speaking should be treated as such. However this is a difficult task. The problem may

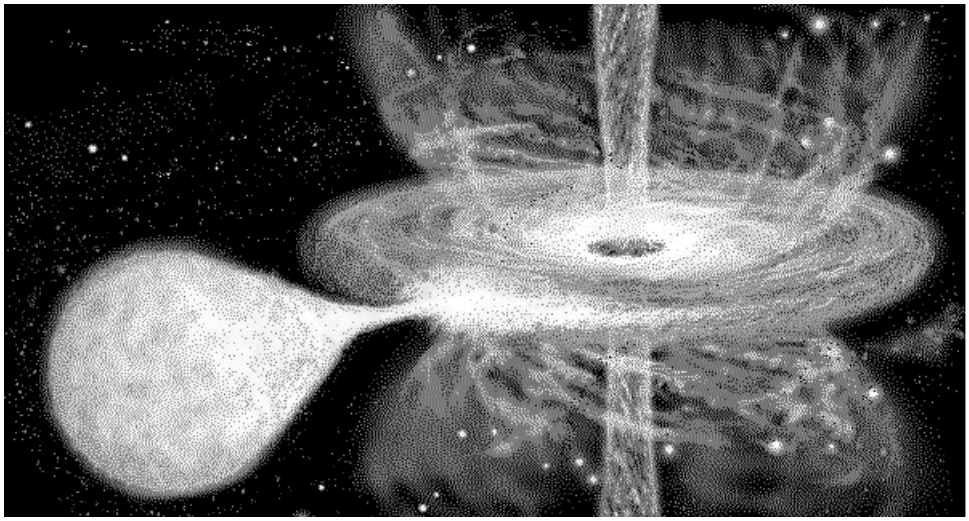

Fig. 1.1: Artist's concept of the view of an accretion disk around a black hole.

be significantly simplified by disentangling the radial and vertical structure. This approximation is possible because for many disks of astrophysical interest the radial extent of the disk is larger than the vertical one. In other words, the disk is geometrically thin. Therefore models are constructed as an at least two-step process. First, assuming a vertically homogeneous structure and axial symmetry the problem is reduced to 1D problem in the radial direction. Solving simultaneously equation of continuity, angular momentum balance and energy balance one can in principle determine the total column mass, angular and radial velocities and the total dissipated energy as a function of radius (Shakura & Sunyaev 1973; Frank et al. 1992).

In order to get the radiation spectrum of a disk authors of early works (Shakura & Sunyaev 1973; Bath et al. 1974) simply assumed that each point of the disk at radius r radiates as a blackbody with the temperature $T_{\rm eff}(r)$. The radiation from the whole disk is obtained by integrating the local spectrum. Needless to say, agreement between these models and data was very rough at best. The disk spectra modeled in such a way generally do not show observed power-law behavior. The radiation from a blackbody has neither spectral features nor any angular dependence.

There was a subsequent era in which sums of stellar spectra were taken to represent the disk spectrum. The pioneering works by Schwarzenberg-Czerny & Rozyczka (1977) and Kiplinger (1979, 1980) used existing model stellar spectra from a variety of sources. Later Wade (1984) used available grids of model stellar spectra by Kurucz (1979) for the modeling of an optically thick disk. However the Kurucz model grid did not extend to the high gravities predicted for the inner parts of CV disks, and its maximum temperature was

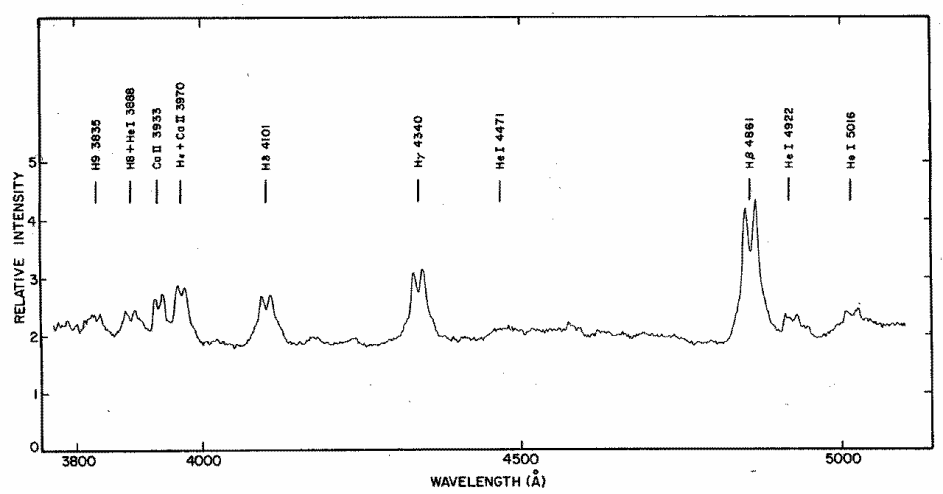

Fig. 1.2: Spectrum of U Gem (from Stover 1981).

only 50,000 K. In the models by Herter et al. (1979), Mayo et al. (1980) and la Dous (1989) approximate atmospheres were used which were calculated directly and not interpolated from a grid. While the match of models to observed disk spectra was improved, important details such as the size of the Balmer jump or the slope of the Balmer continuum were often still far from agreement (Wade 1984, 1988).

Objections to using standard stellar atmospheres to model the local spectra of the disk surface include the following. The gravitational acceleration in the disk is not constant with depth. Instead it can change significantly, especially in the optically thin parts of the disk. The disk is not a semi-infinite atmosphere but rather its optical depth is finite and not *a priori* known. The geometry of the disk is neither plane-parallel nor spherical. The radiative flux cannot be treated as constant with depth since there is an energy generation in the disk due to dissipation which converts the orbital kinetic energy into heat.

The next category of simple approaches comprises models constructed assuming optically thin, vertically homogeneous disks. The emergent spectrum is again calculated rather easily, because the optically thin approximation enables one to write analytical expressions for the emergent flux (Williams 1980; Tylenda 1981; Williams & Ferguson 1982).

The models of the accretion disk were continuously modified and improved by several authors to include shear broadening (Horne & Marsh 1986; Hummel & Vrancken 2000), line broadening due to the Stark effect (Lin et al. 1988), disk winds (Murray & Chiang 1996) and NLTE effects (Williams & Shipman 1988).

Some phenomena cannot be explained in the framework of the traditional Keplerian disk models. Thus a new model of the accretion disk – advection-dominated disks – was proposed by several authors (e.g. Narayan & Yi 1994; Chen 1995). In such a new optically thin disk the viscously dissipated energy is stored as entropy and advected inward rather than being radiated. In some cases the rotational velocity becomes considerably less than the Keplerian one and the radial infall velocity cannot be neglected.

Attempts to solve more self-consistently the vertical structure and the emergent spectrum of the disk were done in the new generation of models. Meyer & Meyer-Hofmeister (1982), Cannizzo & Wheeler (1984), Cannizzo & Cameron (1988) calculated the vertical structure of the disk in the diffusion approximation but without treating the radiation field in detail. Although these models are important for the understanding of the formation and evolution of the accretion disks, they are still not satisfactory because the diffusion approximation provides an acceptable description of the radiation field only at large optical depths but not at upper layers of the disk atmosphere where the spectra originate.

The self-consistent treatment of the radiative transfer equation is necessary on the way towards the satisfactory solution. Kříž & Hubeny (1986) and Adam et al. (1988) have done it in the models of grey disks. The continuum radiation of the accretion disk was calculated by Shaviv & Wehrse (1991) self-consistently under assumption of the two-stream approximation. Using a model of the vertical structure El-Khoury & Wickramasinghe (2000) presented a grid of model disk spectra for the helium-rich AM CVn cataclysmic variables. They calculated the vertical structure of the disk in the grey two-stream approximation as in Adam et al. (1988) but with the rays inclined at a certain angle. This new generation of models overcomes many of the problem associated with applying stellar atmosphere models where they are not appropriate. Although self-consistent models certainly represent an improvement (e.g. very good agreement with the observational spectra was found in Shaviv & Wehrse (1991) and El-Khoury & Wickramasinghe (2000)), the situation is still far from being satisfactory. Many approximations and uncertainties remain even in these models.

1.2 Multidimensional radiative transfer equation

One of the uncertainties that remains in all mentioned models is the decoupling of the radial and vertical structures of the disk. It is obvious that the consideration of the disk as a system of non-interacting rings is unphysical and leads to inaccuracies in the final solution. The problem can, in princi-

pal, be overcome by applying fully multidimensional calculations. However, it is not clear whether even the most sophisticated 3D models which still treat viscosity by means of various ad hoc parameters would be more than a mathematical exercise.

Methods for the solution of a multidimensional radiative transfer equation roughly fall in one of three categories: Monte Carlo methods, Discrete Ordinate methods and Angular Moment methods. Monte Carlo codes are very flexible and can be used for a large variety of problems in multidimensional geometries (cf. Wood et al. 1996; Wolf et al. 1999; Schultz 2000). Such methods perform well at low to medium optical depths but at high optical depths they converge very slowly. Because the random error of the results is approximately inversely proportional to the square root of the number of simulated photons, Monte Carlo simulations are always very time consuming.

Angular Moment methods, on the other hand, are very well suited to treat the high optical depths regime because many of them are related to the diffusion equation (Spagna, Jr. & Leung 1987; Sonnhalter et al. 1995). However, it is not surprising that they fail at low optical depths, since the diffusion approximation was never meant for this regime. In order to treat the problem also at low optical depth the variable Eddington factor approach (Auer & Mihalas 1970) can be used. However, the computational effort due to the generalization of this approach to the multidimensional problem appears to be huge and only a few calculations with this code have been published (Klein et al. 1989; Menshchikov & Henning 1997).

In the Discrete Ordinate approach the photon propagation direction is discretized. A classical method is the application of simple trapezoidal or quadrature rules to evaluate the integral operator for each of the two describing angles separately (Adam 1990; Stenholm et al. 1991). Since the nodes are concentrated toward the poles this grid is usually not adapted to the physical problems. It is therefore desirable to have equally distributed nodes on the unit sphere. Such a discretization of the integral operator was used by Steinacher et al. (1997), Maier (1994) and in the Finite Element method (Kanschat (1996), see also Schrage (1999) for application to accretion disks).

For spatial discretization the Finite Difference method can be used (Stenholm et al. 1991). Another way for the computation of the specific intensity at every point is the Short Characteristics method (Väth 1994; Papkalla 1995). The structure of the resulting numerical scheme is very simple but the flexibility for treating complex geometries is lost. For unstructured grids and complex geometries the Finite Element method is well suited instead.

The discretization of the multidimensional radiative transfer equation results in a very large linear system of equations which is usually solved by means of Λ–iteration method (cf. Mihalas 1978). Its serious disadvantage is a very slow convergence if the optical depth and/or a scattering fraction

is large. To improve the rate of convergence the Approximated Λ–iteration method can be applyed. This is essentially the Jacobi or block Jacobi iteration depending on the form of the approximate operator. There are additional ways of accelerating the convergence. They are Ng method (Ng 1974; Olson et al. 1986), orthomin (Vinsome 1976; Klein et al. 1989) and Bi-CGSTAB (van der Vorst 1992; Turek 1993).

1.3 Why the perturbation approach ?

Despite the relative efficiency of the mentioned multidimensional radiative transfer codes, they have not yet been combined self-consistently with the hydrostatic and energy equations. It is very difficult to do this on the present computers both because the size of the problem exhausts the memory space, and because such computations would require far too much computing time. However, further developments in this direction are in progress since this is, probably, the only way to get an accurate solution in systems with a complex geometry.

In general, the accretion disk is such a system. But in those disks which are geometrically thin the variations in the radial directions are usually small relative to the vertical ones and evidently can be treated as perturbations. In such situations, the perturbation approach seems to be the most appropriate method for the calculation of the vertical structure and spectra of the accretion disks. The solutions of the existing self-consistent models can be regarded as the basis for the zero order of the perturbation theory, whereas the radial gradients, shear broadening etc. which were ignored in these models so far can be taken into account in the higher orders of this approach. Certainly, such a sequence of 1D calculations requires additional computing resources but still remains computationally much cheaper than the codes involving solution of the general 3D radiative transfer equation. The efficiency of such an approach depends both on how many perturbation orders are considered, and how effective the method for the solution of the plane-parallel radiative transfer equation is. The development of such a perturbation approach for the radiative transfer equation for the subsequent application to a geometrically thin, slowly rotating accretion disk is the aim of this thesis.

The methods for the solution of the plane-parallel radiative transfer equation are rather well developed and there exists a vast literature on this topic (see e.g. Chandrasekhar 1950; Mihalas 1978; Cannon 1985; Kalkofen 1984, 1987).

One should bear in mind that although the total optical depth of the disk may be very large, the spectra originate only in the thin surface layer. Coupled with the complex disk shape this may lead to the extremely large number of grid points necessary for the adequate description of the prob-

lem. In such cases either a clever choice of the grid points or the local grid refinement methods must be used for the derivation of the fast solution.

The most preferable methods are those which proceed analytically and are less CPU-time and memory consuming. The two-stream approximation method referred to such class of methods. In spite of the serious simplification, one can obtain results with reasonable accuracy. The problem with the varying de-excitation coefficient ε (see Chapter 2 for definition) could be solved only numerically so far. Now it becomes analytically solvable for a large variety of the internal distributions of the de-excitation coefficient.

Chandrasekhar (1950) considered more than two beams in his analytical approach. It was found that the exact solution of the radiative transfer equation in semi-infinite atmospheres leads to closed expressions for the angular distribution of the emergent radiation, involving a so-called H-function that is the solution of an integral equation of standard form. In media of finite optical depth the emergent radiation can be expressed in terms of certain rational functions X and Y which satisfy integral equations too. The method is not much in use because the Chandrasekhar functions H, X and Y are difficult to calculate in spite of the different methods proposed (Caldwell & Perks 1981; Bosma & de Rooij 1983; Haggag & Machali 1985; Haggag et al. 1989). In addition, it does not provide the distribution of the specific intensity with depth that is required in models of astrophysical objects.

In this thesis the separable approximation method by Efimov et al. (1995, 1997) is applied to the solution of the plane-parallel radiative transfer equation. By introducing the intensities in outward and inward directions the transfer equation can be written in a matrix form. The involved matrix M is an operator in an infinite dimensional space and possesses rather unpleasant properties, in particular, its spectrum extends from $-\infty$ to ∞. In spite of this, the transport operator can be expressed in terms of the hyperbolic tangent function of the matrix M. Note that this function is bounded and therefore no difficulties arise related to the infinite spectrum of M. The successive application of the formalism of meromorphic functions as well as Krein's formula for the finding of inverse operators leads to the exact solution represented in a form of infinite series. Because of their very slow convergence these results are not well suited for numerical work. Therefore an appropriate approximation of the infinite sums by finite ones is recommended. In such a matter the angular distribution of the emergent intensity was only found in the lowest approximation order.

The further development of the method is presented in the thesis. For the slab of finite optical depth with the symmetry plane we obtain both the angle and depth distributions of the specific intensity, i.e. the total solution of the radiative transfer equation. In order to get more precise results additional approximation orders are considered which are defined by

the number of terms in the finite sums approximating the infinite series. The comparison with the solutions obtained by means of other methods shows that highly precise results can be achieved for a wide range of parameters in low approximation orders.

The thesis is arranged as follows. In Chapter 2 we give definitions of quantities used in the radiative transfer theory, discuss the choice of the coordinate system and the reference frame. In Chapter 3 we describe the basic concept of the perturbation approach. We obtain the perturbation equations in the zero, first and second orders of the perturbation theory and give the solutions of the first and second order equations. Next two chapters are dedicated to the solution of the zero order equation, plane-parallel radiative transfer equation with isotropic coherent scattering. In Chapter 4 we solve this problem under assumption of the two-stream approximation. The separable approximation method is used in Chapter 5. Chapter 6 presents results of our calculations. Finally, in Chapter 7 the results are discussed, and conclusions drawn.

Chapter 2

Basic notions

In the present chapter we shall present the basic notions, definitions of the radiative quantities, abbreviations etc. used throughout the thesis. They are mostly taken from Mihalas (1978). We shall use a special form of the radiative transfer equation, the basic equation describing the interaction of the radiation field with matter, which is more suitable for our needs. Here, special attention will be paid to the choice of the coordinate system and the reference frame.

2.1 Radiation

2.1.1 Specific intensity and its moments

Specific intensity. The monochromatic specific intensity (surface brightness) I_λ is the proportionality coefficient in

$$dE \equiv I_\lambda(\lambda, \mathbf{r}, \mathbf{s}, t) \cos\theta \, dA \, d\Omega \, dt \, d\lambda, \tag{2.1}$$

where dE is the amount of energy transported in direction $\mathbf{s}$ at time interval dt per wavelength interval (λ, $d\lambda$) passing through an area dA at position $\mathbf{r}$ into a solid angle $d\Omega$. θ denotes the angle between the normal to dA and the direction $\mathbf{s}$.

Mean intensity. The mean intensity J_λ is the average of the specific intensity over all solid angles

$$J_\lambda(\mathbf{r}, t) = \frac{1}{4\pi} \int I_\lambda \, d\Omega = \frac{1}{4\pi} \int_0^{2\pi} d\phi \int_0^{\pi} I_\lambda \sin\theta \, d\theta.$$

Writing $d\Omega = \sin\theta \, d\theta \, d\phi = -d\mu \, d\phi$ with $\mu \equiv \cos\theta$ we have

$$J_\lambda(\mathbf{r}, t) = \frac{1}{4\pi} \int_0^{2\pi} d\phi \int_{-1}^{+1} I_\lambda \, d\mu. \tag{2.2}$$

Flux. The flux is the net flow of energy per unit time interval per unit wavelength interval at wavelength λ through a unit area placed at location $\mathbf{r}$ in direction $\mathbf{s}$. In principal, flux is a vector

$$\mathbf{F}_\lambda(\mathbf{r},t) = \int I_\lambda(\mathbf{r},\mathbf{s},t)\,\mathbf{s}\,d\Omega \tag{2.3}$$

2.1.2 Radiation – matter interaction

Emission. The monochromatic emissivity j_λ is defined by

$$dE \equiv j_\lambda\,dV\,dt\,d\lambda\,d\Omega, \tag{2.4}$$

where dE is the energy locally added to the radiation in volume dV per wavelength interval $d\lambda$ during the time interval dt into a solid angle $d\Omega$. The intensity contribution from the local emission to the beam is

$$dI_\lambda(s) = j_\lambda(s)\,ds, \tag{2.5}$$

where s measures the geometrical path length along the beam.

Extinction. The monochromatic extinction coefficient specifies the energy fraction taken from the beam due to absorption and scattering. The definition is

$$dI_\lambda(s) = \chi_\lambda\,I_\lambda\,ds, \tag{2.6}$$

with

$$\chi_\lambda = k_\lambda + \sigma_\lambda, \tag{2.7}$$

where k_λ and σ_λ are the absorption and scattering coefficients, respectively.

The contributions to χ_λ come from both the continuum and spectral lines

$$\chi_\lambda = \chi^c_\lambda + \chi^l_\lambda$$

In the present work we consider a simple case of a single spectral line with a Lorentz profile, and continuum extinction which does not depend on λ across the line, i.e.

$$\begin{aligned} \chi^c_\lambda &= \chi^c, \\ \chi^l_\lambda &= \pi\,\chi^l_0\,\varphi_\lambda\,(\gamma/2), \end{aligned}$$

with χ^l_0 the extinction coefficient at the line center λ_0. The line profile function is given by

$$\varphi_\lambda = \frac{1}{\pi}\,\frac{(\gamma/2)}{(\gamma/2)^2 + (\lambda-\lambda_0)^2}, \tag{2.8}$$

with $\gamma/2$ the full width at half maximum of the line, FWHM(λ). Thus the total extinction coefficient can be written as

$$\chi_\lambda = \chi^c\,(1 + 0.5\,\pi\,\gamma\,\xi_0\,\varphi_\lambda) = \chi^c\,f_\lambda, \tag{2.9}$$

where $\xi_0 = \chi^l_0/\chi^c$ is the line strength.

Source function. The source function is the ratio of emissivity to extinction

$$S_\lambda = j_\lambda / \chi_\lambda. \tag{2.10}$$

We consider a medium with thermal emission and coherent isotropic scattering that implies a source function in the following form

$$S_\lambda = (1 - \varepsilon_\lambda) J_\lambda + \varepsilon_\lambda B_\lambda, \tag{2.11}$$

with ε_λ the de-excitation coefficient defined by

$$\varepsilon_\lambda = \frac{k_\lambda}{k_\lambda + \sigma_\lambda} \tag{2.12}$$

and the Planck function

$$B_\lambda = \frac{2hc^2}{\lambda^5} \frac{1}{e^{hc/kT\lambda} - 1} \tag{2.13}$$

2.2 Radiative Transfer Equation

2.2.1 Transport along a ray in a static medium

The basic transfer equation governing the variation of the specific intensity I_λ through an atmosphere which absorbs and emits radiation of wavelength λ is obtained by counting the gains and losses of a pencil of radiation

$$dI_\lambda(s) = I_\lambda(s + ds) - I_\lambda(s) = j_\lambda(s)\, ds - \chi_\lambda(s)\, I_\lambda(s)\, ds$$

or

$$\frac{dI_\lambda}{ds} = j_\lambda - \chi_\lambda\, I_\lambda$$

or

$$\frac{dI_\lambda}{ds} = \chi_\lambda (S_\lambda - I_\lambda). \tag{2.14}$$

Cylindrical coordinate system. In general, any problem requires a choice of coordinate system which reflects its main properties and facilitates the solution of equations describing the problem. For problems without symmetries the Cartesian coordinates are the most appropriate. The Cartesian coordinate system may also be very advantageous in systems with certain symmetries when the problem is solved with help of purely numerical means. This results in a PDE with constant coefficients which contains only spatial derivatives and therefore can be easily discretized. Since there are no directional derivatives, many problems related to the angular grid and boundary

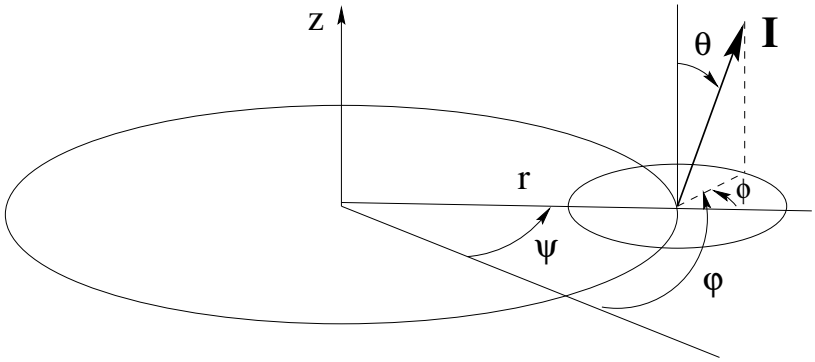

Fig. 2.1: Spatial and local directional coordinate systems.

conditions are avoided. However, the ignorance of the symmetrical properties leads to a computational redundancy. For instance, a radiative transfer problem in a disk which possesses axial symmetry requires the calculation of the specific intensity at grid $N_z \times N_x \times N_y$ if one uses the Cartesian coordinates, and only at grid $N_z \times N_r$ if the cylindrical coordinates are used. However, the direct solution of such a PDE with varying coefficients caused by the introduction of the cylindrical coordinates is a very difficult task for most available numerical and analytical methods. This is not the case for the perturbation theory we apply to solve this equation. Although an additional directional derivative appears in the equation, the method does not require any angular grid. Moreover, this approach provides us with an iterative solution with explicit dependence on directional angle.

According to Jones & Bayazitoglu (1992), the pathlength derivative in cylindrical coordinates is given by

$$\frac{d}{ds} = \cos\theta\frac{\partial}{\partial z} + \sin\theta\,\cos\phi\frac{\partial}{\partial r} - \sin\theta\,\sin\phi\frac{1}{r}\frac{\partial}{\partial\phi} + \sin\theta\,\sin\phi\frac{1}{r}\frac{\partial}{\partial\psi}, \quad (2.15)$$

where the variables (r, ψ, z) define the spatial location, and locally defined azimuthal ϕ and polar θ angles define the direction of the radiation relative to the spatial location (Fig.2.1). Due to the axial symmetry the last term in (2.15) disappears and the basic transfer equation (2.14) becomes

$$\cos\theta\frac{\partial I_\lambda}{\partial z} + \sin\theta\,\cos\phi\frac{\partial I_\lambda}{\partial r} - \sin\theta\,\sin\phi\frac{1}{r}\frac{\partial I_\lambda}{\partial\phi} = \chi_\lambda(S_\lambda - I_\lambda) \quad (2.16)$$

2.2.2 Radiative transfer equation in a rotating disk.

Choice of a reference frame. To study transport phenomena in a moving medium special attention has to be paid to the choice of the frame of reference. Appropriate choice of the frame may give considerable computational

advantage. To solve the radiative transfer equation in a moving medium it should be taken into account that in the observer's frame (an observer is fixed with respect to the center of the disk) the Doppler shift, aberration and advection make both opacity and emissivity angle dependent and hence anisotropic. However, this difficulty can be avoided by expressing the transfer equation in a frame comoving with the element under observation. The comoving frame is a relevant, 'natural' description for the radiative transfer equations since all thermodynamic quantities are only defined in this frame.

Transfer equation in the comoving frame. Let the matter of the disk move on a circular orbit at $z = const$ with Keplerian velocity

$$v_\varphi(r) = \sqrt{\frac{GM}{r}}, \tag{2.17}$$

with M the mass of the central object and G the gravitational constant. The velocity relative to an observer at rest is given by

$$\mathbf{v}(\mathbf{r}) = v_\varphi(r) \begin{pmatrix} -\sin\psi \\ \cos\psi \\ 0 \end{pmatrix}.$$

The presence of a velocity field in a medium gives rise to the Doppler shift of photons and other angular-dependent effects like advection and aberration, each of them of order $O(\mathbf{v}/c)$. The study of relative importance of these effects suggests that in the case of line profile calculation in slowly moving media the Doppler effect plays the major role (cf. Mihalas & Weibel Mihalas 1984, p. 492), and advection and aberration can be ignored.

Let all physical variables measured in the comoving frame be distinguished by subscripts such as $\theta_0, \phi_0, \lambda_0$ etc. The specific intensity in the comoving frame is

$$I_0 = I_0(z, r, \theta_0, \phi_0, \lambda_0).$$

If λ and λ_0 are wavelengths in the observer's and comoving frames then we have the classical formula for the Doppler shift obtained by retaining terms only up to $O(\mathbf{v}/c)$ and putting $\gamma \equiv 1/\sqrt{1-\beta^2} = 1$ for the Lorentz factor

$$\lambda_0 = \lambda(1 + \beta \cdot \mathbf{n}), \tag{2.18}$$

where $\beta = \mathbf{v}/c$ and the direction vector $\mathbf{n}$ has components

$$\mathbf{n} = (\sin\theta\cos\varphi,\ \sin\theta\sin\varphi,\ \cos\theta). \tag{2.19}$$

We assume that $\mathbf{n} = \mathbf{n}_0$, so that

$$\lambda_0 = \lambda\left(1 + \frac{1}{c}\sqrt{\frac{GM}{r}}\sin\theta_0\sin\phi_0\right). \tag{2.20}$$

To derive the transfer equation in the comoving frame we shall follow Wehrse et al. (2000). We consider any vector $\mathbf{r}(s)$ to depend on the variables $\mathbf{r}_0(s)$ and λ_0 rather than directly on s. Then the pathlength derivative (2.15) becomes

$$\frac{d}{ds} \Rightarrow \frac{\partial}{\partial s} + \frac{d\lambda_0}{ds}\frac{\partial}{\partial \lambda_0}, \tag{2.21}$$

with

$$\frac{d\lambda_0}{ds} = \lambda \frac{d(\beta \cdot \mathbf{n})}{ds} = \frac{\lambda_0}{1+\beta\cdot\mathbf{n_0}}\frac{d(\beta\cdot\mathbf{n_0})}{ds} \approx \lambda_0 \frac{d(\beta\cdot\mathbf{n_0})}{ds}.$$

Since

$$\begin{aligned}
\frac{\partial(\beta\cdot\mathbf{n_0})}{\partial z} &= 0, \\
\frac{\partial(\beta\cdot\mathbf{n_0})}{\partial \psi} &= 0, \\
\frac{\partial(\beta\cdot\mathbf{n_0})}{\partial \phi_0} &= \frac{1}{c}\sqrt{\frac{GM}{r}}\sin\theta_0\,\cos\phi_0, \\
\frac{\partial(\beta\cdot\mathbf{n_0})}{\partial r} &= -\frac{1}{2c}\sqrt{\frac{GM}{r^3}}\sin\theta_0\sin\phi_0,
\end{aligned}$$

we have

$$\begin{aligned}
\frac{d(\beta\cdot\mathbf{n_0})}{ds} &= -\frac{1}{2c}\sqrt{\frac{GM}{r^3}}\sin^2\theta_0\sin\phi_0\cos\phi_0 - \frac{1}{c}\sqrt{\frac{GM}{r^3}}\sin^2\theta_0\sin\phi_0\cos\phi_0 \\
&= -\frac{3}{4c}\sqrt{\frac{GM}{r^3}}\sin^2\theta_0\sin 2\phi_0 = w(r,\theta_0,\phi_0).
\end{aligned} \tag{2.22}$$

Thus the radiative transfer equation reads

$$\cos\theta\frac{\partial I}{\partial z} + \sin\theta\,\cos\phi\frac{\partial I}{\partial r} - \sin\theta\,\sin\phi\frac{1}{r}\frac{\partial I}{\partial \phi} + w\lambda\frac{\partial I}{\partial \lambda} = \chi(S-I). \tag{2.23}$$

where we have suppressed the subscripts 0 and λ to simplify notation. The last term in the left-hand side of (2.23), the Doppler term, describes the influence of a velocity gradient.

Chapter 3

Perturbation approach

In this chapter we shall discuss the applicability of the perturbation theory, describe the perturbation procedure as a whole, and give high order solutions in particular.

3.1 Applicability

The smallness of all gradients in the horizontal direction relative to the gradients in the vertical direction is the main criterion of the applicability of the perturbation approach. Once the assumption is made that most of the radiation flows in the vertical direction, it follows that the disk is geometrically thin, i.e. at any radial point r we have

$$r \gg z_0(r),$$

where $z_0(r)$ is the geometrical thickness of the disk at r. It is also obvious that the perturbation approach is not applicable when the matter of the disk moves with a very large velocity. We require therefore that

$$c \gg v_\varphi \gg v_r .$$

If above conditions are fulfilled the second to fourth terms in the left-hand side of equation (2.23) can evidently be treated as perturbations.

Thus the zero order solution is always the solution of a problem where the disk is regarded either as one static plane-parallel layer or as a system of *independent* rings, each of them radiating as a plane-parallel static medium. The latter case implies that all quantities do not depend on r across the width of a ring but their values can vary from one ring to another. It is obvious that the zero order solution does not depend on the angle ϕ; the radiation field in a plane-parallel medium is isotropic with respect to this azimuthal angle. Interactions of the rings with each other, radial gradients, velocity field etc.

are taken into account in the next orders of the perturbation approach. A consequence of these effects is an azimuthal variation of the radiation field.

3.2 Perturbation equations

Let us expand the specific intensity in power series depending on the small parameter $\delta \ll 1$

$$I(z,r,\phi,\mu) = I^{(0)}(z,r,\mu) + \delta\, I^{(1)}(z,r,\phi,\mu) + \delta^2\, I^{(2)}(z,r,\phi,\mu) + O(\delta^3) \quad (3.1)$$

Substitution of this series into equation (2.23) and collection of terms corresponding to the different powers of δ give us the zero, first and second order perturbation equations

$$\mu\frac{\partial I^{(0)}}{\partial\tau} = -f_\lambda I^{(0)} + \frac{1-\varepsilon}{2} f_\lambda \int_{-1}^{+1} I^{(0)}\, d\mu' + \varepsilon f_\lambda B, \quad (3.2)$$

$$\begin{aligned}\mu\frac{\partial I^{(1)}}{\partial\tau} &= -f_\lambda I^{(1)} + \frac{(1-\varepsilon)}{4\pi} f_\lambda \int_0^{2\pi} d\phi \int_{-1}^{+1} I^{(1)}\, d\mu' \\ &- \sqrt{1-\mu^2}\frac{1}{\chi_c}\cos\phi\frac{\partial I^{(0)}}{\partial r} - w\lambda\frac{1}{\chi_c}\frac{\partial I^{(0)}}{\partial\lambda},\end{aligned} \quad (3.3)$$

$$\begin{aligned}\mu\frac{\partial I^{(2)}}{\partial\tau} &= -f_\lambda I^{(2)} + \frac{(1-\varepsilon)}{4\pi} f_\lambda \int_0^{2\pi} d\phi \int_{-1}^{+1} I^{(2)}\, d\mu' \\ &- \sqrt{1-\mu^2}\frac{1}{\chi_c}\left(\cos\phi\frac{\partial I^{(1)}}{\partial r} - \frac{\sin\phi}{r}\frac{\partial I^{(1)}}{\partial\phi}\right) - w\lambda\frac{1}{\chi_c}\frac{\partial I^{(1)}}{\partial\lambda},\end{aligned} \quad (3.4)$$

where we have introduced, as a new variable in place of z, the optical depth

$$d\tau(z,r) = \chi_c(z,r)\, dz, \quad (3.5)$$

which is measured away from the symmetry plane and equals $-\Delta$ and Δ at the lower and upper boundary, respectively.

For the boundary conditions we require that no radiation is incident on the disk surface from outside, i.e.

$$I^+(-\Delta,r,\mu,\phi) = I^-(\Delta,r,\mu,\phi) = 0, \quad (3.6)$$

where $I^+ = I(\mu > 0)$ and $I^- = I(\mu < 0)$ are intensities in positive and negative directions with respect to μ.

3.3 Zero order

The zero order equation (3.2) will be considered in detail in the forthcoming chapters. There we shall derive a solution of this integro-differential equation

by means of two methods. The first method (Chapter 4) provides us with the solution under the simplifying conditions of the two-stream approximation. The method belongs to the family of Discrete Ordinate methods and was originally developed by Schuster and Schwarzschild (reprinted by Menzel 1966). Taking into account only two beams from the set of directed streams, we shall obtain a fast analytical solution whose accuracy strongly depends on the inclination of the chosen beams. The second method is a more sophisticated separable approximation method developed by Efimov et al. (1995, 1997). It is presented in Chapter 5 and enables us to obtain a very accurate solution without discretization of the spatial transport and integral operators in the transfer equation.

3.4 First order

In spite of the seeming complexity of the first and second order equations, their solutions can be obtained without much effort. We look for a solution of the first order equation (3.3) in the form

$$I^{(1)} = I_0^{(1)} + \cos\phi\, I_{\rm c}^{(1)} + \sin 2\phi\, I_{\rm s}^{(1)}. \tag{3.7}$$

Then we substitute it into (3.3) and equate terms corresponding to $\cos\phi$, $\sin 2\phi$ and remaining ones. A result is the system of equations which requires the already determined function $I^{(0)}$

$$\mu\frac{\partial I_0^{(1)}}{\partial\tau} = -f_\lambda I_0^{(1)} + \frac{1-\varepsilon}{2} f_\lambda \int_{-1}^{+1} I_0^{(1)}\, d\mu', \tag{3.8}$$

$$\mu\frac{\partial I_{\rm c}^{(1)}}{\partial\tau} = -f_\lambda I_{\rm c}^{(1)} - \sqrt{1-\mu^2}\,\frac{1}{\chi_c}\frac{\partial I^{(0)}}{\partial r}, \tag{3.9}$$

$$\mu\frac{\partial I_{\rm s}^{(1)}}{\partial\tau} = -f_\lambda I_{\rm s}^{(1)} + (1-\mu^2)\,\frac{3\lambda}{4c}\sqrt{\frac{GM}{r^3}}\,\frac{1}{\chi_c}\frac{\partial I^{(0)}}{\partial\lambda}. \tag{3.10}$$

Since equation (3.8) is the homogeneous equation and satisfies the zero boundary conditions, its solution equals zero. For equations (3.9) and (3.10) we give explicit solutions for I^+ only, since solutions for I^- follow analogously. Taking into account the boundary conditions (3.6), these solutions read

$$I_{\rm c}^{(1)}(\tau) = -\frac{\sqrt{1-\mu^2}}{\mu}\int_{-\Delta}^{\tau} e^{-\frac{f_\lambda}{\mu}(\tau-\tau')}\,\frac{1}{\chi_c}\frac{\partial I^{(0)}}{\partial r}\,d\tau', \tag{3.11}$$

$$I_{\rm s}^{(1)}(\tau) = \frac{1-\mu^2}{\mu}\,\frac{3\lambda}{4c}\sqrt{\frac{GM}{r^3}}\int_{-\Delta}^{\tau} e^{-\frac{f_\lambda}{\mu}(\tau-\tau')}\,\frac{1}{\chi_c}\frac{\partial I^{(0)}}{\partial\lambda}\,d\tau'. \tag{3.12}$$

3.5 Second order

We look for a solution of the second order equation (3.4) in the form

$$\begin{aligned} I^{(2)} &= I_0^{(2)} + \cos^2\phi\, I_{\rm c}^{(2)} + \sin^2\phi\, I_{\rm s}^{(2)} + \sin^2 2\phi\, I_{\rm 2s}^{(2)} \\ &+ \cos\phi\, \sin 2\phi\, I_{\rm c2s}^{(2)} + \sin\phi\, \cos 2\phi\, I_{\rm s2c}^{(2)}. \end{aligned} \tag{3.13}$$

In a similar way we have the system of equations

$$\mu\frac{\partial I_{\rm c}^{(2)}}{\partial\tau} = -f_\lambda I_{\rm c}^{(2)} - \sqrt{1-\mu^2}\frac{1}{\chi_c}\frac{\partial I_{\rm c}^{(1)}}{\partial r}, \tag{3.14}$$

$$\mu\frac{\partial I_{\rm s}^{(2)}}{\partial\tau} = -f_\lambda I_{\rm s}^{(2)} - \sqrt{1-\mu^2}\frac{1}{\chi_c}\frac{I_{\rm c}^{(1)}}{r}, \tag{3.15}$$

$$\mu\frac{\partial I_{\rm s2c}^{(2)}}{\partial\tau} = -f_\lambda I_{\rm s2c}^{(2)} + \sqrt{1-\mu^2}\frac{1}{\chi_c}\frac{2I_{\rm s}^{(1)}}{r}, \tag{3.16}$$

$$\mu\frac{\partial I_{\rm 2s}^{(2)}}{\partial\tau} = -f_\lambda I_{\rm 2s}^{(2)} + (1-\mu^2)\frac{3\lambda}{4c}\sqrt{\frac{GM}{r^3}}\frac{1}{\chi_c}\frac{\partial I_{\rm s}^{(1)}}{\partial\lambda}, \tag{3.17}$$

$$\mu\frac{\partial I_{\rm c2s}^{(2)}}{\partial\tau} = -f_\lambda I_{\rm c2s}^{(2)} + (1-\mu^2)\frac{3\lambda}{4c}\sqrt{\frac{GM}{r^3}}\frac{1}{\chi_c}\frac{\partial I_{\rm c}^{(1)}}{\partial\lambda} - \sqrt{1-\mu^2}\frac{1}{\chi_c}\frac{\partial I_{\rm s}^{(1)}}{\partial r}, \tag{3.18}$$

$$\mu\frac{\partial I_0^{(2)}}{\partial\tau} = -f_\lambda I_0^{(2)} + \frac{1-\varepsilon}{4}f_\lambda\int_{-1}^{+1}\left(2I_0^{(2)} + I_{\rm c}^{(2)} + I_{\rm s}^{(2)} + I_{\rm 2s}^{(2)}\right)d\mu'. \tag{3.19}$$

Solutions of equations (3.14) to (3.18) are straightforward for I^+

$$I_{\rm c}^{(2)}(\tau) = -\frac{\sqrt{1-\mu^2}}{\mu}\int_{-\Delta}^{\tau} e^{-\frac{f_\lambda}{\mu}(\tau-\tau')}\frac{1}{\chi_c}\frac{\partial I_{\rm c}^{(1)}}{\partial r}\,d\tau', \tag{3.20}$$

$$I_{\rm s}^{(2)}(\tau) = -\frac{\sqrt{1-\mu^2}}{\mu}\int_{-\Delta}^{\tau} e^{-\frac{f_\lambda}{\mu}(\tau-\tau')}\frac{1}{\chi_c}\frac{I_{\rm c}^{(1)}}{r}\,d\tau', \tag{3.21}$$

$$I_{\rm 2s}^{(2)}(\tau) = \frac{1-\mu^2}{\mu}\frac{3\lambda}{4c}\sqrt{\frac{GM}{r^3}}\int_{-\Delta}^{\tau} e^{-\frac{f_\lambda}{\mu}(\tau-\tau')}\frac{1}{\chi_c}\frac{\partial I_{\rm s}^{(1)}}{\partial\lambda}\,d\tau', \tag{3.22}$$

$$I_{\rm s2c}^{(2)}(\tau) = \frac{\sqrt{1-\mu^2}}{\mu}\int_{-\Delta}^{\tau} e^{-\frac{f_\lambda}{\mu}(\tau-\tau')}\frac{1}{\chi_c}\frac{2I_{\rm s}^{(1)}}{r}\,d\tau', \tag{3.23}$$

$$\begin{aligned} I_{\rm c2s}^{(2)}(\tau) &= \frac{1-\mu^2}{\mu}\frac{3\lambda}{4c}\sqrt{\frac{GM}{r^3}}\int_{-\Delta}^{\tau} e^{-\frac{f_\lambda}{\mu}(\tau-\tau')}\frac{1}{\chi_c}\frac{\partial I_{\rm c}^{(1)}}{\partial\lambda}\,d\tau' \\ &- \frac{\sqrt{1-\mu^2}}{\mu}\int_{-\Delta}^{\tau} e^{-\frac{f_\lambda}{\mu}(\tau-\tau')}\frac{1}{\chi_c}\frac{\partial I_{\rm s}^{(1)}}{\partial r}\,d\tau'. \end{aligned} \tag{3.24}$$

The integro-differential equation (3.19) can be solved by the same method as the zero order equation (3.2).

Chapter 4

Two-stream approximation

The present chapter is devoted to the solution of the plane-parallel radiative transfer equation in the two-stream approximation. This approximation makes the problem analytically solvable. In spite of the serious simplification, one can obtain a rather accurate solution by taking only two beams with an appropriate inclination. The analytical structure of the solution is simple and that allows us to investigate various dependences very easily.

First, we shall study the transfer equation with a constant de-excitation coefficient ε. Results available here serve as a starting point for the investigation of the properties of the plane-parallel radiative transfer equation before the application of more accurate methods. The main characteristics of the system such as the mean intensity and the flux are depth-weighted samplings of the Planck function with the weighting extending over a region around the depth of interest. The fully analytical solution enables us to investigate different aspects of the problem very quickly and to get a first insight into the problem. The developed technique will be partially applied in the method of separable approximation described in the next chapter.

Then we shall consider the transfer equation with ε varying in depth. We shall obtain analytical solutions for a large variety of internal distributions of ε (linear, quadratic etc.). We shall also propose methods for the derivation of solutions with a stochastic distribution of the de-excitation coefficient and ε with spikes, that enables us to treat the problem in media with different degrees of density inhomogeneity.

Having obtained exact solutions for the different behaviors of $\varepsilon(\tau)$, the solution of the inverse problem, i.e. the diagnostic of $\varepsilon(\tau)$ from observational data, becomes possible. In particular, the procedure for the derivation of the internal distribution of ε is facilitated in the case of isothermal media, since the characteristic behavior of the solution refers to the behavior of ε only. As an example, we shall find the corresponding parameters of the constant and linear distributions of $\varepsilon(\tau)$ precisely.

4.1 Constant ε

In the current section we obtain an analytical solution of the transfer equation with a depth-independent ε. Althought the assumption of the constant ε is unrealistic, it nevertheless represents a landmark test in radiative transfer theory.

4.1.1 Matrix form of the transfer equation and its solution

The specific intensity in the plane-parallel media with coherent isotropic scattering is governed by the following equation

$$\mu \frac{dI(\tau,\mu)}{d\tau} = -f_\lambda\, I(\tau,\mu) + \frac{1-\varepsilon}{2} f_\lambda \int_{-1}^{+1} I(\tau,\mu')\, d\mu' + \varepsilon f_\lambda\, B(\tau) \qquad (4.1)$$

Let us suppose that the radiation field can be characterized by a discrete number of directed streams ("discrete ordinates") to mimic the true variation of the intensity with angle. To simplify the problem we consider only two rays in opposite directions $\mu = \pm\mu_0$. Thus, instead of (2.2) and (2.3) the expressions for the mean intensity and the flux take the forms

$$J(\tau,\mu_0) = \frac{1}{2}\left(I^+(\tau) + I^-(\tau)\right), \qquad F(\tau,\mu_0) = \frac{1}{2}\left(I^+(\tau) - I^-(\tau)\right). \quad (4.2)$$

Equations for $I^+(\tau)$ and $I^-(\tau)$ become

$$\frac{d}{d\tau} I^+(\tau) = -k\, I^+(\tau) + \beta\, k \left(I^+(\tau) + I^-(\tau)\right) + \mathcal{B}(\tau), \qquad (4.3)$$

$$-\frac{d}{d\tau} I^-(\tau) = -k\, I^-(\tau) + \beta\, k \left(I^+(\tau) + I^-(\tau)\right) + \mathcal{B}(\tau), \qquad (4.4)$$

where

$$k = \frac{f_\lambda}{\mu_0}, \quad \beta = \frac{1-\epsilon}{2}, \quad \mathcal{B}(\tau) = \varepsilon\, k\, B(\tau).$$

and f_λ is defined in (2.9).

Let us introduce the two-component vector of the specific intensity

$$\mathbf{I}(\tau) = \begin{pmatrix} I^+(\tau) \\ I^-(\tau) \end{pmatrix}$$

Then equations (4.3) and (4.4) can be written in the form of a matrix equation

$$\frac{d}{d\tau}\mathbf{I}(\tau) = -\mathcal{M}\,\mathbf{I}(\tau) + \mathbf{B}(\tau), \qquad (4.5)$$

where

$$\mathcal{M} = k(\tau_3 - |e_-\rangle\beta\langle e_+|) = k\begin{pmatrix} 1-\beta & -\beta \\ \beta & -1+\beta \end{pmatrix}, \quad \mathbf{B}(\tau) = \mathcal{B}(\tau)|e_-\rangle,$$

with

$$|e_+\rangle = \begin{pmatrix} 1 \\ 1 \end{pmatrix}, \qquad |e_-\rangle = \begin{pmatrix} 1 \\ -1 \end{pmatrix}, \qquad \tau_3 = \begin{pmatrix} 1 & 0 \\ 0 & -1 \end{pmatrix},$$
$$\langle e_+| = (\ 1,\ 1\ ), \qquad \langle e_-| = (\ 1,\ -1\ )$$

The boundary conditions (3.6) can be represented in the following form

$$\mathbf{I}(\Delta) = \begin{pmatrix} I_{\text{out}} \\ 0 \end{pmatrix}, \qquad \mathbf{I}(-\Delta) = \begin{pmatrix} 0 \\ I_{\text{out}} \end{pmatrix}$$

or

$$\mathbf{I}(\Delta) = I_{\text{out}}\,\frac{1+\tau_3}{2}|e_+\rangle, \qquad \mathbf{I}(-\Delta) = I_{\text{out}}\,\frac{1-\tau_3}{2}|e_+\rangle, \tag{4.6}$$

where $I_{\text{out}}(\mu)$ is the outgoing intensity.

The formal solution of (4.5) can be written in two equivalent forms

$$\begin{aligned} \mathbf{I}(\tau) &= e^{-\mathcal{M}(\tau+\Delta)}\mathbf{I}(-\Delta) + \int_{-\Delta}^{\tau} e^{-\mathcal{M}(\tau-\tau')}\,\mathbf{B}(\tau')\,d\tau' \\ &= e^{-\mathcal{M}(\tau-\Delta)}\mathbf{I}(\Delta) - \int_{\tau}^{\Delta} e^{-\mathcal{M}(\tau-\tau')}\,\mathbf{B}(\tau')\,d\tau'. \end{aligned} \tag{4.7}$$

It follows from (4.7) that

$$\mathbf{I}(\Delta) = e^{-2\mathcal{M}\Delta}\mathbf{I}(-\Delta) + \int_{-\Delta}^{\Delta} e^{-\mathcal{M}(\Delta-\tau')}\,\mathbf{B}(\tau')\,d\tau'.$$

Multiplying both sides by $e^{\mathcal{M}\Delta}$ and using $\mathbf{B}(-\tau) = \mathbf{B}(\tau)$ we obtain

$$e^{\mathcal{M}\Delta}\mathbf{I}(\Delta) - e^{-\mathcal{M}\Delta}\mathbf{I}(-\Delta) = \int_{-\Delta}^{\Delta} \cosh(\mathcal{M}\tau')\mathbf{B}(\tau')\,d\tau'. \tag{4.8}$$

Substitution of (4.6) into (4.8) gives

$$\left[e^{\mathcal{M}\Delta}\frac{1+\tau_3}{2} - e^{-\mathcal{M}\Delta}\frac{1-\tau_3}{2}\right] I_{\text{out}}|e_+\rangle = \int_{-\Delta}^{\Delta} \cosh(\mathcal{M}\,\tau')\,\mathbf{B}(\tau')\,d\tau',$$

$$[\tau_3 + \tanh(\mathcal{M}\Delta)]\,I_{\text{out}}|e_+\rangle = \int_{-\Delta}^{\Delta} \frac{\cosh(\mathcal{M}\tau')}{\cosh(\mathcal{M}\Delta)}\mathbf{B}(\tau')\,d\tau'.$$

Finally, multiplying both sides of the last equation by $\langle e_-|$ we get an expression defining the intensity emerging from the disk surface

$$I_{\rm out} = \frac{2}{\langle e_-|\tau_3 + \tanh(\mathcal{M}\Delta)|e_+\rangle} \int\limits_0^\Delta \left\langle e_- \left| \frac{\cosh(\mathcal{M}\tau')}{\cosh(\mathcal{M}\Delta)} \right| e_- \right\rangle \mathcal{B}(\tau')\, d\tau'. \quad (4.9)$$

Using (4.7) and the following relation

$$\mathbf{I}(\Delta) + \mathbf{I}(-\Delta) = I_{\rm out}|e_+\rangle$$

we obtain

$$\begin{aligned} \mathbf{I}(\tau) &= \frac{e^{-\mathcal{M}\tau}}{2\cosh(\mathcal{M}\Delta)} I_{\rm out}|e_+\rangle \quad (4.10) \\ &+ \int\limits_{-\Delta}^{\Delta} \left\{ \Theta(\tau-\tau') \frac{e^{-\mathcal{M}(-\Delta+\tau-\tau')}}{2\cosh(\mathcal{M}\Delta)} - \Theta(\tau'-\tau) \frac{e^{-\mathcal{M}(\Delta+\tau-\tau')}}{2\cosh(\mathcal{M}\Delta)} \right\} \mathbf{B}(\tau')\, d\tau', \end{aligned}$$

where the unit step function $\Theta(x)$ is given by

$$\Theta(x) = \begin{cases} 0 \text{ for } x \le 0, \\ 1 \text{ for } x > 0. \end{cases}$$

The components of the vector $\mathbf{I}(\tau)$ can be obtained either directly from (4.10) or from the definitions of the mean intensity and the flux which in the present notations are

$$J(\tau) = \frac{1}{2}\langle e_+|\mathbf{I}(\tau)\rangle, \qquad F(\tau) = \frac{1}{2}\langle e_-|\mathbf{I}(\tau)\rangle. \quad (4.11)$$

For these purposes we use equalities

$$\begin{aligned} &e^{\mathcal{M}\tau} = \mathbf{1}\cosh(k\omega\tau) + \frac{\mathcal{M}}{k\omega}\sinh(k\omega\tau), \\ &\cosh(\mathcal{M}\tau) = \mathbf{1}\cosh(k\omega\tau), \\ &\sinh(\mathcal{M}\tau) = \frac{\mathcal{M}}{k\omega}\sinh(k\omega\tau), \\ &\tanh(\mathcal{M}\tau) = \frac{\mathcal{M}}{k\omega}\tanh(k\omega\tau), \\ &\frac{e^{-\mathcal{M}t}}{1+e^{\pm 2\mathcal{M}\Delta}} = \frac{1}{2\cosh(k\omega\Delta)} \left(\mathbf{1}\cosh(k\omega(\Delta\pm t) \mp \frac{\mathcal{M}}{k\omega}\sinh(k\omega(\Delta\pm t)\right), \end{aligned}$$

which are valid due to the following

$$\mathcal{M}^2 = \mathbf{1}\, k^2(1-2\beta) = \mathbf{1}\,(k\omega)^2 \quad \text{with} \quad \omega = \sqrt{1-2\beta} = \sqrt{\epsilon}.$$

Substituting them into (4.9) and (4.10) and using

$$\mathcal{M}|e_+\rangle = k(1-2\beta)|e_-\rangle = k\omega^2|e_-\rangle, \quad \mathcal{M}|e_-\rangle = k|e_+\rangle,$$
$$\langle e_-|\mathcal{M}|e_+\rangle = 2k(1-2\beta) = 2k\omega^2, \quad \langle e_+|\mathcal{M}|e_-\rangle = 2k$$

we get, in accordance with (4.11), expressions for the mean intensity and the flux

$$J(\tau) = \frac{\cosh(k\omega\tau)}{2\cosh(k\omega\Delta)} I_{\rm out} + \int_{-\Delta}^{\Delta} \frac{\sinh(k\omega(\Delta - |\tau-\tau'|))}{2\omega\cosh(k\omega\Delta)} \mathcal{B}(\tau')\, d\tau',$$

$$F(\tau) = -\frac{\omega}{2}\frac{\sinh(k\omega\tau)}{\cosh(k\omega\Delta)} I_{\rm out} + \int_{-\Delta}^{\Delta} \epsilon(\tau-\tau')\frac{\cosh(k\omega(\Delta - |\tau-\tau'|))}{2\cosh(k\omega\Delta)} \mathcal{B}(\tau')\, d\tau',$$

and the outgoing intensity

$$I_{\rm out} = \frac{2}{1+\omega\tanh(k\omega\Delta)} \int_0^{\Delta} \frac{\cosh(k\omega\tau')}{\cosh(k\omega\Delta)} \mathcal{B}(\tau')\, d\tau' \qquad (4.12)$$

with $\epsilon(x)$ the Heaviside function. Some transformations which follow after the substitution of $I_{\rm out}$ result in the final expressions for $J(\tau)$ and $F(\tau)$

$$\begin{aligned} J(\tau) &= \int_{-\Delta}^{\Delta} d\tau' \, \frac{\sqrt{\varepsilon}kB(\tau')}{1+\sqrt{\varepsilon}\tanh(k\sqrt{\varepsilon}\Delta)} \\ &\times \left(\sqrt{\varepsilon}\frac{\cosh(k\sqrt{\varepsilon}(\Delta - |\tau-\tau'|))}{2\cosh(k\sqrt{\varepsilon}\Delta)} + \frac{\sinh(k\sqrt{\varepsilon}(\Delta - |\tau-\tau'|))}{2\cosh(k\sqrt{\varepsilon}\Delta)}\right) \qquad (4.13) \\ F(\tau) &= \int_{-\Delta}^{\Delta} d\tau' \epsilon(\tau-\tau')\frac{\varepsilon kB(\tau')}{1+\sqrt{\varepsilon}\tanh(k\sqrt{\varepsilon}\Delta)} \\ &\times \left(\frac{\cosh(k\sqrt{\varepsilon}(\Delta - |\tau-\tau'|))}{2\cosh(k\sqrt{\varepsilon}\Delta)} + \sqrt{\varepsilon}\frac{\sinh(k\sqrt{\varepsilon}(\Delta - |\tau-\tau'|))}{2\cosh(k\sqrt{\varepsilon}\Delta)}\right) \qquad (4.14) \end{aligned}$$

Their application in media with different linearly depth-dependent B and constant ε is shown in Fig. 4.1. We set $f_\lambda = 1$. In order to get the best fit by eye to the precise solution obtained by the separable approximation method (Chapter 5) we choose beams with inclination $\mu_0 = 0.55$. Note that such a choice is very close to the Eddington approximation where $\mu_0 = 1/\sqrt{3} \approx 0.58$.

Fig. 4.1 demonstrates the influence of such quantities as the gradient of the Planck function and the de-excitation coefficient ε on the sign and the magnitude of the split between J and B. Such $J \neq B$ inequality is important in NLTE radiative transfer because it characterizes the non-local nature of

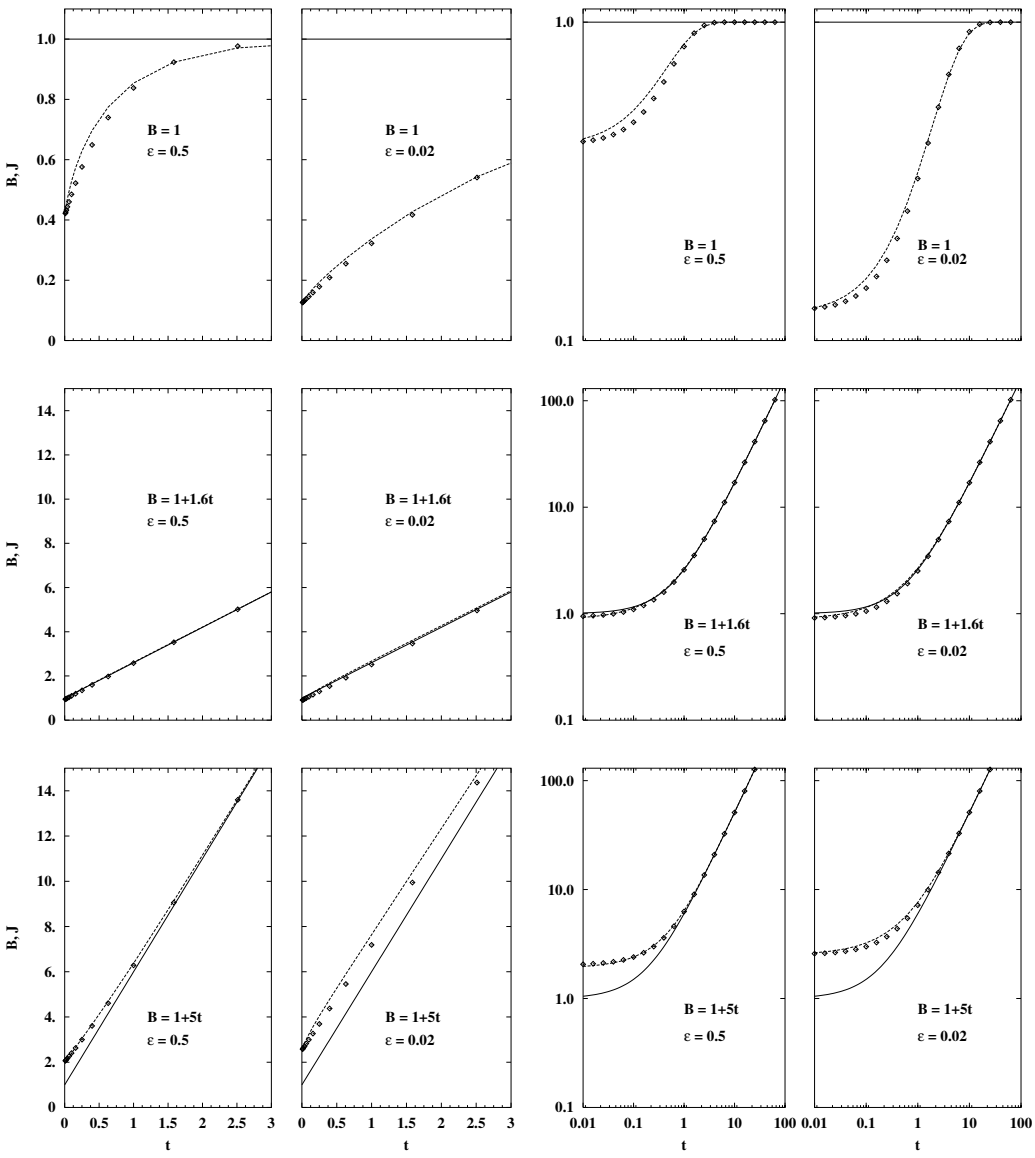

Fig. 4.1: Variation of B and J with depth in the upper part of a medium with depth-independent ε and linearly depth-dependent B for the different combinations of ε and dB/dt. $t = \Delta - \tau$, with $\Delta = 100$ the optical half-thickness of the medium. *Left-hand part:* numerical results plotted on linear scale. *Right-hand part:* the same results on logarithmic scale. *Solid:* the Planck function B. *Dashed:* the mean intensity J obtained by means of the separable approximation method (Chapter 5). *Diamonds:* corresponding two-stream approximation results from (4.13). *Top row:* isothermal atmosphere producing $J < B$. *Middle row:* "radiative-equilibrium gradient" $dB/dt = 1.6$ producing $J \approx B$. *Bottom row:* steep inward increase of the Planck function producing $J > B$.

the local radiation field. A flatter B gradient produces $J < B$, whereas a steeper one produces $J > B$. In the first case the production of photons in deeper layers is not sufficient to maintain $J \approx B$ higher up; in the second case, there are more photons arriving from the deeper layers than given by the local thermodynamic equilibrium prediction. The split extends to the thermalization depth $\Lambda \approx 1/\sqrt{\varepsilon}$.

4.1.2 Limit of large optical depth

For $k\sqrt{\varepsilon}\Delta \gg 1$ equations (4.13) and (4.14) look like

$$J(\tau) = \frac{k\sqrt{\varepsilon}}{2}\int_{-\Delta}^{\Delta}\left(e^{-k\sqrt{\varepsilon}|\tau-\tau'|} - \frac{1-\sqrt{\varepsilon}}{1+\sqrt{\varepsilon}}\,e^{-k\sqrt{\varepsilon}(2\Delta-|\tau-\tau'|)}\right)B(\tau')\,d\tau' \tag{4.15}$$

$$F(\tau) = \frac{k\varepsilon}{2}\int_{-\Delta}^{\Delta}\left(e^{-k\sqrt{\varepsilon}|\tau-\tau'|} + \frac{1-\sqrt{\varepsilon}}{1+\sqrt{\varepsilon}}\,e^{-k\sqrt{\varepsilon}(2\Delta-|\tau-\tau'|)}\right)\epsilon(\tau-\tau')B(\tau')\,d\tau' \tag{4.16}$$

If we are in a depth far from the boundary, the main contribution to the integrals comes from the first terms of the integrands, and the second terms can therefore be ignored. This can easily be proved by, e.g., the evaluation of the integrals with a constant Planck function. We consider then some reference point τ. We can write the Taylor expansion of the Planck function as

$$B(\tau') = \sum_{n=0}^{\infty}\frac{(\tau'-\tau)^n}{n!}\left[\frac{dB(\tau')}{d\tau'}\right]_{\tau}$$

Substitution in (4.15) and (4.16) gives us the values of $J(\tau)$ and $F(\tau)$ deep inside of the medium

$$J(\tau) \approx B(\tau) + \frac{1}{\varepsilon k}B''(\tau) + \cdots$$
$$F(\tau) \approx -\frac{1}{k}B'(\tau) - \frac{1}{\varepsilon k^3}B'''(\tau) + \cdots$$

where the restriction to the first terms only is referred to as the diffusion approximation.

4.1.3 Isothermal media

In the simple case of a medium with the constant Planck function $B(\tau) = B$ we have

$$J(\tau) \;=\; \left(1 - \frac{\cosh(k\sqrt{\varepsilon}\tau)}{\cosh(k\sqrt{\varepsilon}\Delta) + \sqrt{\varepsilon}\sinh(k\sqrt{\varepsilon}\Delta)}\right)B, \tag{4.17}$$

$$F(\tau) = \frac{\sqrt{\varepsilon}\sinh(k\sqrt{\varepsilon}\tau)}{\cosh(k\sqrt{\varepsilon}\Delta)+\sqrt{\varepsilon}\sinh(k\sqrt{\varepsilon}\Delta)}\,B, \tag{4.18}$$

$$I_{\rm out} = 2J(\Delta) = 2F(\Delta) = \frac{2\sqrt{\varepsilon}\tanh(k\sqrt{\varepsilon}\Delta)}{1+\sqrt{\varepsilon}\tanh(k\sqrt{\varepsilon}\Delta)}\,B. \tag{4.19}$$

Fig. 4.2 shows the angular distribution of the specific intensity emerging from a plane-parallel isothermal layer. The results from (4.19) are compared with those obtained by means of the separable approximation method. Since the scattering term in the transfer equation disappears for $\varepsilon = 1$, the results of both the methods are the same. In the case of optically thin slabs the agreement is quite good with the exception of grazing incidence ($\mu \to 0$). In optically thick media the agreement is much worse. The two-stream approximation method cannot even reproduce the correct behavior of the curves. Good accuracy can only be achieved in the narrow interval around $\mu \approx 0.5$. The choice of the beams with an inclination from this interval may also deliver the internal distribution of the radiation field quite accurately as shown in Fig. 4.1.

For optically thick media surface values of the mean intensity and the source function look like

$$\begin{aligned} J(\Delta) &= \frac{\sqrt{\varepsilon}}{1+\sqrt{\varepsilon}}\,B, \\ S(\Delta) &= (1-\varepsilon)J(\Delta)+\varepsilon\,B = \sqrt{\varepsilon}\,B. \end{aligned}$$

The last equation is the well-known $\sqrt{\varepsilon}$-law. The basic reason for this lack of emergent photons is that a photon on its way out in the direction to the observer suffers the chance being scattered back to internal regions of the medium where its random-walk steps are much shorter. It may well be confined there until it is eventually destroyed. Thus photons experience more difficulty in escaping. Compensation would occur if photons would enter from outside and be scattered back into the direction towards the observer, but such photons are absent because of the boundary conditions assumed.

There is asymmetry between creation and destruction of photons near the surface because photons may leave the medium without returning into the thermal pool. In LTE this photon leak is simply ignored by requiring thermal equilibrium between photon emission (= creation) and photon extinction (= destruction) all the way. Dropping the LTE condition means that the transport of photons is coupled self-consistently with the "transport" of lack of atomic excitation. The scattering part of the source function senses the anisotropy of the radiation field which increases towards the surface.

An appropriate thought experiment is to add a thin layer with $\varepsilon \ll 1$ on top of the medium. It creates a few additional photons and destroys a

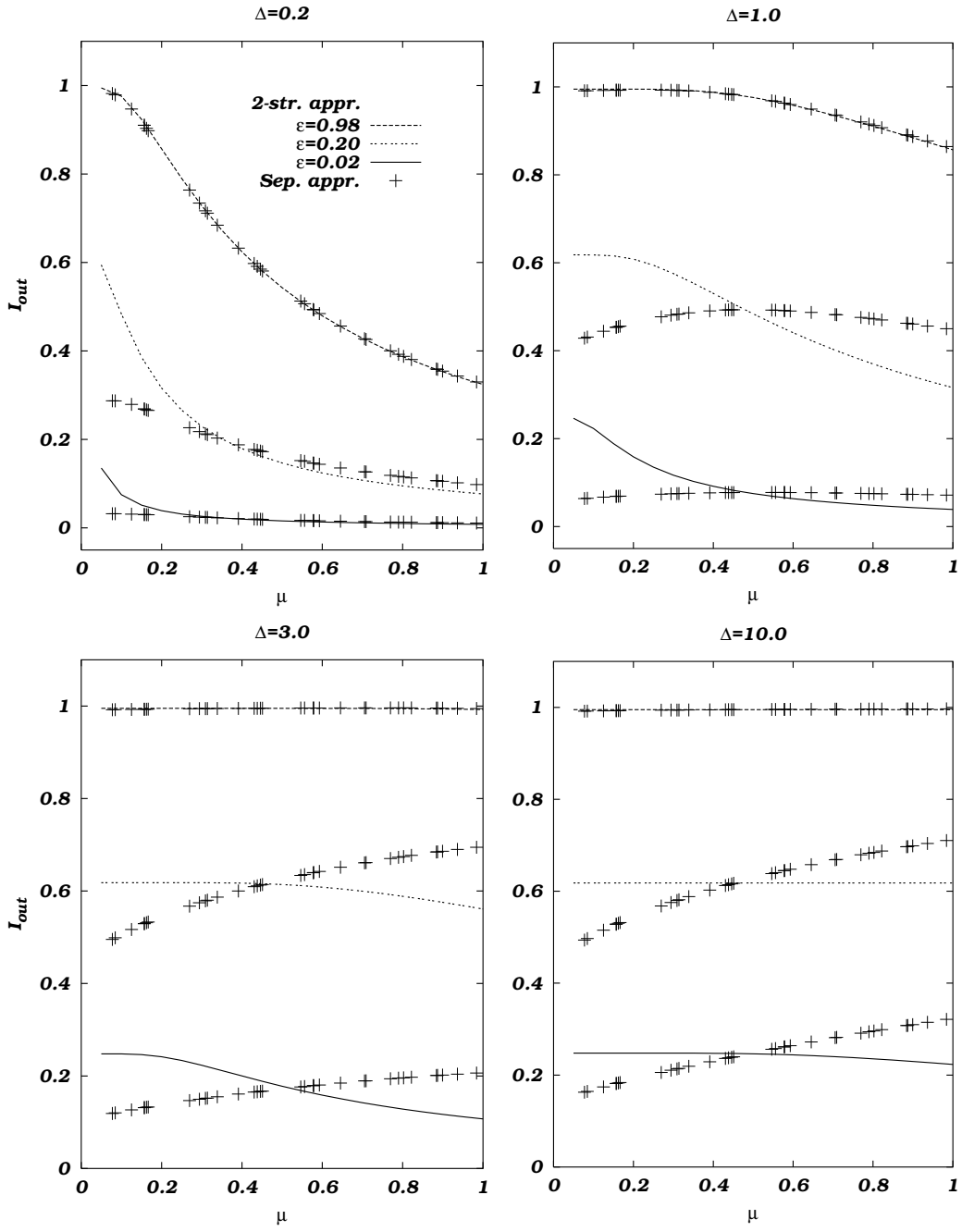

Fig. 4.2: Angular distribution of the emergent intensity in slabs of different optical thickness Δ with different values of ε and constant Planck function $B(\tau) = 1$. The comparison with the precise solutions is shown. Equation (4.19) was used for the derivation of the results in the two-stream approximation. The precise solutions were obtained by means of the separable approximation method as described in the next chapter.

few existing ones, but its main effect is that it scatters many more. The scattering prevents the flux; extra scattering reduces the emergent intensity. The same must hold for the next thin surface layer. A quantitative analysis of this experiment, producing the $\sqrt{\varepsilon}$-law exactly, is given by Hubeny (1987).

4.2 Depth-dependent $\varepsilon(\tau)$

So far we have discussed the problem of the radiative transfer in the slabs with constant de-excitation coefficient ε. However, there are many cases such as the transmission of light through the earth's atmosphere, the emission of radiation by nonisotropic high-temperature gas streams etc. where the properties of the medium may significantly vary with position. Even in the case of stellar atmospheres it is desirable to use varying ε, because the density decreases roughly exponentially outwards resulting in the increase of the collision probability inwards.

4.2.1 General solution

In order to obtain the desired solution we use a different method, namely, the Feautrier technique (cf. Mihalas 1978). Adding and subtracting equations (4.3) and (4.4) we have

$$\begin{aligned} \frac{dF(\tau)}{d\tau} &= k\,\varepsilon(\tau)(B(\tau) - J(\tau)), \\ \frac{dJ(\tau)}{d\tau} &= -kF(\tau). \end{aligned}$$

Elimination of $F(\tau)$ produces a second order differential equation

$$\left(-\frac{d^2}{d\tau^2} + k^2\varepsilon(\tau)\right) J(\tau) = k^2\varepsilon(\tau)B(\tau). \tag{4.20}$$

Further we shall use $k = 1$. An extension to the case of an arbitrary k can be done easily. Due to the symmetry it is sufficient to obtain the solution e.g. for the upper part of the slab: $0 \le \tau \le \Delta$. Then instead of the boundary condition at the lower surface we use the reflection condition at the symmetry plane: $I^+(0) = I^-(0)$. Since $F(\tau) = -J'(\tau)$, the boundary conditions can be written in terms of J as follows

$$J(\Delta) + J'(\Delta) = 0, \qquad J'(0) = 0. \tag{4.21}$$

Let $\{Y_1, (\tau), Y_2(\tau)\}$ be linearly independent solutions of the homogeneous equation (4.20) satisfying the normalization condition of the Wronskian

$$W = Y_1(\tau)Y_2'(\tau) - Y_2(\tau)Y_1'(\tau) = 1.$$

Then the formal solution of equation (4.20) becomes

$$\begin{aligned} J(\tau) &= C_1\, Y_1(\tau) + C_2\, Y_2(\tau) \\ &+ \int_0^\tau (Y_1(\tau)Y_2(\tau') - Y_1(\tau')Y_2(\tau))\ \mathcal{B}(\tau')\, d\tau', \qquad (4.22) \\ J'(\tau) &= C_1\, Y_1'(\tau) + C_2\, Y_2'(\tau) \\ &+ \int_0^\tau (Y_1'(\tau)Y_2(\tau') - Y_1(\tau')Y_2'(\tau))\ \mathcal{B}(\tau')\, d\tau'. \qquad (4.23) \end{aligned}$$

C_1 and C_2 are arbitrary constants whose values are defined by the boundary conditions (4.21)

$$\begin{aligned} C_1 &= -Y_2'(0) \int_0^\Delta \frac{\mathbf{Z}(\Delta)\sigma\mathbf{Y}(\tau')}{\mathbf{Z}(\Delta)\sigma\mathbf{Y}'(0)}\, \mathcal{B}(\tau')\, d\tau', \\ C_2 &= Y_1'(0) \int_0^\Delta \frac{\mathbf{Z}(\Delta)\sigma\mathbf{Y}(\tau')}{\mathbf{Z}(\Delta)\sigma\mathbf{Y}'(0)}\, \mathcal{B}(\tau')\, d\tau, \end{aligned}$$

where the following notations have been used

$$\mathbf{Y}(\tau) = \begin{pmatrix} Y_1(\tau) \\ Y_2(\tau) \end{pmatrix}, \quad \mathbf{Z}(\tau) = \begin{pmatrix} Y_1(\tau) + Y_1'(\tau) \\ Y_2(\tau) + Y_2'(\tau) \end{pmatrix}, \quad \sigma = \begin{pmatrix} 0 & 1 \\ -1 & 0 \end{pmatrix}.$$

Note that we do not distinguish column and row vectors, and a matrix product in the present notation means $\mathbf{xUy} = \sum_{i,j}^N x_i U_{ij} y_j$, where $\mathbf{x}$ and $\mathbf{y}$ are N-component vectors and $\mathbf{U}$ is an $N \times N$ matrix.

Substitution in (4.22) gives

$$\begin{aligned} J(\tau) &= -\frac{Y_1(\tau)Y_2'(0)}{\mathbf{Z}(\Delta)\sigma\mathbf{Y}'(0)} \int_0^\Delta \mathbf{Z}(\Delta)\sigma\mathbf{Y}(\tau')\, \mathcal{B}(\tau')\, d\tau' \\ &\quad + \frac{Y_2(\tau)Y_1'(0)}{\mathbf{Z}(\Delta)\sigma\mathbf{Y}'(0)} \int_0^\Delta \mathbf{Z}(\Delta)\sigma\mathbf{Y}(\tau')\, \mathcal{B}(\tau')\, d\tau' \\ &\quad + \int_0^\tau \mathbf{Y}(\tau)\sigma\mathbf{Y}(\tau')\, \mathcal{B}(\tau')\, d\tau', \end{aligned}$$

or

$$\begin{aligned} J(\tau) &= \frac{\mathbf{Y}'(0)\sigma\mathbf{Y}(\tau)}{\mathbf{Z}(\Delta)\sigma\mathbf{Y}'(0)} \int_0^\Delta \mathbf{Z}(\Delta)\sigma\mathbf{Y}(\tau')\, \mathcal{B}(\tau')\, d\tau' \\ &+ \int_0^\tau \mathbf{Y}(\tau)\sigma\mathbf{Y}(\tau')\, \mathcal{B}(\tau')\, d\tau'. \qquad (4.24) \end{aligned}$$

For arbitrary vectors $\mathbf{U}$, $\mathbf{V}$, $\mathbf{X}$, $\mathbf{Y}$ the following identity is valid

$$\begin{aligned} &(\mathbf{U}(u)\sigma\mathbf{V}(v))(\mathbf{X}(x)\sigma\mathbf{Y}(y)) = \qquad (4.25) \\ &(\mathbf{U}(u)\sigma\mathbf{Y}(y))(\mathbf{X}(x)\sigma\mathbf{V}(v)) - (\mathbf{U}(u)\sigma\mathbf{X}(x))(\mathbf{Y}(y)\sigma\mathbf{V}(v)). \end{aligned}$$

Table 4.1: The different kinds of $\varepsilon(\tau)$ and corresponding linearly independent solutions of the homogeneous equation (4.20). The divergence at $\tau = 0$ in the last three examples can be removed by an appropriate coordinate shift.

$\varepsilon(\tau)$	$Y_1(\tau)$	$Y_2(\tau)$
b^2	$\cosh(b\tau)$	$\frac{1}{b}\sinh(b\tau)$
$a\tau + b$	$\mathrm{Ai}\left(\frac{a\tau+b}{\lvert a\rvert^{2/3}}\right)$	$\pi\frac{\lvert a\rvert^{2/3}}{a}\mathrm{Bi}\left(\frac{a\tau+b}{\lvert a\rvert^{2/3}}\right)$
$a^2\tau^2 + b$	$a^{1/4}e^{-\frac{a\tau^2}{2}}F(\frac{a+b}{4a}, \frac{1}{2}; a\tau^2)$	$a^{-1/4}e^{-\frac{a\tau^2}{2}}\tau F(\frac{3a+b}{4a}, \frac{3}{2}; a\tau^2)$
$\frac{b^2m^2-\frac{1}{4}}{\tau^2} + \frac{b^2a^2\tau^{2b}}{\tau^2}$	$\sqrt{\tau}\,K_m(a\tau^b)$	$\frac{1}{b}\sqrt{\tau}\,I_m(a\tau^b)$
$\frac{1}{4} - \frac{b-2a}{2\tau} - \frac{b(2-b)}{4\tau^2}$	$\tau^{\frac{b}{2}}e^{-\frac{\tau}{2}}\,F(a, b; \tau)$	$\frac{1}{1-b}\tau^{\frac{1-b}{2}}e^{-\frac{\tau}{2}}\,F(a-b+1, 2-b; \tau)$
$\frac{b^2m^2-\frac{1}{4}}{\tau^2} - \frac{kab^2\tau^b}{\tau^2} + \frac{b^2a^2\tau^{2b}}{4\tau^2}$	$\tau^{\frac{1-b}{2}}M_{k,-m}(a\tau^b)$	$\frac{1}{2mab}\tau^{\frac{1-b}{2}}M_{k,m}(a\tau^b)$

$\mathrm{Ai}(\tau)$, $\mathrm{Bi}(\tau)$ – the Airy functions,
$I_m(\tau)$, $K_m(\tau)$ – the modified Bessel functions,
$F(a, b; \tau)$ – the Kummer confluent hypergeometric function,
$M_{k,m}(\tau)$ – the Whittaker function, $2m \neq \pm1, \pm2, \pm3 \ldots$

Breaking the interval of integration in the first integral in (4.24) and using (4.25) we get

$$\begin{aligned} J(\tau) &= \frac{\mathbf{Z}(\Delta)\sigma\mathbf{Y}(\tau)}{\mathbf{Z}(\Delta)\sigma\mathbf{Y}'(0)}\int_0^\tau \mathbf{Y}'(0)\sigma\mathbf{Y}(\tau')\,\mathcal{B}(\tau')\,d\tau' \\ &+ \frac{\mathbf{Y}'(0)\sigma\mathbf{Y}(\tau)}{\mathbf{Z}(\Delta)\sigma\mathbf{Y}'(0)}\int_\tau^\Delta \mathbf{Z}(\Delta)\sigma\mathbf{Y}(\tau')\,\mathcal{B}(\tau')\,d\tau'. \end{aligned} \tag{4.26}$$

Since $\mathbf{Z}(\Delta)\sigma\mathbf{Y}(\Delta) = -1$, the mean intensity at the boundary $\tau = \Delta$ becomes

$$J(\Delta) = \int_0^\Delta \frac{\mathbf{Y}(\tau')\sigma\mathbf{Y}'(0)}{\mathbf{Z}(\Delta)\sigma\mathbf{Y}'(0)}\,\mathcal{B}(\tau')\,d\tau'. \tag{4.27}$$

As one can see the exact solution of the radiative transfer equation for the given run of $\varepsilon(\tau)$ requires only the knowledge of the linearly independent solutions of the homogeneous equation (4.20).

4.2.2 Examples

Some examples of the continuous distributions of $\varepsilon(\tau)$ and corresponding solutions $Y_1(\tau)$ and $Y_2(\tau)$ (taken from Abramowitz & Stegun 1972; Kamke

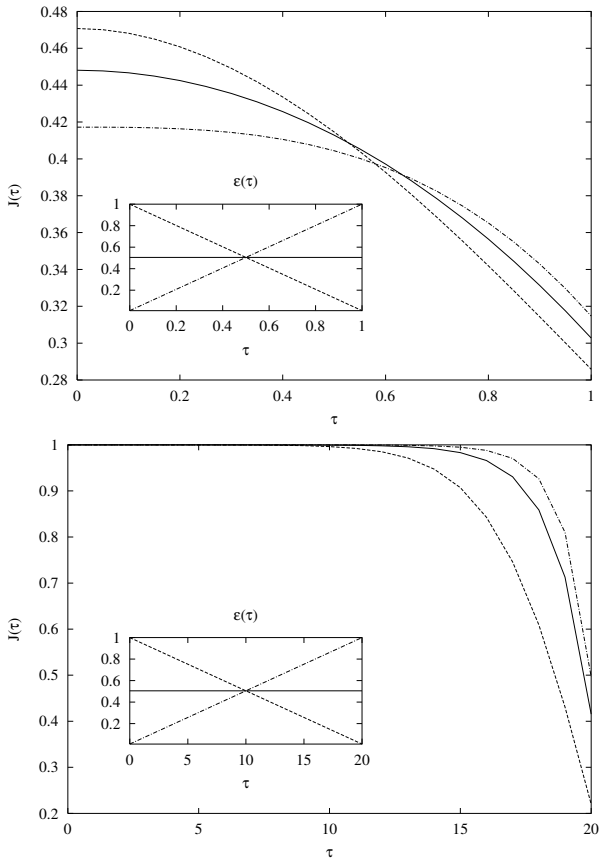

Fig. 4.3: Variations of the mean intensity in optically thin (*top*) and optically thick (*bottom*), isothermal, $B(\tau) = 1$, slabs with the different distributions of $\varepsilon(\tau)$ (see insert).

1965) have been collected in Table 4.1. The free parameters must be chosen in such a way to satisfy the condition of the location of $\varepsilon(\tau)$ in the interval between 0 and 1.

In spite of the small variation range of $\varepsilon(\tau)$, solutions obtained for different $\varepsilon(\tau)$ may have significant difference, especially in optically thick media. So, in Fig. 4.3 solutions of equation (4.20) with constant and linear $\varepsilon(\tau)$ are shown. In optically thin isothermal media (*top*) this difference does not exceed 10%. However, it becomes larger with the increasing of the total optical thickness and can reach 50% at some points in optically thick media (*bottom*).

Although the functions presented in Table 4.1 are suitable for the approximation of a large variety of internal distributions of $\varepsilon(\tau)$, they cannot be applied for the description of media with strong density condensations. Furthermore, the solution of the homogeneous equation (4.20) can hardly be found directly with $\varepsilon(\tau)$ approximated by a function with spikes. To avoid these difficulties we suggest the following procedure: if $\varepsilon(\tau)$ can be

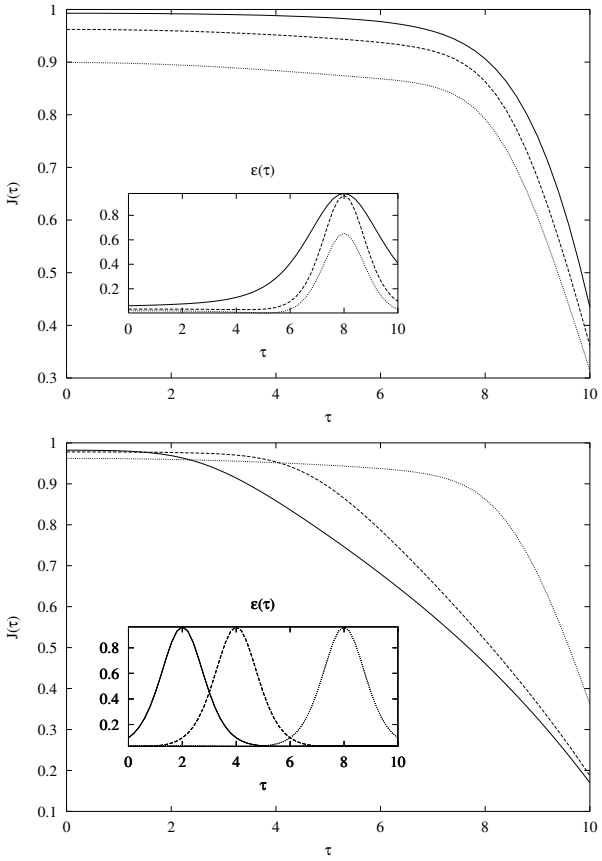

Fig. 4.4: The mean intensity as a function of the optical depth and $\varepsilon(\tau)$ whose internal distribution can be approximated by a resonance curve. The dependence on the shape and the position of the resonance is shown.

represented as

$$\varepsilon(\tau) \;=\; -A(\tau)\frac{d}{d\tau}\left(\frac{A'(\tau)}{A^2(\tau)}\right) + \varepsilon^{\mathrm{T}}(\tau)A^4(\tau), \tag{4.28}$$

then the corresponding solutions of the homogeneous equation (4.20) can be expressed through already known solutions in the following way

$$Y_i(\tau) \;=\; \frac{1}{A(\tau)}Y_i^{\mathrm{T}}(\phi(\tau)), \qquad (i=1,2) \tag{4.29}$$

where functions $\varepsilon^{\mathrm{T}}(\tau)$, $Y_1^{\mathrm{T}}(\tau)$ and $Y_2^{\mathrm{T}}(\tau)$ are taken from Table 4.1, $A(\tau)$ is known function and the differential equation $\phi'(\tau) = A^2(\tau)$ defines the function $\phi(\tau)$.

For example, the choice of

$$A(\tau) \;=\; 0.9 + \frac{0.3}{0.3 + (\tau - 8)^2}, \quad \varepsilon^{\mathrm{T}} = 0.047$$

leads to the dashed curves in the upper part of Fig. 4.4. The altering of the parameters results in the other curves.

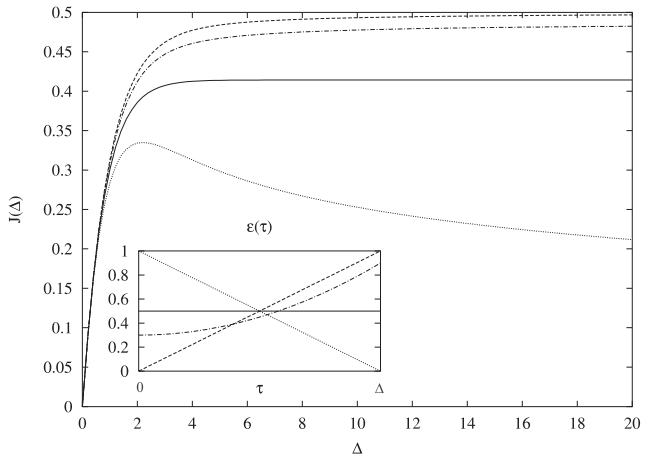

Fig. 4.5: The mean intensity at the boundary as a function of the optical thickness Δ. The curves correspond to the different runs of $\varepsilon(\tau)$: $\varepsilon(\tau) = \tau/\Delta$ (*dashed*), $\varepsilon(\tau) = 0.6(\tau/\Delta)^2 + 0.3$ (*dashed-dotted*), $\varepsilon(\tau) = -\tau/\Delta + 1$ (*dotted*) and $\varepsilon(\tau) = 0.5$ (*solid*).

4.2.3 Diagnostics of $\varepsilon(\tau)$

The prediction of the internal structure of a medium from observational data is one of the most important tasks in astrophysics. The only observable quantity of the problem is the emergent intensity which is a function of wavelength λ. The total optical thickness of a layer also depends on λ. The knowledge of these functions allows us to plot $J(\lambda(\Delta)) = J(\Delta)$ and therefore makes the prediction of $\varepsilon(\tau)$ possible. In the general case when the solution depends both on temperature and $\varepsilon(\tau)$, the diagnostic of $\varepsilon(\tau)$ is hardly possible. However, in the isothermal media the features of the solutions associate only with a definite behavior of $\varepsilon(\tau)$ (see Fig. 4.5) and therefore the derivation of the corresponding parameters of such the behavior seems not to be so hopeless. In order to confirm that, we consider a slab with $B = 1$, constant and linear $\varepsilon(\tau)$. In these cases the integration in (4.27) gives

$$J(\Delta) = \frac{\sqrt{\varepsilon}\tanh(\sqrt{\varepsilon}\Delta)}{1+\sqrt{\varepsilon}\tanh(\sqrt{\varepsilon}\Delta)} B \quad \text{for } \varepsilon(\tau) = \varepsilon, \tag{4.30}$$

$$J(\Delta) = \frac{\mathcal{A}}{1+\mathcal{A}} B \qquad \text{for } \varepsilon(\tau) = \left(\frac{a}{\Delta}\right)\tau + b, \tag{4.31}$$

where

$$\mathcal{A} = \frac{a\,\Delta^{1/3}}{|a|^{2/3}} \left\{ \mathrm{Ai}'\left(\frac{a+b}{(|a|/\Delta)^{2/3}}\right) \mathrm{Bi}'\left(\frac{b}{(|a|/\Delta)^{2/3}}\right) - \mathrm{Ai}'\left(\frac{b}{(|a|/\Delta)^{2/3}}\right) \mathrm{Bi}'\left(\frac{a+b}{(|a|/\Delta)^{2/3}}\right) \right\} \Big/$$

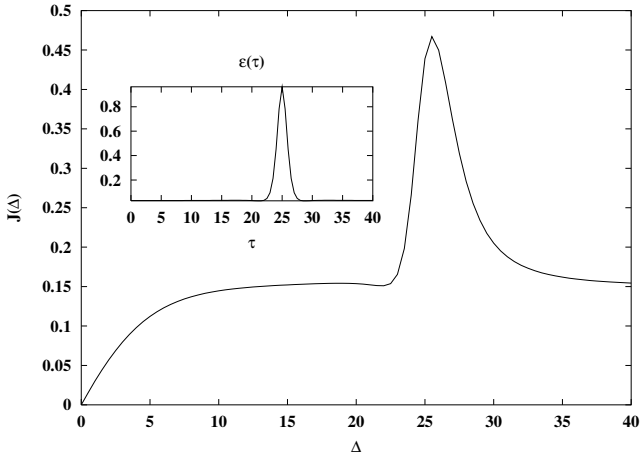

Fig. 4.6: The mean intensity at the boundary of a medium with a strong density condensation.

$$\left\{\mathrm{Ai}\left(\frac{a+b}{(|a|/\Delta)^{2/3}}\right)\mathrm{Bi}'\left(\frac{b}{(|a|/\Delta)^{2/3}}\right)\right.$$
$$\left. - \quad \mathrm{Ai}'\left(\frac{b}{(|a|/\Delta)^{2/3}}\right)\mathrm{Bi}\left(\frac{a+b}{(|a|/\Delta)^{2/3}}\right)\right\}.$$

These expressions can now be used for the fitting of observational data. In the case of a good fit the parameters of $\varepsilon(\tau)$ can be derived without much effort.

The derivation of the corresponding parameters can be done much easier if we take into account behaviors of these curves at the limit of large and small Δ. At the limit of small Δ these functions are proportional to Δ whereas at large Δ they saturate (Fig. 4.5) in accordance with the following

$$\begin{aligned} J(\Delta) &= \frac{\sqrt{\varepsilon}}{1+\sqrt{\varepsilon}}\,B \\ J(\Delta) &= \frac{\sqrt{a+b}}{1+\sqrt{a+b}}\,B \end{aligned} \qquad \text{for} \quad \Delta \gg 1, \tag{4.32}$$

$$\begin{aligned} J(\Delta) &= (\varepsilon\Delta - \varepsilon^2\Delta^2)\,B \\ J(\Delta) &= (\bar{\varepsilon}\Delta - \bar{\varepsilon}^2\Delta^2)\,B \end{aligned} \qquad \text{for} \quad \Delta \ll 1, \tag{4.33}$$

where $\bar{\varepsilon} = (a+2b)/2$.

We want to stress, however, that some features such as spikes occurring in intermediate points may be missed during the determination of the internal behavior of $\varepsilon(\tau)$ by means of this method (Fig. 4.6).

As mentioned above the presence of some peculiarities can point to the definite behavior of $\varepsilon(\tau)$ and, thus, simplify its diagnostic. For example, the maximum of the function $J(\Delta)$ may indicate a linearly decreasing $\varepsilon(\tau)$ (Fig. 4.5), although other distributions of the de-excitation coefficient may also result in such a feature.

4.2.4 Stochastic ε

The method described in subsection 4.2.2 enables us to consider media with a small number of inhomogeneities. However, in very inhomogeneous media whose properties can only be treated statistically it no longer works. Meanwhile, such media are ubiquitous as high resolution observations of the solar atmosphere, nova and supernova remnants, accretion disks etc. have shown and their investigations are very important. For the need to include strong spatial variations in reliable models see e.g. Gu et al. (1997). Unfortunately, in contrast to the Navier-Stokes equations, for the radiative transfer equation there is not yet a general homogenization scheme available that can deal with such situations, and exististing algorithms (see Gierens et al. 1986; Lindsey & Jefferies 1990; Nikoghossian et al. 1997) have a very limited range of application.

In order to solve the radiative transfer equation in a slab with many strong density inhomogeneities we divide it into N layers

$$[0,\Delta] = \bigcup_{j=1}^{N} [(j-1)\delta, j\delta], \qquad \delta = \frac{\Delta}{N}. \tag{4.34}$$

The Planck function and the de-excitation coefficient are assumed to be constant in each layer but their values differ from one layer to an other

$$\begin{array}{c} \varepsilon(\tau) = \varepsilon_j = \text{const} \\ B(\tau) = B_j = \text{const} \end{array} \qquad \text{for} \quad \tau \in [(j-1)\delta, j\delta].$$

In addition, ε_j is a function of a random number r_j whose values may be independent as well as obey correlations from layer to layer.

We do not use the formalism of Peraiah (1984) or that of Schmidt & Wehrse (1987) based on the interaction principle which relates the incident and emergent intensities in a layer. Instead of these, we propose another method which relates the mean intensity and the flux at one boundary of the layer with the same quantities at another boundary. By introducing the vector of the mean intensity

$$\mathbf{J}_j(\tau) \;=\; \begin{pmatrix} J_j(\tau) \\ J'_j(\tau) \end{pmatrix} \tag{4.35}$$

equations (4.22)-(4.23) may be written in a matrix form

$$\mathbf{J}(\tau) \;=\; \mathbf{R}(\tau)\mathbf{C} + \mathbf{R}(\tau)\,\sigma\int_0^\tau \mathbf{Y}(\tau')\,\mathcal{B}(\tau')\,d\tau', \tag{4.36}$$

with

$$\mathbf{R}(\tau) = \begin{pmatrix} Y_1(\tau) & Y_2(\tau) \\ Y_1'(\tau) & Y_2'(\tau) \end{pmatrix}, \qquad \mathbf{C} = \begin{pmatrix} C_1 \\ C_2 \end{pmatrix}.$$

Taking into account the boundary conditions

$$\mathbf{J}(0) = \begin{pmatrix} J(0) \\ 0 \end{pmatrix} = J(0)\mathbf{f}, \qquad \mathbf{J}(\Delta) = \begin{pmatrix} J(\Delta) \\ -J(\Delta) \end{pmatrix} = J(\Delta)\mathbf{g}, \tag{4.37}$$

with

$$\mathbf{f} = \begin{pmatrix} 1 \\ 0 \end{pmatrix} \quad \text{and} \quad \mathbf{g} = \begin{pmatrix} 1 \\ -1 \end{pmatrix}$$

we get the formal solution as

$$\mathbf{J}(\tau) \;=\; \mathbf{U}(\tau,0)\mathbf{J}(0) + \mathbf{R}(\tau)\,\sigma\int_0^\tau \mathbf{Y}(\tau')\mathcal{B}(\tau')\,d\tau', \tag{4.38}$$

where

$$\mathbf{U}(\tau_1,\tau_2) \;=\; \mathbf{R}(\tau_1)\mathbf{R}^{-1}(\tau_2), \qquad (\tau_1 \geq \tau_2).$$

In the case of constant $\varepsilon(\tau)$ and $B(\tau)$ we obtain the equation where corresponding values in the j-th cell can be represented in terms of those in cell $(j-1)$ by the following:

$$\mathbf{J}_j \;=\; \mathbf{U}_j\mathbf{J}_{j-1} - \mathbf{K}_j B_j, \tag{4.39}$$

with

$$\mathbf{U}_j = \begin{pmatrix} \cosh(\omega_j\delta) & \frac{1}{\omega_j}\sinh(\omega_j\delta) \\ \omega_j\sinh(\omega_j\delta) & \cosh(\omega_j\delta) \end{pmatrix}, \quad \mathbf{K}_j = \begin{pmatrix} \cosh(\omega_j\delta) - 1 \\ \omega_j\sinh(\omega_j\delta) \end{pmatrix}$$

B_j and ε_j denote the value of the Planck function and the de-excitation coefficient at the upper boundary of each layer.

A successive application of equation (4.39) – with the corresponding boundary conditions – allows us to study the evolution of the mean intensity in the medium (see Appendix A)

$$J_j = \frac{(\mathbf{eB}(N,j+1))(\mathbf{fU}(j,1)\mathbf{f})}{\mathbf{eU}(N,1)\mathbf{f}} + \frac{(\mathbf{eU}(N,j+1)\mathbf{h})(\mathbf{fW}(j,1))}{\mathbf{eU}(N,1)\mathbf{f}}, \tag{4.40}$$

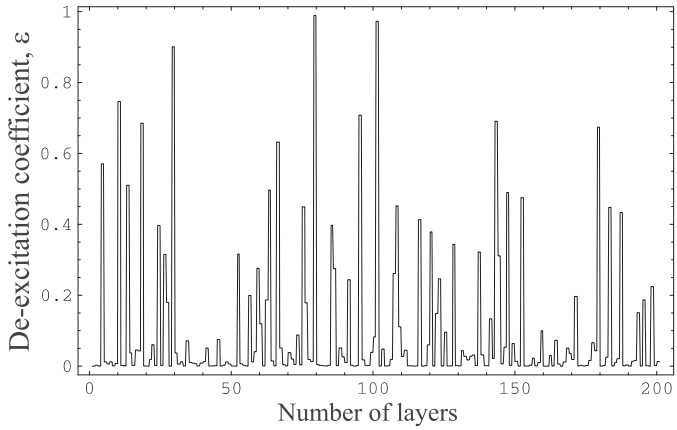

Fig. 4.7: An example of the stochastic distribution of ε

as well as to compute the value of J at the boundary

$$J_N = \frac{\mathbf{fW}(N,1)}{\mathbf{eU}(N,1)\mathbf{f}}, \tag{4.41}$$

where

$$\begin{aligned}
\mathbf{U}(j,i) &= \mathbf{U}_j\mathbf{U}_{j-1}...\mathbf{U}_i, \qquad (i \le j),\\
\mathbf{B}(j,i) &= \mathbf{U}(j,i+1)\mathbf{K}_i B_{i-1} + \mathbf{U}(j,i+2)\mathbf{K}_{i+1}B_i +\\
&+ \ ... + \mathbf{U}_j\mathbf{K}_{j-1}B_{j-2} + \mathbf{K}_j B_{j-1},\\
\mathbf{W}(j,1) &= \mathbf{W}_1\, B_0 + \mathbf{U}^\top(1,1)\mathbf{W}_2\, B_1 + ... + \mathbf{U}^\top(j-1,1)\mathbf{W}_j\, B_{j-1},
\end{aligned}$$

and

$$\mathbf{W}_j = \mathbf{U}_j^\top \sigma \mathbf{K}_j = \begin{pmatrix} \omega_j \sinh(\omega_j\delta) \\ \cosh(\omega_j\delta) - 1 \end{pmatrix}, \quad \mathbf{e} = \begin{pmatrix} 1 \\ 1 \end{pmatrix}, \quad \mathbf{h} = \begin{pmatrix} 0 \\ 1 \end{pmatrix}$$

The representations given for the matrix $\mathbf{U}_j$ and the vectors $\mathbf{K}_j$ and $\mathbf{W}_j$ are unfortunately not well suited for numerical calculations, since the hyperbolic functions involved lead to machine overflows for large δ. In order to overcome this problem we extract factors $X = \cosh(\omega_j\delta)$ from the expressions. It can be shown that the X-terms in the numerator and denominator of expressions (4.40)-(4.41) cancel, i.e we can use the following formulae

$$\begin{aligned}
\mathbf{U}_j &= \begin{pmatrix} 1 & \frac{1}{\omega_j}\tanh(\omega_j\delta) \\ \omega_j \tanh(\omega_j\delta) & 1 \end{pmatrix}, \qquad (4.42)\\
\mathbf{K}_j &= \begin{pmatrix} 1 - \mathrm{sech}(\omega_j\delta) \\ \omega_j \tanh(\omega_j\delta) \end{pmatrix}, \ \mathbf{W}_j = \begin{pmatrix} \omega_j \tanh(\omega_j\delta) \\ 1 - \mathrm{sech}(\omega_j\delta) \end{pmatrix}.
\end{aligned}$$

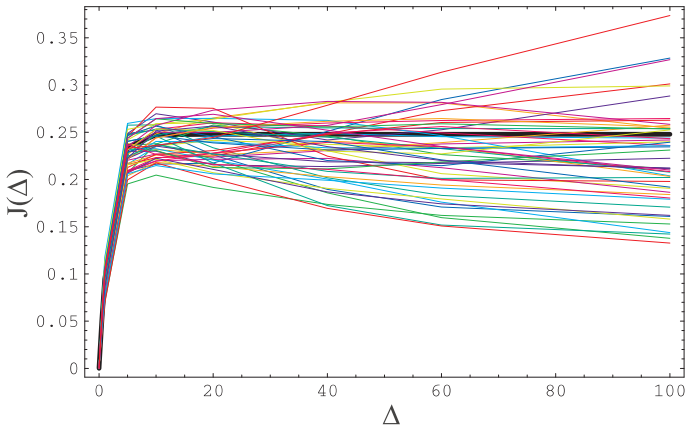

Fig. 4.8: Solutions obtained for 50 different realizations of ε. The bold curve was obtained for $\bar{\varepsilon}$.

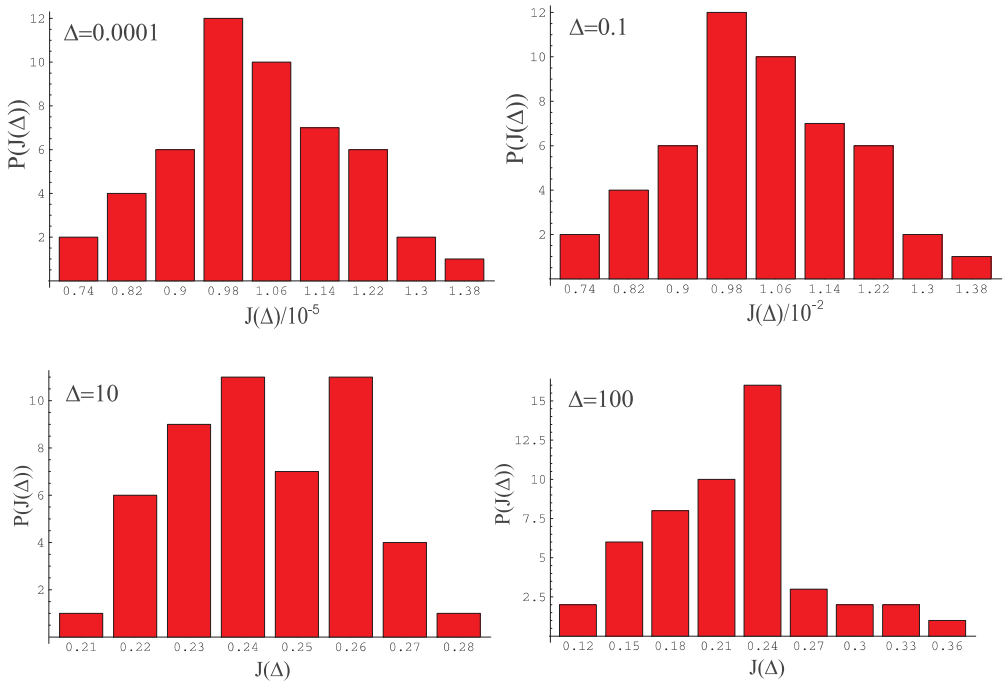

Fig. 4.9: Statistical distribution of $J(\Delta)$ from Fig.4.8. *Top left*: The mean value is $\langle J\rangle = 1.04\times10^{-5}$, the standard deviation $\sigma = 0.14\times10^{-5}$, the value of the bold curve (see Fig.4.8) at this point is $J_{\bar{\varepsilon}} = 1.09\times10^{-5}$. *Top right*: $\langle J\rangle = 1.03\times10^{-2}$, $\sigma = 0.14\times10^{-2}$, $J_{\bar{\varepsilon}} = 1.08\times10^{-5}$. *Bottom left*: $\langle J\rangle = 0.24$, $\sigma = 1.65\times10^{-2}$. $J_{\bar{\varepsilon}} = 0.247$. *Bottom right*: $\langle J\rangle = 0.22$, $\sigma = 0.052$, $J_{\bar{\varepsilon}} = 0.247$.

One is left with equations that involve *tanh* and *sech* functions only. If it is necessary, the sech(x) for large arguments can be approximated by $2e^{-x}$. In

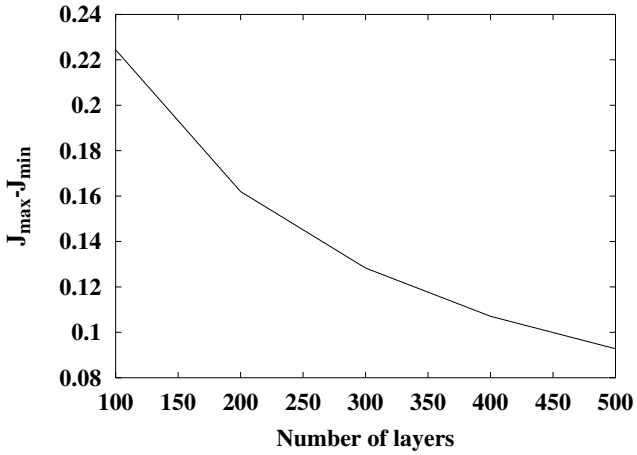

Fig. 4.10: The variation range vs the number of layers taken at $\Delta = 50$.

this way we have obtained convenient expressions that are well suited for all optical depths.

The solution obtained is written as a sequence of products of 2×2-matrices and two-component vectors that is easily implemented. It is no longer necessary to solve the system of $2(N-1)$ linear equations (N – number of layers) (Wehrse 1981) or to use the method of the forward elimination and back substitution (Peraiah 1984) for the determination of the internal distribution of J. The problems related to the finding of the corresponding inverse matrix and the keeping of many coefficients are thus avoided, so that the numerical calculations are sped up.

In our example we divide the slab into 200 layers. We require that values of ε_j lie in interval [0,1] and probability of appearance of small ε_j be higher. As an example of such ε_j we take the following

$$\varepsilon_j \quad = \quad 10^{-4r_j}, \tag{4.43}$$

where r_j are random numbers from the interval $[0, 1]$.

A realization of ε is shown in Fig. 4.7. In Fig. 4.8 one can see the set of solutions for 50 realizations of ε as well as the solution for $\bar{\varepsilon}$ in a medium with $B = 1$. Their statistical distributions at different Δ are shown in Fig. 4.9.

Since the number of layers does not change, the width of each layer becomes larger with increasing Δ and ε takes, thus, a block structure. This seems to be a reason of large scattering of curves at large Δ. In particular, the dependence of the variation range on the number of layers shown in Fig. 4.10 confirms this assumption.

Chapter 5

Separable approximation

A method for the solution of the plane-parallel radiative transfer equation without its spatial and angular discretizations is presented in this chapter. The basics of this largely analytical method were originally developed by Efimov et al. (1995, 1997). In these papers the attention was mostly paid to mathematical aspects of the problem and algorithmic aspects were hardly considered. Although some applications were discussed, they all referred to problems without photon sources in a medium. The problem with photon sources is treated here. In order to solve the inhomogeneous radiative transfer equation with a depth-dependent Planck function additional methods must be involved. Using the formalism of meromorphic functions as well as Krein's formula for the evaluation of inverse operators we are able to represent the solution in the form of an infinite sum. However, its extremely slow convergence makes this solution inefficient. The efficiency can be significantly improved by means of an approximation of the infinite sum by a finite one where the number of terms N defines the order of the approximation. There exist at least two methods which enable us to make this approximation in such a way that the solutions in the low approximation orders ($N \leq 5$) may be highly precise.

The analytical solution of the transfer equation by Chandrasekhar (1950) is not commonly used because Chandrasekhar functions H, X and Y are difficult to calculate. Furthermore, it provides the angular distribution of the emergent intensity only. Numerical methods are usually not well suited for media with steep gradients and/or large optical depths and scattering fraction. The present method does not suffer from these problems and accurate and rather fast solutions can be obtained for a wide range of parameters.

5.1 Basic equations

Again, as in the previous chapter, we start with the plane-parallel radiative transfer equation of the following form

$$\mu \frac{dI(\tau,\mu)}{d\tau} = -f_\lambda I(\tau,\mu) + \beta f_\lambda \int_{-1}^{+1} I(\tau,\mu')\, d\mu' + \varepsilon f_\lambda B(\tau). \qquad (5.1)$$

with $\beta = (1-\varepsilon)/2$, f_λ is defined in (2.9). The de-excitation coefficient ε is assumed to be constant.

We introduce $\mathcal{I}(\tau,\mu) = \sqrt{\mu}\, I(\tau,\mu)$ and regard $\mathcal{I}(\tau,\mu)$ as a vector in the infinite-dimensional space with respect to μ. Moreover, we distinguish intensities in the positive $\mathcal{I}^+(\tau,\mu)$ and negative direction $\mathcal{I}^-(\tau,\mu)$. The representation of the specific intensity as the two-component vector

$$\mathbf{I}(\tau,\mu) \;=\; \begin{pmatrix} \mathcal{I}^+(\tau,\mu) \\ \mathcal{I}^-(\tau,\mu) \end{pmatrix}$$

enables us to write equation (5.1) in compact matrix notation

$$\frac{d\mathbf{I}(\tau,\mu)}{d\tau} = -\mathbf{M}_{\mu\mu'}\, \mathbf{I}(\tau,\mu') + \mathbf{B}(\tau) \qquad (5.2)$$

where the integration over the index μ' is implied. The matrix $\mathbf{M}$ and the vector $\mathbf{B}$ are given by

$$\mathbf{M}_{\mu\mu'} = f_\lambda(\mathbf{D} - |\mathbf{v}\rangle\, \beta\, \langle\mathbf{u}|)_{\mu\mu'}, \quad \mathbf{B}(\tau) = \varepsilon f_\lambda B(\tau)|\mathbf{v}\rangle$$

with

$$\mathbf{D}_{\mu\mu'} = \frac{1}{\mu}\, \tau_3\, \delta(\mu-\mu'),\ |\mathbf{v}\rangle = \frac{1}{\sqrt{\mu}}|e_-\rangle,\ |\mathbf{u}\rangle = \frac{1}{\sqrt{\mu}}|e_+\rangle,$$

Subsequently we shall drop the index μ in the notation and use the following abbreviation

$$\begin{aligned} F(\mathbf{M})|\mathbf{v}\rangle &= \int_0^1 \frac{d\mu'}{\sqrt{\mu'}}\, F(\mathbf{M})_{\mu\mu'}|e_-\rangle, \\ \langle\mathbf{u}|F(\mathbf{M})|\mathbf{v}\rangle &= \iint_0^1 \frac{d\mu d\mu'}{\sqrt{\mu\mu'}}\, \langle e_+|F(\mathbf{M})_{\mu\mu'}|e_-\rangle. \end{aligned}$$

Carrying out the statements (4.6) to (4.9) with the new matrix $\mathbf{M}$ we obtain the equation for $\mathcal{I}_{\rm out}(\mu)$

$$\mathcal{I}_{\rm out} = \langle e_+| \frac{\varepsilon f_\lambda}{\tau_3 + \tanh(\mathbf{M}\Delta)} \int_0^\Delta \frac{\cosh(\mathbf{M}\tau')}{\cosh(\mathbf{M}\Delta)}\, B(\tau')|\mathbf{v}\rangle\, d\tau'. \qquad (5.3)$$

The internal distribution of the radiation field is given by the solution of equation (5.1). It is sufficient to solve this equation for I^+, since due to the symmetry I^- follows immediately

$$\mathcal{I}^+(-\tau) = \mathcal{I}^-(\tau). \tag{5.4}$$

Thus for the given mean intensity and the boundary conditions we have

$$I^+(\tau,\mu) = \frac{f_\lambda}{\mu}\int_{-\Delta}^{\tau} e^{-\frac{f_\lambda}{\mu}(\tau-\tau')}\left[(1-\varepsilon)J(\tau') + \varepsilon B(\tau')\right] d\tau' \tag{5.5}$$

The mean intensity is given by

$$\begin{aligned} J(\tau) &= \frac{1}{2}\int_0^1 \left(I^+(\tau,\mu') + I^-(\tau,\mu')\right) d\mu' \\ &= \frac{1}{2}\int_0^1 \frac{1}{\sqrt{\mu'}}\left(\mathcal{I}^+(\tau,\mu') + \mathcal{I}^-(\tau,\mu')\right) d\mu' \\ &= \frac{1}{4}\langle \mathbf{u}|\left(\mathcal{I}^+(\tau) + \mathcal{I}^-(\tau)\right)|e_+\rangle. \end{aligned}$$

Using the definition of $\mathbf{I}(\tau)$ and equation (5.4) we obtain

$$\mathbf{I}(\tau) + \mathbf{I}(-\tau) = \left(\mathcal{I}^+(\tau) + \mathcal{I}^-(\tau)\right)|e_+\rangle.$$

So that the mean intensity becomes

$$J(\tau) = \frac{1}{4}\langle \mathbf{u}|\mathbf{I}(\tau) + \mathbf{I}(-\tau)\rangle. \tag{5.6}$$

The substitution of (4.10) and (5.3) into (5.6) leads to

$$J(\tau) = \frac{\varepsilon f_\lambda}{4}\int_{-\Delta}^{\Delta} \left(G_1(\tau,\tau') + G_2(\tau-\tau')\right) B(\tau')\, d\tau' \tag{5.7}$$

where

$$\begin{aligned} G_1(\tau,\tau') &= \left\langle \mathbf{u}\left|\frac{\cosh(\mathbf{M}\tau)}{\cosh(\mathbf{M}\Delta)}\frac{1}{\tau_3 + \tanh(\mathbf{M}\Delta)}\frac{\cosh(\mathbf{M}\tau')}{\cosh(\mathbf{M}\Delta)}\right|\mathbf{v}\right\rangle \\ G_2(\tau-\tau') &= \left\langle \mathbf{u}\left|\frac{\sinh(\mathbf{M}(\Delta - |\tau-\tau'|))}{\cosh(\mathbf{M}\Delta)}\right|\mathbf{v}\right\rangle \end{aligned}$$

5.2 Evaluation of the matrix elements

In order to evaluate (5.3) and (5.7) we apply the formalism of meromorphic functions and Krein's formula.

By definition, a meromorphic function is a function that is analytic, except for a set of poles ξ_m. For a meromorphic function $F(z)$ decreasing for $|z| \to \infty$ the following representation is valid

$$F(z) = \sum_m \frac{\mathcal{F}_m}{z - \xi_m} \tag{5.8}$$

where

$$\mathcal{F}_m = \lim_{z \to \xi_m} (z - \xi_m) F(z).$$

In our case we have the meromorphic functions

$$\frac{\cosh(\mathbf{M}a)}{\cosh(\mathbf{M}\Delta)}, \quad \frac{\sinh(\mathbf{M}a)}{\cosh(\mathbf{M}\Delta)}, \quad |a| \le \Delta$$

which in accordance with (5.8) can be represented by

$$F(\mathbf{M}) \;=\; \sum_m \frac{\mathcal{F}_m}{\mathbf{M} - \xi_m} = \sum_{m=-\infty}^{\infty} \frac{F_m}{\mathbf{D} + iy_m - |\mathbf{v}\rangle\, \beta\, \langle \mathbf{u}|} \tag{5.9}$$

where the constants $F_m = \mathcal{F}/f_\lambda$ depend on the particular form of the function $F(\mathbf{M})$, and the simple poles are

$$\xi_m = -iy_m = -\frac{i\pi}{\Delta f_\lambda} \left(\frac{1}{2} + m \right).$$

In order to calculate an inverse operator as that in (5.9) we use Krein's formula which states that for an operator S acting in an appropriate space $\mathcal{L}$ and being of the following form

$$S = H - \sum_{i,j}^{N} |V_i\rangle c_{ij} \langle W_j| = H - |V\rangle\, c\, \langle W|$$

the inverse operator S^{-1} can be represented by

$$S^{-1} \;=\; \frac{1}{H} + \frac{1}{H} |V\rangle U \langle W| \frac{1}{H} \tag{5.10}$$

where

$$U = (1 - cT)^{-1} c, \qquad T_{ij} = \left\langle W_i \left| \frac{1}{H} \right| V_j \right\rangle.$$

H is an operator, $|V_i\rangle$ and $|W_i\rangle$ are vectors of the space $\mathcal{L}$, c_{ij} is a number matrix.

The application of Krein's formula leads to

$$F(\mathbf{M}) = F(f_\lambda \mathbf{D}) + \sum_m \frac{1}{\mathbf{D}+iy_m}\left|\mathbf{v}\right\rangle \frac{\beta F_m}{C(iy_m)}\left\langle \mathbf{u}\right| \frac{1}{\mathbf{D}+iy_m} \quad (5.11)$$

where

$$\begin{aligned} C(iy_m) &= C_m = 1 - \left\langle \mathbf{u}\left|\frac{\beta}{\mathbf{D}+iy_m}\right|\mathbf{v}\right\rangle \\ &= 1 - 2\beta\int_0^1 \frac{1}{1+\mu^2 y_m^2}\,d\mu = 1 - 2\beta\frac{\arctan(y_m)}{y_m} \end{aligned} \quad (5.12)$$

Using (5.11) and (5.12) we obtain

$$\begin{aligned} F(\mathbf{M})|\mathbf{v}\rangle &= \sum_m \frac{F_m}{C_m}\frac{1}{\mathbf{D}+iy_m}\left|\mathbf{v}\right\rangle, \\ \langle \mathbf{u}|F(\mathbf{M}) &= \sum_m \frac{F_m}{C_m}\left\langle \mathbf{u}\right|\frac{1}{\mathbf{D}+iy_m}, \\ \langle \mathbf{u}|F(\mathbf{M})|\mathbf{v}\rangle &= \frac{1}{\beta}\sum_m F_m\left(\frac{1}{C_m}-1\right). \end{aligned}$$

In order to evaluate these expressions we apply the following representation

$$\frac{1}{C_m} = 1 - \frac{2t_0}{C_1}\frac{1}{t_0^2+y_m^2} + \int_0^1 \frac{\rho(t)}{1+y_m^2 t^2}\,dt \quad (5.13)$$

where

$$\rho(t) = \frac{2\beta}{\left(1+\beta t\ln\left(\frac{1-t}{1+t}\right)\right)^2 + (\pi\beta t)^2},$$

t_0 is a positive root of the equation

$$C(t_0) = 1 + \frac{\beta}{t_0}\ln\left(\frac{1-t_0}{1+t_0}\right) = 0$$

and

$$C_1 = \left.\frac{dC(t)}{dt}\right|_{t=t_0} = \frac{1-t_0^2-2\beta}{t_0(1-t_0^2)}.$$

Since

$$\sum_m \frac{F_m}{\mu^2+y_m^2} = \sum_m \frac{F_m}{2\mu}\left(\frac{1}{\mu+iy_m}+\frac{1}{\mu-iy_m}\right) = \frac{1}{2\mu}(F(\mu f_\lambda) - F(-\mu f_\lambda))$$

we have for an odd $F(\mathbf{M})$

$$\langle \mathbf{u}|F(\mathbf{M})|\mathbf{v}\rangle \;=\; \frac{1}{\beta}\left(-\frac{2}{C_1}F(f_\lambda t_0)+\int_0^1 \frac{\rho(t)}{t}F\left(\frac{f_\lambda}{t}\right)\,dt\right).$$

In a similar way we obtain

$$\sum_m \frac{F_m}{\mu^2+y_m^2}\frac{1}{\mathbf{D}+iy_m} \;=\; \frac{F(f_\lambda \mathbf{D})}{\mu^2-\mathbf{D}^2}-\frac{1}{2\mu}\left(\frac{F(\mu f_\lambda)}{\mu-\mathbf{D}}+\frac{F(-\mu f_\lambda)}{\mu+\mathbf{D}}\right),$$

Finally, substituting instead of $F(\mathbf{M})$ its actual form we get

$$\begin{aligned}\left\langle \mathbf{u}\left|\frac{\sinh(\mathbf{M}(\Delta-|\tau-\tau'|))}{\cosh(\mathbf{M}\Delta)}\right|\mathbf{v}\right\rangle &= \Psi(|\tau-\tau'|),\\ \left.\frac{\cosh(\mathbf{M}\tau)}{\cosh(\mathbf{M}\Delta)}\right|\mathbf{v}\Big\rangle &= \Phi(\tau,\mu)|\,\mathbf{v}\rangle\,, \qquad (5.14)\\ \left\langle \mathbf{u}\left|\frac{\cosh(\mathbf{M}\tau)}{\cosh(\mathbf{M}\Delta)}\right.\right. &= \langle \mathbf{u}\,|\Phi(\tau,\mu)\end{aligned}$$

where

$$\Psi(\tau) \;=\; -\frac{2}{\beta C_1}\frac{\sinh(f_\lambda t_0(\Delta-\tau))}{\cosh(f_\lambda t_0\Delta)}+\frac{1}{\beta}\int_0^1 \frac{\rho(t)}{t}\frac{\sinh(f_\lambda(\Delta-\tau)/t)}{\cosh(f_\lambda\Delta/t)}dt$$

and

$$\begin{aligned}\Phi(\tau,\mu) &= \frac{\cosh(f_\lambda\tau/\mu)}{\cosh(f_\lambda\Delta/\mu)} \qquad (5.15)\\ &- \frac{2t_0}{C_1}\left(\frac{\cosh(f_\lambda\tau/\mu)}{\cosh(f_\lambda\Delta/\mu)}-\frac{\cosh(f_\lambda t_0\tau)}{\cosh(f_\lambda t_0\Delta)}\right)\frac{\mu^2}{t_0^2\mu^2-1}\\ &+ \int_0^1\left(\frac{\cosh(f_\lambda\tau/\mu)}{\cosh(f_\lambda\Delta/\mu)}-\frac{\cosh(f_\lambda\tau/t)}{\cosh(f_\lambda\Delta/t)}\right)\frac{\mu^2\rho(t)}{\mu^2-t^2}\,dt.\end{aligned}$$

The last operator which has to be represented in a form convenient for numerical work is $(1+\tau_3\tanh(\mathbf{M}\Delta))^{-1}$. The following representation is valid for the operator $\tanh(\mathbf{M}\Delta)$

$$\tanh(\mathbf{M}\Delta)=\frac{1}{\Delta f_\lambda}\sum_{m=-\infty}^{\infty}\frac{1}{\mathbf{D}+iy_m-|\mathbf{v}\rangle\,\beta\,\langle\mathbf{u}|} \qquad (5.16)$$

The application of Krein's formula leads to

$$\begin{aligned}\tau_3\tanh(\mathbf{M}\Delta) &= \frac{\tau_3}{\Delta f_\lambda}\sum_m\left(\frac{1}{\mathbf{D}+iy_m}+\left.\frac{\mathbf{D}-iy_m}{\mathbf{D}^2+y_m^2}\right|\mathbf{v}\right\rangle\frac{\beta}{C_m}\left\langle\mathbf{u}\left|\frac{\mathbf{D}-iy_m}{\mathbf{D}^2+y_m^2}\right.\right)\\ &= \tau_3\tanh(f_\lambda\mathbf{D}\Delta)+\frac{2\tau_3}{\Delta f_\lambda}\sum_{m=0}^{\infty}\left.\frac{\mathbf{D}}{\mathbf{D}^2+y_m^2}\right|\mathbf{v}\right\rangle\frac{\beta}{C_m}\left\langle\mathbf{u}\left|\frac{\mathbf{D}}{\mathbf{D}^2+y_m^2}\right.\right.\\ &\quad -\frac{2\tau_3}{\Delta f_\lambda}\sum_{m=0}^{\infty}\left.\frac{1}{\mathbf{D}^2+y_m^2}\right|\mathbf{v}\right\rangle\frac{\beta\,y_m^2}{C_m}\left\langle\mathbf{u}\left|\frac{1}{\mathbf{D}^2+y_m^2}\right.\right.\end{aligned}$$

Thus we have

$$\begin{aligned} 1+\tau_3\tanh(\mathbf{M}\Delta) &= w^{(0)}+w^{(1)}P_- - w^{(2)}P_+ \\ &= (w^{(0)}+w^{(1)})P_- + (w^{(0)}-w^{(2)})P_+ \end{aligned} \tag{5.17}$$

where $P_\pm = \frac{1}{2}|e_\pm\rangle\langle e_\pm|$ are the projection operators with the properties:

$$P_+ + P_- = 1, \quad P_\pm^2 = P_\pm, \quad P_\pm P_\mp = 0.$$

The operators $w^{(j)} = w^{(j)}(\mu,\mu')$, $(j=0,1,2)$ are given by

$$w^{(0)}(\mu,\mu') = \left[1+\tanh\left(\frac{f_\lambda\Delta}{\mu}\right)\right]\delta(\mu-\mu'), \tag{5.18}$$

$$w^{(1)}(\mu,\mu') = \frac{4\beta}{\Delta f_\lambda}\sum_{m=0}^{\infty}\frac{1}{C_m}\cdot\frac{\sqrt{\mu}}{1+y_m^2\mu^2}\cdot\frac{\sqrt{\mu'}}{1+y_m^2\mu'^2}, \tag{5.19}$$

$$w^{(2)}(\mu,\mu') = \frac{4\beta}{\Delta f_\lambda}\sum_{m=0}^{\infty}\frac{y_m^2}{C_m}\cdot\frac{\mu^{3/2}}{1+y_m^2\mu^2}\cdot\frac{\mu'^{3/2}}{1+y_m^2\mu'^2}. \tag{5.20}$$

The operators $w^{(1)}$ and $w^{(2)}$ are symmetric, positive definite and have finite traces (Efimov et al. 1995, 1997), i.e.

$$\mathrm{Tr}\, w^{(j)} = \int_0^1 w^{(j)}(\mu,\mu)\,d\mu < \infty, \quad (j=1,2).$$

The inversion of (5.17) is given by

$$\frac{1}{1+\tau_3\tanh(\mathbf{M}\Delta)} = \frac{1}{w^{(0)}+w^{(1)}}P_- + \frac{1}{w^{(0)}-w^{(2)}}P_+$$

so that

$$\begin{aligned} \frac{1}{\tau_3+\tanh(\mathbf{M}\Delta)} &= \left(\frac{1}{w^{(0)}-w^{(2)}}-\frac{1}{w^{(0)}}\right)P_+\tau_3 \\ &\quad -\left(\frac{1}{w^{(0)}}-\frac{1}{w^{(0)}+w^{(1)}}\right)P_-\tau_3 + \frac{1}{w^{(0)}}\tau_3 \end{aligned} \tag{5.21}$$

5.3 Separable representation of the solution

Krein's formula (5.10) can now be applied to the expressions in brackets in (5.21). $w^{(0)}$ corresponds to H and the terms

$$\frac{\sqrt{\mu}}{1+y_m^2\mu^2}\cdot\frac{\sqrt{\mu'}}{1+y_m^2\mu'^2}, \quad \text{and} \quad \frac{\mu^{3/2}}{1+y_m^2\mu^2}\cdot\frac{\mu'^{3/2}}{1+y_m^2\mu'^2}$$

which are present in the definitions (5.19) and (5.20) can be regarded as the vectors V_m and W_m. Unfortunately, the infinite sums converge very

slowly and one needs up to several thousands terms in order to achieve the required accuracy. Consequently, the dimension of the matrices involved in (5.10) becomes very large that makes the application of Krein's formula inefficient here. In order to accelerate computations we use the following approximations for $w^{(1)}$ and $w^{(2)}$.

The operators $w^{(1)}$ and $w^{(2)}$ are represented by

$$w^{(1)}(\mu,\mu') = \sqrt{\mu}\cdot\frac{E(\mu^2)-E(\mu'^2)}{\mu^2-\mu'^2}\cdot\sqrt{\mu'}, \tag{5.22}$$

$$w^{(2)}(\mu,\mu') = \mu^{3/2}\cdot\frac{\frac{E(\mu^2)}{\mu^2}-\frac{E(\mu'^2)}{\mu'^2}}{\mu'^2-\mu^2}\cdot\mu'^{3/2} \tag{5.23}$$

where

$$E(\mu^2) = \frac{4\beta}{\Delta f_\lambda}\sum_{m=0}^{\infty}\frac{1}{C_m}\cdot\frac{\mu^2}{1+y_m^2\mu^2}. \tag{5.24}$$

Let us approximate the function $E(t)$ by a finite sum

$$E(t)\approx E_N(t)=\sum_{n=1}^{N}\frac{a_n t}{1+A_n t}. \tag{5.25}$$

Then we get for (5.22) and (5.23)

$$w^{(1)}(\mu,\mu') \approx \sum_{nn'}^{N} V_n^{(1)}(\mu)\,a_n\delta_{nn'}\,V_{n'}^{(1)}(\mu') = |V^{(1)}\rangle J^{(1)}\langle V^{(1)}|, \tag{5.26}$$

$$w^{(2)}(\mu,\mu') \approx \sum_{nn'}^{N} V_n^{(2)}(\mu)\,a_n A_n\delta_{nn'}\,V_{n'}^{(2)}(\mu') = |V^{(2)}\rangle J^{(2)}\langle V^{(2)}| \tag{5.27}$$

where

$$V_n^{(1)}(\mu)=\frac{\sqrt{\mu}}{1+A_n\mu^2}, \qquad J_{nn'}^{(1)}=a_n\delta_{nn'},$$
$$V_n^{(2)}(\mu)=\frac{\mu^{3/2}}{1+A_n\mu^2}, \qquad J_{nn'}^{(2)}=a_n A_n\delta_{nn'}.$$

The number N in (5.25) defines the N-th separable approximation.

Taking into account representations (5.26) and (5.27) and using Krein's formula we now get

$$\frac{1}{w^{(0)}}-\frac{1}{w^{(0)}+w^{(1)}} = \frac{1}{w^{(0)}}\left|V^{(1)}\right\rangle S^{(1)}\left\langle V^{(1)}\right|\frac{1}{w^{(0)}},$$
$$\frac{1}{w^{(0)}-w^{(2)}}-\frac{1}{w^{(0)}} = \frac{1}{w^{(0)}}\left|V^{(2)}\right\rangle S^{(2)}\left\langle V^{(2)}\right|\frac{1}{w^{(0)}}$$

where

$$S^{(1)}_{nn'} = \left(\frac{1}{1+J^{(1)}U^{(1)}}\,J^{(1)}\right)_{nn'}, \quad S^{(2)}_{nn'} = \left(\frac{1}{1-J^{(2)}U^{(2)}}\,J^{(2)}\right)_{nn'}$$

and

$$\begin{aligned} U^{(1)}_{nn'} &= \frac{1}{2}\int_0^1 \frac{\mu\left(1+e^{-\frac{2\Delta f_\lambda}{\mu}}\right)}{(1+A_n\mu^2)(1+A_{n'}\mu^2)}\,d\mu, \\ U^{(2)}_{nn'} &= \frac{1}{2}\int_0^1 \frac{\mu^3\left(1+e^{-\frac{2\Delta f_\lambda}{\mu}}\right)}{(1+A_n\mu^2)(1+A_{n'}\mu^2)}\,d\mu. \end{aligned}$$

The substitution of the third term of (5.21) into (5.7) gives

$$\left\langle \mathbf{u}\left|\frac{\cosh(\mathbf{M}\tau')}{\cosh(\mathbf{M}\Delta)}\frac{\tau_3}{w^{(0)}}\frac{\cosh(\mathbf{M}\tau)}{\cosh(\mathbf{M}\Delta)}\right|\mathbf{v}\right\rangle = \int_0^1 \Phi(\tau,\mu)\Phi(\tau',\mu)(1+e^{-\frac{2\Delta f_\lambda}{\mu}})\frac{d\mu}{\mu}.$$

Because $P_-\tau_3|e_-\rangle = 0$, the contribution of the second term of (5.21) equals zero. The substitution of the first term gives

$$\begin{aligned} &\left\langle \mathbf{u}\left|\frac{\cosh(\mathbf{M}\tau)}{\cosh(\mathbf{M}\Delta)}\left(\frac{1}{w^{(0)}-w^{(2)}}-\frac{1}{w^{(0)}}\right)P_+\tau_3\frac{\cosh(\mathbf{M}\tau')}{\cosh(\mathbf{M}\Delta)}\right|\mathbf{v}\right\rangle \\ &\quad = \left\langle \mathbf{u}\left|\frac{\cosh(\mathbf{M}\tau)}{\cosh(\mathbf{M}\Delta)}\right|\mathbf{Y}^+_n\right\rangle S^{(2)}_{nn'}\left\langle \mathbf{Y}^-_{n'}\left|\frac{\cosh(\mathbf{M}\tau')}{\cosh(\mathbf{M}\Delta)}\right|\mathbf{v}\right\rangle \end{aligned}$$

where

$$|\mathbf{Y}^\pm_n\rangle = \frac{V^{(2)}_n}{w^{(0)}}|e_\pm\rangle$$

and

$$\begin{aligned} \left\langle \mathbf{u}\left|\frac{\cosh(\mathbf{M}\tau)}{\cosh(\mathbf{M}\Delta)}\right|\mathbf{Y}^+_n\right\rangle &= \left\langle \mathbf{Y}^-_n\left|\frac{\cosh(\mathbf{M}\tau)}{\cosh(\mathbf{M}\Delta)}\right|\mathbf{v}\right\rangle \\ &= \int_0^1 \Phi(\tau,\mu)\left(1+e^{-\frac{2\Delta f_\lambda}{\mu}}\right)\frac{\mu}{1+A_n\mu^2}d\mu = K_n(\tau). \end{aligned}$$

Taking into account the above expressions the mean intensity becomes

$$\begin{aligned} J(\tau) &= \frac{\varepsilon f_\lambda}{4}\left(\int_{-\Delta}^{\Delta}\Psi(|\tau-\tau'|)B(\tau')\,d\tau' + K_n(\tau)\,S^{(2)}_{nn'}\int_0^{\Delta}K_{n'}(\tau')B(\tau')\,d\tau'\right. \\ &+ \left.\int_0^1\frac{2}{\mu}\,\Phi(\tau,\mu)\left(1+e^{-\frac{2\Delta f_\lambda}{\mu}}\right)\int_0^{\Delta}\Phi(\tau',\mu)B(\tau')\,d\tau' d\mu\right) \end{aligned} \tag{5.28}$$

and the emerging intensity takes the form

$$I_{\rm out}(\mu) = \varepsilon f_\lambda \left(1 + e^{-\frac{2\Delta f_\lambda}{\mu}}\right) \left(\frac{1}{\mu}\int_0^\Delta \Phi(\tau',\mu)B(\tau')\,d\tau' + \frac{\mu}{2(1+A_n\mu^2)}\,S^{(2)}_{nn'}\int_0^\Delta K_{n'}(\tau')B(\tau')\,d\tau'\right) \quad (5.29)$$

where the Einstein's convention is implied.

5.4 Efficiency of the method

The practical efficiency of the method depends largely on how well the lower orders of the approximation represent the exact solution. In order to obtain an accurate solution in the low approximation orders a clever approximation of the function $E(t)$ is necessary. The representation of the original function (5.24) by the finite sum (5.25) with the minimal number of terms and without loss of accuracy is the crucial point of our investigation.

We propose two methods for the approximation (5.25). The first was originally developed by Stieltjes and Markov (Appendix B.1). Using the theory of the orthonormal polynomials, the coefficients a_n and A_n can be found very quickly. However, roundoff errors appearing in the calculation of the coefficients p_{kl} in (B.1.5) do not allow the method to be implemented, in particular, by means of FORTRAN codes. The method is well suited for programs like MATHEMATICA. The convergence of the final solution is moderate in optically thick media and high in optically thin ones.

The second method is the so called "Points method". It consist of the solution of the system of $2N$ algebraic equations as described in Appendix B.2. In contrast to the Stieltjes-Markov method it does not suffer from roundoff errors, and FORTRAN codes run very well. Some matrices become badly conditioned in the high approximation orders ($N > 6$). However these cases imply a very high accuracy of the final solution, which is usually not needed in applications, and are not considered. In optically thin media the solution obtained with such a_n and A_n shows approximately the same convergence as in the Stieltjes-Markov method. The convergence of the "Points method" is much better in optically thick slabs. The calculation of a_n and A_n takes much longer because one needs the values of the original $E(t)$ in the reference points $\{t_1, ..., t_{2N}\}$.

Further, all the calculations are carried out with the application of the "Points method" where the points are chosen as $t_i = i/2N$. In the present chapter we set $f_\lambda = 1$.

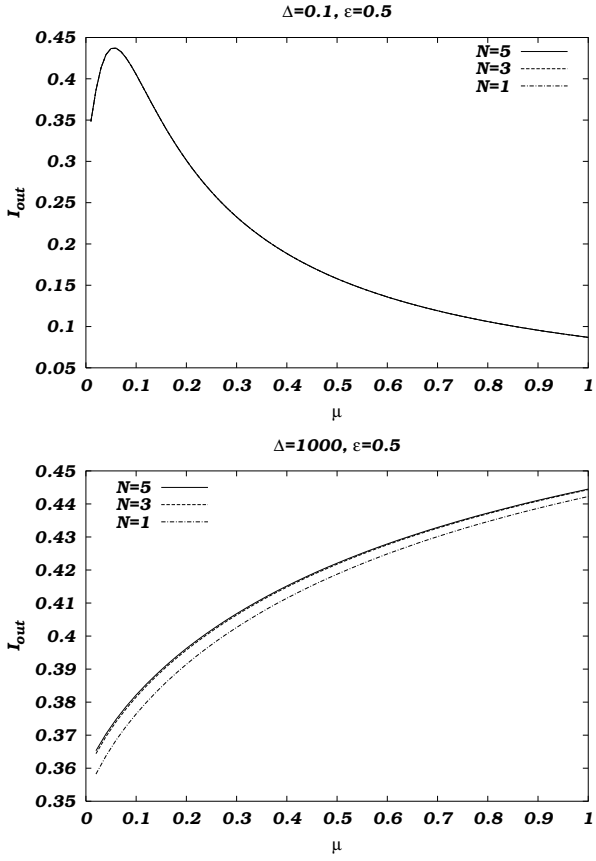

Fig. 5.1: Angular distribution of the outgoing intensity calculated in the different approximation orders by means of equation (5.5) with the Planck function $B(\tau) = 1 - 0.5\,(\tau/\Delta)^2$. In the upper panel the curves representing the results of the different approximation orders coincide.

Fig. 5.1 shows the angular distribution of the emergent intensity in slabs of different optical depth. The results were obtained through Eq. (5.5) with the mean intensity $J(\tau)$ calculated by means of (5.28). The dependence of the approximation order is shown. As one can see in optically thin media the precise results can be obtained already in the lowest separable approximation whereas in optically thick slabs a few additional approximation orders are necessary in order to match the exact solution.

However, the simplest and the fastest way for the calculation of the emergent intensity is the direct application of (5.29). As in the previous case a few approximation orders are sufficient to obtain the results with the reasonable accuracy. The exception is for the range of small μ (see Fig. 5.2). The difference between this solution and the exact one is caused by errors in the approximation of the function $E(\mu^2)$. So, for $\mu \to 0$ we have $E(\mu^2) \sim \mu$, whereas $E_N(\mu^2) \sim \mu^2$. Although the asymptotic behavior of $w^{(1)}(\mu, \mu')$ and $w_N^{(1)}(\mu, \mu')$ at small μ are the same, $w^{(2)}(\mu, \mu')$ and $w_N^{(2)}(\mu, \mu')$ behave in different ways: when $\mu, \mu' \to 0$ $w^{(2)}(\mu, \mu') \sim \sqrt{\mu}\sqrt{\mu'}$ while $w_N^{(2)}(\mu, \mu') \sim \mu^{3/2}\mu'^{3/2}$.

Better results in the region of small μ can be obtained by means of a

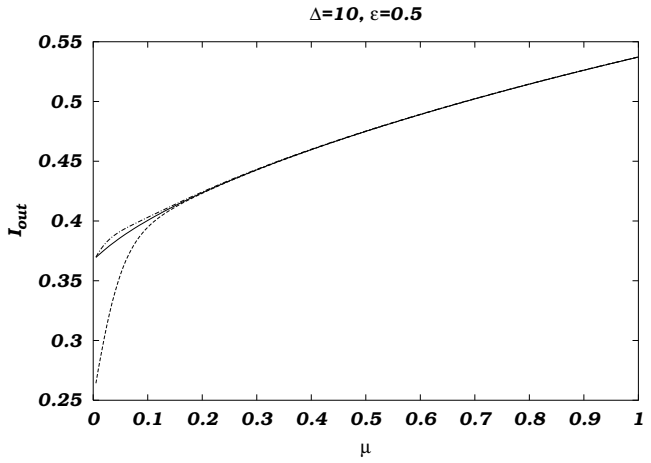

Fig. 5.2: Angular distribution of the outgoing intensity calculated in the 6-th approximation order with the Planck function $B(\tau) = 1 - 0.5\,(\tau/\Delta)^2$. The solid curve represents the precise results obtained by means of (5.5). Equation (5.29) was used to get the dashed curve. The results obtained with the improved approximation of the operator $w^{(2)}$ (5.30) are represented by the dashed-dotted curve.

further improvement of the approximation for the operator $w^{(2)}$:

$$\begin{aligned} w^{(2)}(\mu,\mu') &= \mu^{3/2}\cdot\frac{\frac{E(\mu^2)}{\mu^2}-\frac{E(\mu'^2)}{\mu'^2}}{\mu'^2-\mu^2}\cdot\mu'^{3/2} \\ &= \sqrt{\mu}\cdot\frac{\frac{\mu'}{\mu}E(\mu^2)-\frac{\mu}{\mu'}E(\mu'^2)}{\mu'^2-\mu^2}\cdot\sqrt{\mu'} \\ &= w^{(1)}(\mu,\mu')+w^{(3)}(\mu,\mu') \end{aligned} \tag{5.30}$$

where

$$w^{(3)}(\mu,\mu') = \sqrt{\mu}\cdot\frac{\frac{1}{\mu}E(\mu^2)-\frac{1}{\mu'}E(\mu'^2)}{\mu'-\mu}\cdot\sqrt{\mu'}.$$

Applying the "Points method" for the following approximation

$$\frac{1}{\mu}E(\mu^2) = \frac{4\beta}{\Delta f_\lambda}\sum_{m=0}^{\infty}\frac{1}{C_m}\cdot\frac{\mu}{1+y_m^2\mu^2}\approx\sum_{n=1}^{N}\frac{b_n}{1+B_n\mu} \tag{5.31}$$

we get

$$w^{(3)}(\mu,\mu') \approx \sum_{n=1}^{N}\frac{\sqrt{\mu}}{1+B_n\mu}\cdot b_nB_n\cdot\frac{\sqrt{\mu'}}{1+B_n\mu'}. \tag{5.32}$$

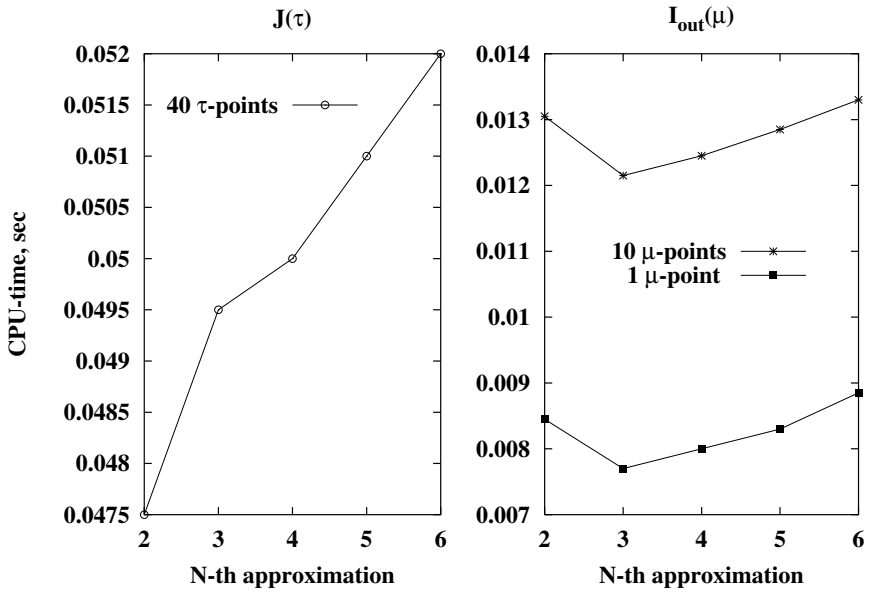

Fig. 5.3: CPU-time required for the calculation of the mean intensity and the intensity emerging from the surface of a slab with $\Delta = 100$ and $\varepsilon = 0.5$ in the different approximation orders.

Thus the final results calculated with the new representation of $w^{(2)}$ (5.30) show better agreement with the exact solution for all μ as shown in Fig. 5.2.

Fig. 5.3 shows the CPU-time required for the calculation of the internal distribution of the mean intensity (*left panel*; Eq. (5.28)) and the angular distribution of the outgoing intensity (*right panel*; Eq. (5.29)) in the different approximation orders. FORTRAN double-precision, optimized codes were used on a HP C240 computer. Note that time necessary for the calculations of the coefficients a_n, A_n and matrix $S^{(2)}_{nn'}$ is also included. Although these calculations are carried out only once for the given Δ and ε, the most time (about 8 ms in the 2nd order) is spent on this, which remains the place for further improvements.

The comparisons of our results with those obtained by means of the Finite Element (see Richling et al. 2001, and references therein) and the Finite Difference (Stenholm et al. 1991) methods are shown in Fig. 5.4. In general, these three codes give the same results. Excellent agreement is obtained between the present and the FE methods. The FD code is not able to reproduce the results of the other methods for the high optical depth and large scattering.

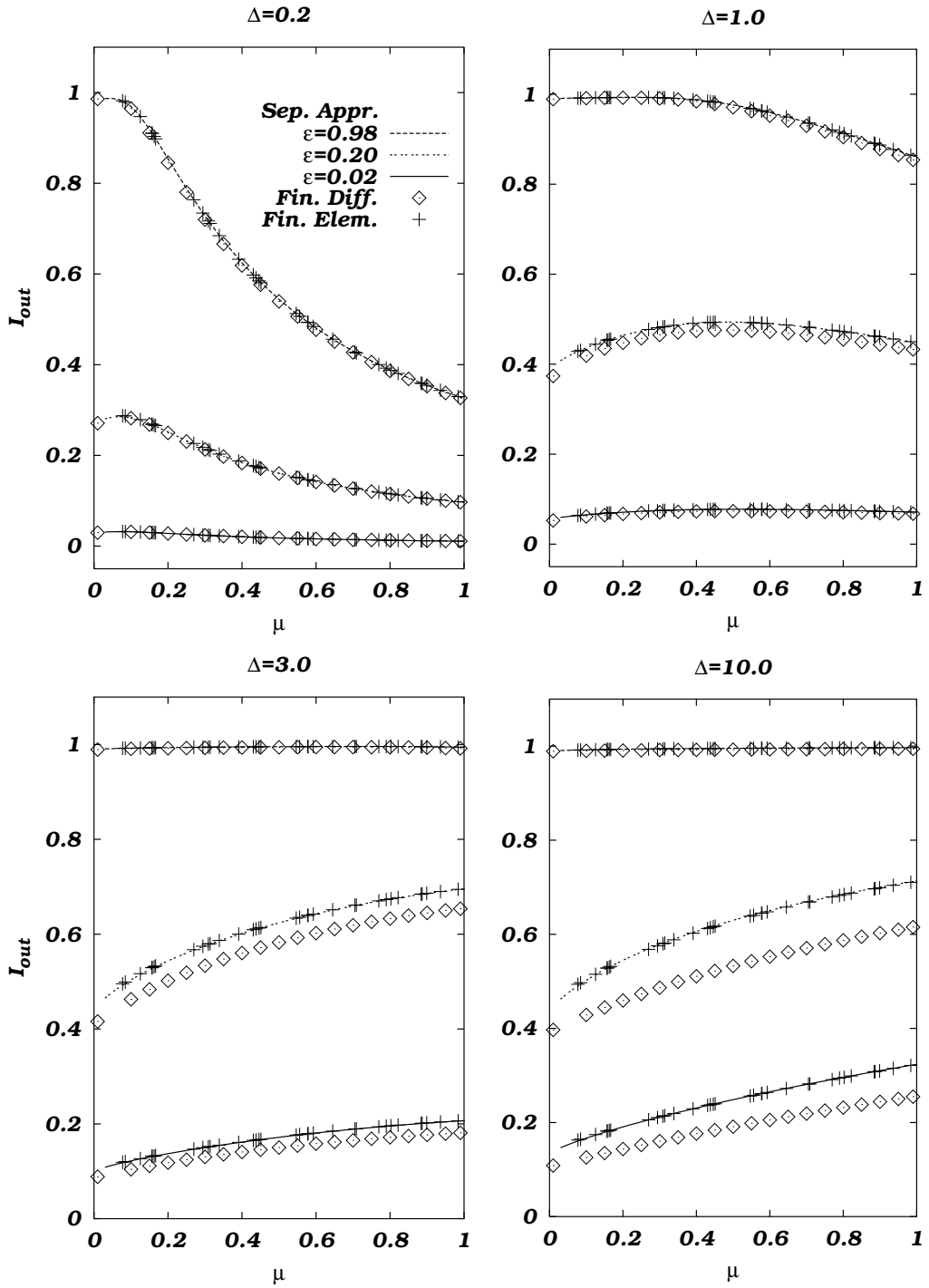

Fig. 5.4: Angular distribution of the outgoing intensity in the 5th approximation order. The results are compared with those of the Finite Difference and Finite Element methods. The Planck function is constant, $B = 1$.

Chapter 6

Results

This chapter consists of the results of our calculations of the accretion disk radiation field. In the beginning we discuss a simple case of a homogeneous disk in order to investigate the influence of the kinematic properties of the disk on the line profile. Then the general case is considered. Here we investigate effects caused by all the first and second order corrections of the perturbation theory. The calculation of the radiation field divides into two parts. The first part deals with the local line formation and consists of calculating the spectral and angular distribution of the emerging radiation at each point on the disk surface. The second part consists of calculating, as a function of inclination, the line profile by summing all local contributions with appropriate Doppler shifts resulting from the rotational motion.

6.1 Homogeneous accretion disk

The calculation of the line radiation is more complicated than the calculation of the continuum because much more factors affect the process of the line formation. The careful investigation of each of these factors is necessary in order to recognize the effects caused by it in the line profile. Obviously, the best way to do this is to consider such a model where the investigating factor dominates other ones.

The simplest model for the line profiles which permits us to investigate the influence of the kinematic structure of the disk on the radiation field is a homogeneous, Keplerian disk (Adam 1990; Papkalla 1995). We assume that the temperature does not vary in the vertical and radial directions and set $B = 1$. The extinction in the continuum χ_c and at the line center χ_0^l are constant too and considered as parameters. The advantage of this model is that one can study the effect of the de-excitation coefficient ε and the total optical depth at the line center $\tau_0^l = \chi_0^l H$ and in continuum $\tau_c = \Delta = \chi_c H$. H is the height of the disk above the midplane.

Since the disk is homogeneous, many terms in equations (3.2), (3.7) and (3.13) disappear. Among the remaining ones, only the following five may give a remarkable contribution to the local line profile

$$I^{(0)}(\lambda,\mu) = \frac{f_\lambda}{\mu}\int_{-\Delta}^{\Delta} e^{-\frac{f_\lambda}{\mu}(\Delta-\tau)}[(1-\varepsilon)J+\varepsilon B]\,d\tau, \tag{6.1}$$

$$I_{\rm s}^{(1)}(\lambda,r,\mu) = \frac{1-\mu^2}{\mu}\frac{3\lambda}{4c}\sqrt{\frac{GM}{r^3}}\frac{1}{\chi_c}\int_{-\Delta}^{\Delta} e^{-\frac{f_\lambda}{\mu}(\Delta-\tau)}\frac{\partial I^{(0)}}{\partial\lambda}\,d\tau, \tag{6.2}$$

$$I_{\rm 2s}^{(2)}(\lambda,r,\mu) = \frac{1-\mu^2}{\mu}\frac{3\lambda}{4c}\sqrt{\frac{GM}{r^3}}\frac{1}{\chi_c}\int_{-\Delta}^{\Delta} e^{-\frac{f_\lambda}{\mu}(\Delta-\tau)}\frac{\partial I_{\rm s}^{(1)}}{\partial\lambda}\,d\tau, \tag{6.3}$$

$$I_{\rm s2c}^{(2)}(\lambda,r,\mu) = \frac{3}{4}\,I_{\rm c2s}^{(2)}(\Delta) = \frac{\sqrt{1-\mu^2}}{\mu}\frac{1}{\chi_c}\frac{2}{r}\int_{-\Delta}^{\Delta} e^{-\frac{f_\lambda}{\mu}(\Delta-\tau)}I_{\rm s}^{(1)}\,d\tau \tag{6.4}$$

We do not consider $I_0^{(2)}$ defined in equation (3.13) for the reason of efficiency. This intensity obeys the integro-differential equation (3.19) whose solution is the most computationally expensive part of the whole perturbation approach. Although the computations are large, this intensity contribution to the final solution is negligibly small in comparison with the other ones.

Substituting into equation (6.2) the wavelength derivative

$$\frac{\partial}{\partial\lambda}I^{(0)}(\tau,\lambda,r,\mu) = \frac{1}{\mu}\int_{-\Delta}^{\tau} e^{-\frac{f_\lambda}{\mu}(\tau-\tau')}\left[\mathcal{S}'-\frac{f'_\lambda}{\mu}(\tau-\tau')\,\mathcal{S}\right]d\tau' \tag{6.5}$$

with the modified source function $\mathcal{S}=f_\lambda[(1-\varepsilon)J+\varepsilon B]$ and rearranging the order of integration

$$\int_{-\Delta}^{\Delta}d\tau\int_{-\Delta}^{\tau}f(\tau,\tau')\,d\tau' = \int_{-\Delta}^{\Delta}d\tau'\int_{\tau'}^{\Delta}f(\tau,\tau')\,d\tau$$

we obtain the expression for the first order correction

$$I_{\rm s}^{(1)}(\lambda,r,\mu) = \frac{1-\mu^2}{\mu^2}\frac{3}{4c}\sqrt{\frac{GM}{r^3}}\frac{1}{\chi_c}\,\mathcal{R}_{\rm s}(\lambda,\mu) \tag{6.6}$$

where

$$\mathcal{R}_{\rm s}(\lambda,\mu) = \lambda\int_{-\Delta}^{\Delta} e^{-\frac{f_\lambda}{\mu}(\Delta-\tau)}(\Delta-\tau)\left[\mathcal{S}'-\frac{f'_\lambda}{2\mu}(\Delta-\tau)\,\mathcal{S}\right]d\tau$$

The prime denotes the differentiation with respect to λ and f_λ is defined in (2.9). In a similar way, the substitution of $\partial I_{\rm s}^{(1)}/\partial\lambda$ and $I_{\rm s}^{(1)}$ into equations (6.3) and (6.4) and the following re-arrangement

$$\int\limits_{-\Delta}^{\Delta} d\tau \int\limits_{-\Delta}^{\tau} d\tau' \int\limits_{-\Delta}^{\tau'} f(\tau,\tau',\tau'')\,d\tau'' = \int\limits_{-\Delta}^{\Delta} d\tau'' \int\limits_{\tau''}^{\Delta} d\tau' \int\limits_{\tau'}^{\Delta} f(\tau,\tau',\tau'')\,d\tau$$

give us the expressions for the second order corrections

$$I_{\rm s2c}^{(2)}(\lambda,r,\mu) = \frac{(1-\mu^2)^{3/2}}{\mu^3}\,\frac{3}{4c}\,\sqrt{\frac{GM}{r^5}}\,\frac{1}{\chi_c^2}\,\mathcal{R}_{\rm s2c}(\lambda,\mu) \tag{6.7}$$

$$I_{\rm 2s}^{(2)}(\lambda,r,\mu) = \frac{(1-\mu^2)^{2}}{\mu^3}\,\frac{9}{32c}\,\frac{GM}{r^3}\,\frac{1}{\chi_c^2}\,\mathcal{R}_{\rm 2s}(\lambda,\mu) \tag{6.8}$$

with

$$\mathcal{R}_{\rm s2c}(\lambda,\mu) = \lambda \int\limits_{-\Delta}^{\Delta} e^{-\frac{f_\lambda}{\mu}(\Delta-\tau)}(\Delta-\tau)^2\left[\mathcal{S}' - \frac{f'_\lambda}{3\mu}\,(\Delta-\tau)\,\mathcal{S}\right] d\tau$$

$$\begin{aligned}\mathcal{R}_{\rm 2s}(\lambda,\mu) &= \lambda \int\limits_{-\Delta}^{\Delta} e^{-\frac{f_\lambda}{\mu}(\Delta-\tau)}(\Delta-\tau)^2\left[(\lambda\mathcal{S}')' + \frac{\lambda\,(f'_\lambda)^2}{4\mu^2}\,(\Delta-\tau)^2\,\mathcal{S}\right.\\ &- \left.\frac{1}{3\mu}\,(\Delta-\tau)\left((\lambda f'_\lambda\mathcal{S})' + 2\lambda f'_\lambda\mathcal{S}'\right)\right] d\tau\end{aligned}$$

Thus, the assumption of the constant extinction coefficient χ_c leads to the possibility of independent calculation of the zero order intensity and its high order corrections. We need for that the source function and its wavelength derivatives only. The memory requirements and computational time reduce significantly because we need to calculate the intensity only in the reference points ($\tau = \Delta$ in the above case) and intensities in many irrelevant points are no longer necessary.

The final solution in the comoving frame with the explicit dependences of r and ϕ reads

$$\begin{aligned}I_{\rm tot}(\lambda,r,\phi,\mu) &= I^{(0)}(\lambda,\mu) + \sin 2\phi\, I_{\rm s}^{(1)}(\lambda,r,\mu)\\ &+ \sin^2 2\phi\, I_{\rm 2s}^{(2)}(\lambda,r,\mu) + \frac{1}{4}\,\sin\phi\,(3+7\cos 2\phi)\, I_{\rm s2c}^{(2)}(\lambda,r,\mu)\end{aligned} \tag{6.9}$$

To compare the calculated intensity with the flux an observer would see we have to take into account all the local contributions with an appropriate Doppler shift. Thus the flux is given by

$$F_\lambda(\theta,\varphi) = \int\limits_0^{2\pi} d\psi \int\limits_{r_{\rm in}}^{r_{\rm out}} I\left(\lambda_0\left(1-\frac{1}{c}\sqrt{\frac{GM}{r}}\,\sin\theta\,\sin(\varphi-\psi)\right), r, \theta, \varphi, \psi\right) r\,dr$$

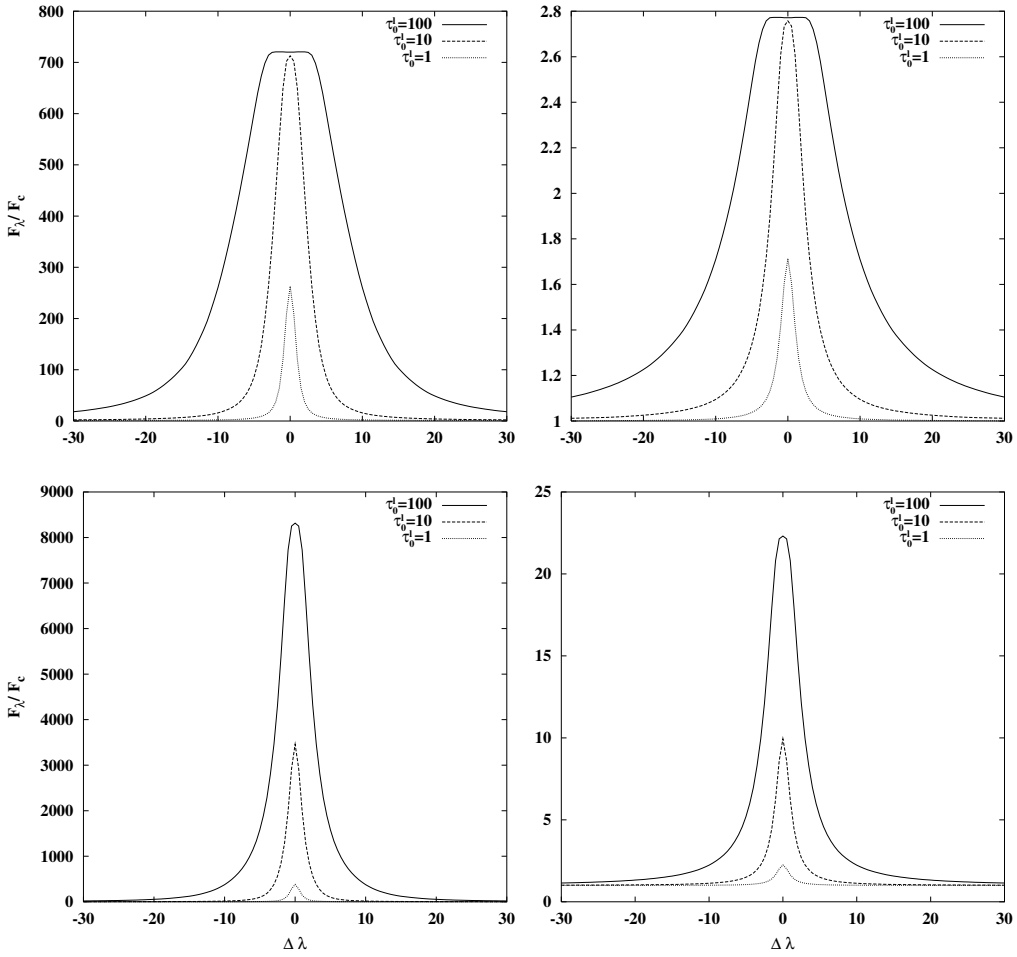

Fig. 6.1: Line profiles of the radiation emerging from a homogeneous CV disk ($B = 1$) perpendicular to its surface ($\mu = 1$) for the different combinations τ_0^l, τ_c and ε. *Left-hand part:* $\tau_c = 0.01$. *Right-hand part:* $\tau_c = 1$. *Top row:* $\varepsilon = 2 \times 10^{-2}$. *Bottom row:* $\varepsilon = 2 \times 10^{-4}$.

The example we consider is an accretion disk in a cataclysmic system. The model is defined by the disk inner radius $r_{\rm in} = 4 \cdot 10^9$ cm, outer radius $r_{\rm out} = 2.4 \cdot 10^{10}$ cm, the constant height above the midplane $H = 10^9$ cm, the mass of the central object $M = 0.5\, M_\odot$. The line at $\lambda_0 = 5000$Å has the Lorentz profile with $\gamma/2 = 1$Å. The parameters are $\varepsilon = 2 \cdot 10^{-2}$ and $2 \cdot 10^{-4}$, $\tau_0^l = 1$, 10 and 100, $\tau_c = \Delta = 10^{-2}$ and 1.

Fig. 6.1 shows the line profiles of the radiation emerging the disk perpendicular to its surface. Since the Doppler-broadening effect due to the disk rotation is absent in this case, we observe the intrinsic line profiles. The ratio F_λ/F_c is nothing else as $I_\lambda^{(0)}/I_c^{(0)}$ because of the factor $1 - \mu^2$ in equations (6.2)–(6.4). $I^{(0)}$ is defined by equation (6.1). Although these profiles were obtained by means of the separable approximation method, for their quali-

tative interpretation we apply the formulae of the two-stream approximation theory. Discrepances between the results of both the methods are shown in Fig. 4.2 on page 27.

According to (4.19) the intensity of radiation leaving a slab of half optical thickness τ_λ is given by

$$I_\lambda \;=\; I_\lambda^{(0)} \approx \frac{2\sqrt{\varepsilon}\tanh(\sqrt{\varepsilon}\tau_\lambda)}{1+\sqrt{\varepsilon}\tanh(\sqrt{\varepsilon}\tau_\lambda)}\,B \tag{6.10}$$

where

$$\tau_\lambda = \Delta + 0.5\,\pi\,\gamma\,\tau_0^l\,\varphi_\lambda \tag{6.11}$$

For an optically thin line we can use the McLaurin expansion of (6.10) which gives

$$I_\lambda \approx (\varepsilon\tau_\lambda - \varepsilon^2\tau_\lambda^2)\,B \tag{6.12}$$

When $\sqrt{\varepsilon}\tau_\lambda > 1$ the specific intensity cannot be larger than

$$I_\lambda = \frac{2\sqrt{\varepsilon}}{1+\sqrt{\varepsilon}}\,B, \tag{6.13}$$

and the line width increases for increasing τ_0^l.

For $\sqrt{\varepsilon}\tau_\lambda \gg 1$ lines saturate with the saturation level $I_{\max}$ defined by (6.13). However the far wings have $\sqrt{\varepsilon}\tau_\lambda < 1$. They may yet grow for increasing τ_0^l and so contribute additional width.

The values of the line maxima shown in Fig. 6.1 depend also on the intensity of the continuum I_c. In the given case the continuum is optically thin and therefore formula (6.12) with Δ instead of τ_λ can be used for the qualitative estimates of the continuum radiation. If, however, τ_c increases, the continuum level approaches $I_{\max}$ and the lines disappear into the continuum.

The spatially integrated line profiles of the radiation in direction $\varphi = 0$ for the disk observed at different inclinations are presented in Figs. 6.2 and 6.3. With the exception of the optically thick line $\tau_0^l = 100$ in the disk with $\varepsilon = 2\cdot 10^{-2}$ all graphs show double-peaked profiles which are due to the disk rotation. The position of the line peaks corresponds to the Keplerian velocity at the outer radius of the disk and is given by

$$\Delta\lambda_p \approx \pm\,\lambda_0\,\frac{v(r_{\rm out})}{c}\,\sqrt{1-\mu^2} \tag{6.14}$$

The lines are strong for low inclinations and disappear when $\mu \to 0$ because the disk becomes optically thick in the continuum when viewed nearly edge-on.

The effect of the disk outer radius is illustrated in Fig. 6.4. According to (6.14) decreasing disk radius has the effect of increasing the average disk

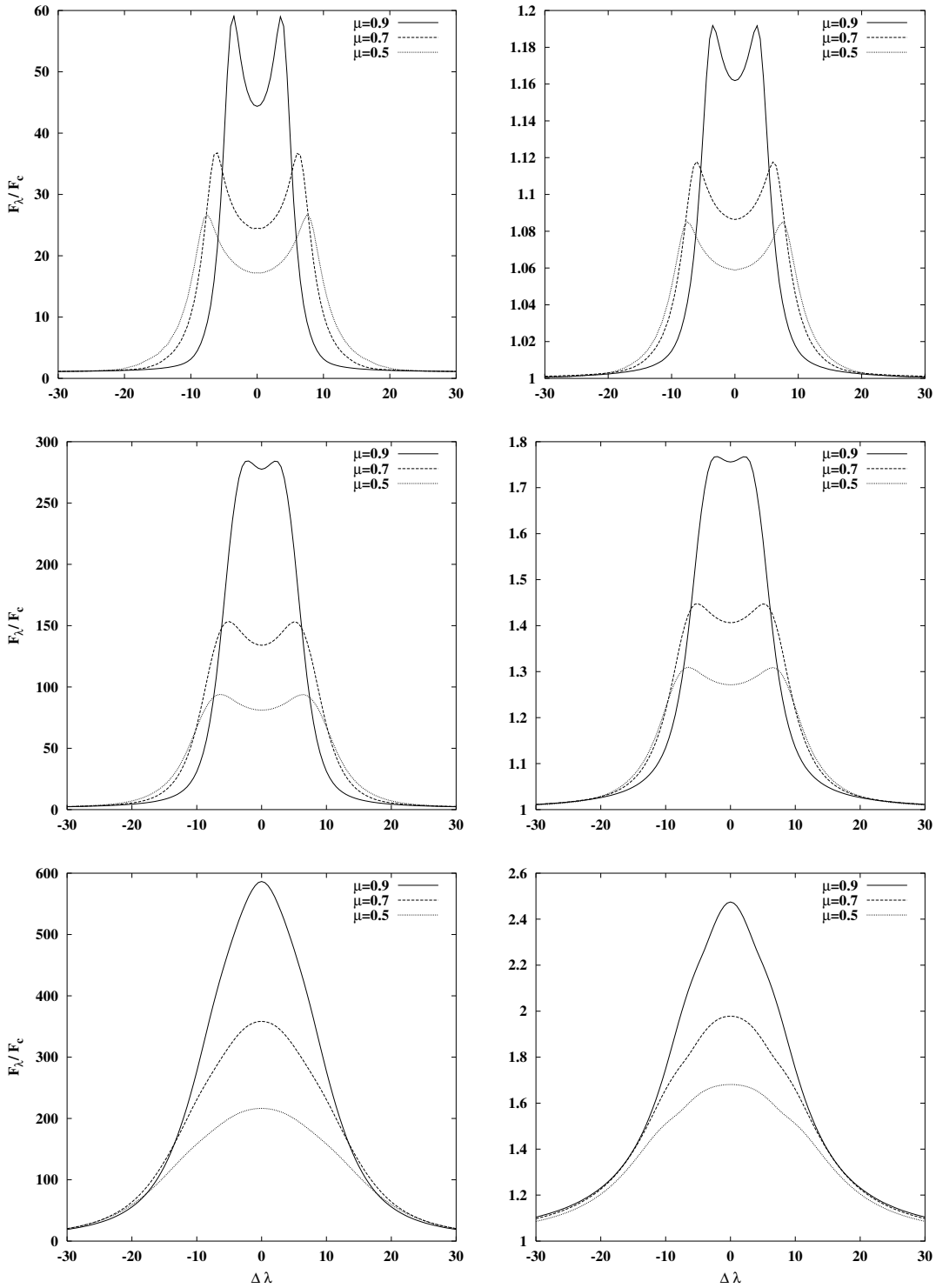

Fig. 6.2: Line profiles for a homogeneous CV disk ($B = 1$, $\varepsilon = 2 \times 10^{-2}$) observed at different inclinations for the different combinations τ_c and τ_0^l. *Left-hand part:* $\tau_c = 0.01$. *Right-hand part:* $\tau_c = 1$. *Top row:* $\tau_0^l = 1$. *Middle row:* $\tau_0^l = 10$. *Bottom row:* $\tau_0^l = 100$.

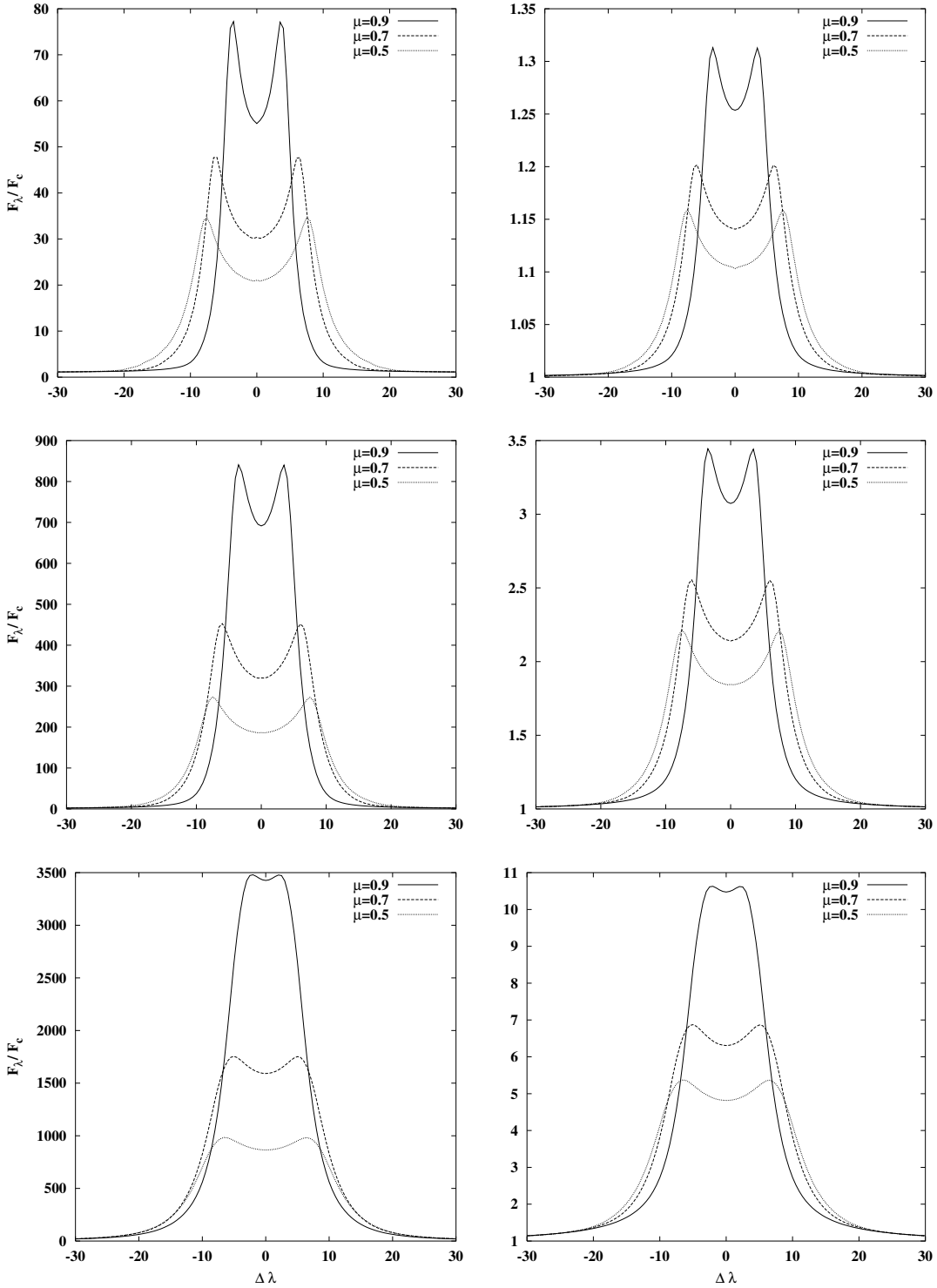

Fig. 6.3: Line profiles for a homogeneous CV disk ($B = 1$, $\varepsilon = 2 \times 10^{-4}$) observed at different inclinations for the different combinations τ_c and τ_0^l. *Left-hand part:* $\tau_c = 0.01$. *Right-hand part:* $\tau_c = 1$. *Top row:* $\tau_0^l = 1$. *Middle row:* $\tau_0^l = 10$. *Bottom row:* $\tau_0^l = 100$.

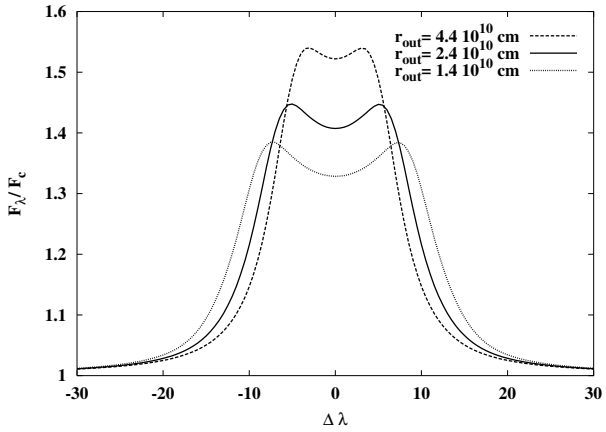

Fig. 6.4: Line profiles of a disk with the different outer radius. The data are for $\mu = 0.7$, $B = 1$, $\varepsilon = 2 \times 10^{-2}$, $\tau_c = 1$, $\tau_0^l = 10$.

Keplerian velocity and widening the line profile. The line becomes stronger because of larger surface area of the disk with larger outer radius.

The line profiles in the bottom row of Fig. 6.2 remains single-peaked even for higher inclinations. The reason is the large intrinsic line broadening that prevents the peak separation. The broad single-peaked emission lines are present in many cataclysmic variables (Stover et al. 1980; Young et al. 1981). In particular, there are eclipsing systems that have symmetric, single-peaked profiles and yet display an evolution through eclipse that suggests the emission does originate in a rotating disk. The Stark effect as a reason of the single-peaked profile is discussed by Lin et al. (1988). Another physical mechanism is discussed by Murray & Chiang (1996).

6.2 General case

The disk considered so far is a major oversimplification. On one hand a real disk is not flat but should obey some profile the derivation of which is the challenge for researchers. In some models, however, the height of the disk above the midplane as a function of radius is approximated by a line running at some constant angle that is the free model parameter. On the other hand the accretion disk is not isothermal. Temperature at the midplane and the surface as well as at the inner and the outer disk edges may differ significantly. The temperature variation with depth and radius is crucial in the line formation process.

In order to test the method we use for the solution of multi-dimensional radiative transfer equation, the previous accretion disk model is not sufficient.

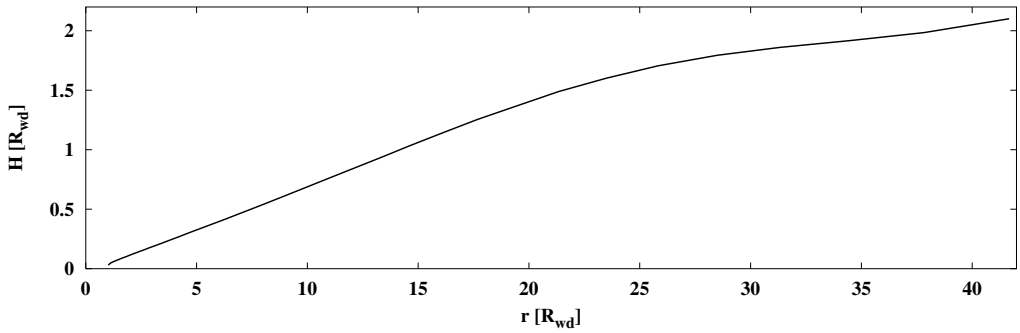

Fig. 6.5: The height of a disk above the midplane as a function of the radial distance.

To give an estimate of the time and memory requirements as well as to define the range of the applicability of the perturbation theory, a model with the number of simplifications as small as possible is necessary. For these purposes we use a model of an accretion disk constructed in a self-consistent way as described by Shaviv & Wehrse (1991). The parameters of the model are chosen in such a way to provide the smallness of gradients in the radial direction relative to ones in the vertical direction, and the rotational velocity of the disk matter much smaller than speed of light. This disk in a cataclysmic variables system with the following accretion rate, inner and outer radii

$$\begin{aligned} \dot{M} &= 10^{17}\ \mathrm{gr/s}, \\ r_{\mathrm{in}} &= 6.08 \cdot 10^{8}\ \mathrm{cm}, \quad (v_\varphi = 4685\ \mathrm{km/s}) \\ r_{\mathrm{out}} &= 2.50 \cdot 10^{10}\ \mathrm{cm}, \quad (v_\varphi = 731\ \mathrm{km/s}) \end{aligned}$$

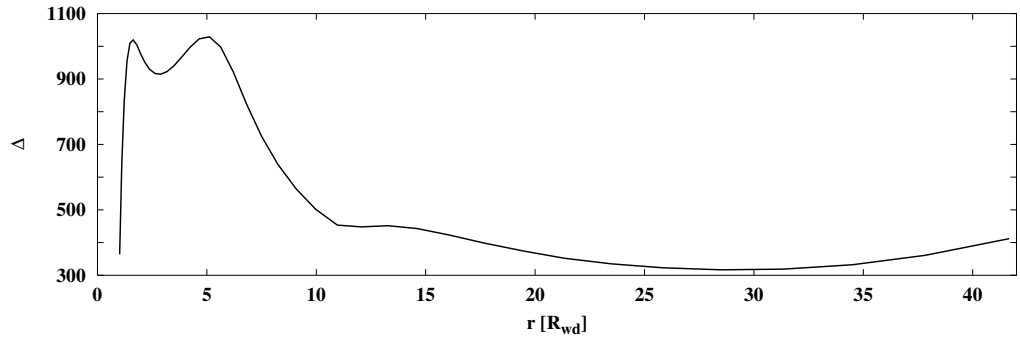

Fig. 6.6: The total Rosseland optical depth above the disk midplane as a function of the radial distance.

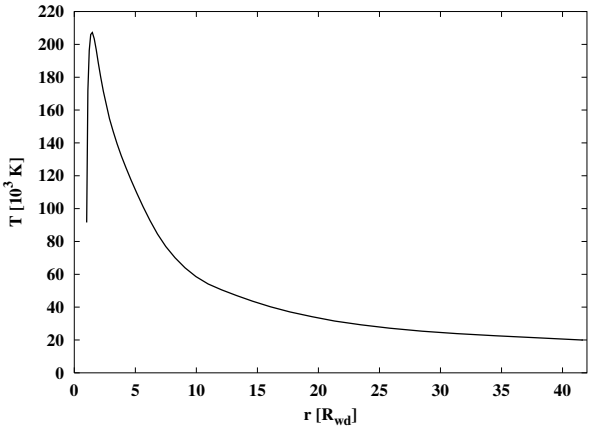

Fig. 6.7: Radial run of the temperature in the midplane of a disk

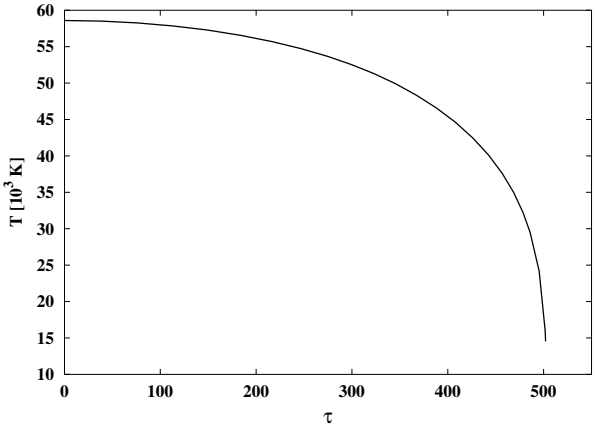

Fig. 6.8: Vertical run of the temperature at $r = 10R_{\rm wd}$

rotates around the central object that is a white dwarf with

$$R_{\rm wd} = 6 \cdot 10^8 {\rm cm}, \qquad M = M_\odot$$

The disk is not flat. Instead, its height obtained iteratively from the hydrostatic calculations varies with radius as shown in Fig. 6.5. As one can see this is the geometrically thin disk where the ratio of the height to the radius for the outer edge is approximately 20. Apart from the previous case, this disk is optically thick in the continuum. The complex form of the total Rosseland optical thickness above the midplane is shown in Fig. 6.6.

Since the temperature changes both in vertical and radial direction, (examples of such distributions are given in Figs. 6.7 and 6.8), each term in (3.7) and (3.13) has to be considered. Thus we can investigate the influence not only of the kinematic properties but also of the radial and vertical structures of the disk on the line profile.

Again we take a line at $\lambda_0 = 5000$Å with the Lorentz profile. The value of the damping constant $\gamma = 2$Å is chosen for convenience. The disk is always viewed in the direction $\varphi = 0$. We study the effect of the de-excitation coefficient ε which is assumed to be constant, the line strength ξ_0 (see equation

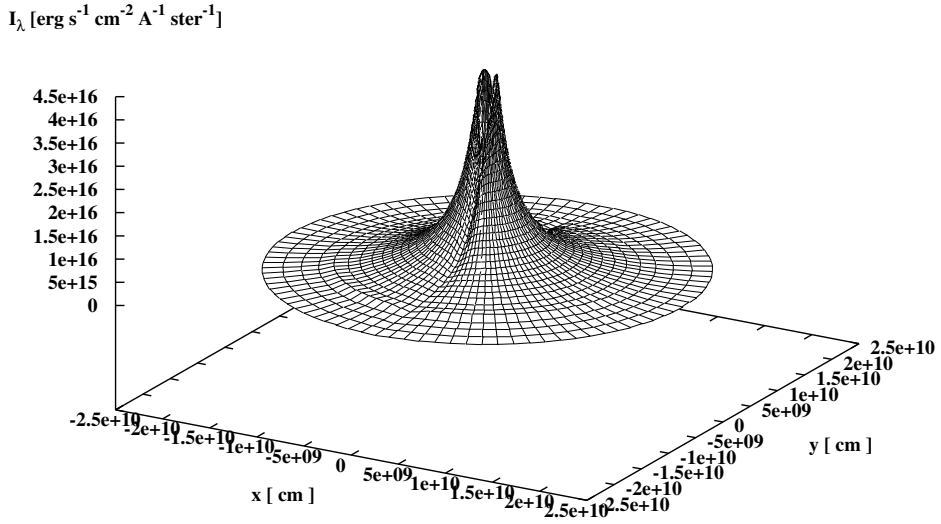

Fig. 6.9: Intensity distribution in the observer's frame of a disk with $\varepsilon = 0.5$ viewed at inclination $\mu = 0.8$ ($\approx 37^\circ$) in the direction $\varphi = 0$. The disk is observed at $\lambda = \lambda_0$. The line strength parameter ξ_0 is 10.

(2.9)) and the inclination.

The choice of the parameters $\xi_0 = 10$, $\varepsilon = 0.5$ and $\mu = 0.8$ results in the brightness distribution on the disk surface shown in Fig. 6.9. Such an intensity map was obtained by taking into account the solution of the zero order equation calculated in the 6th separable approximation, and all the first and second order corrections with the exception of $I_0^{(2)}$ defined by (3.19). An appropriate Doppler shift was made in each point to get an intensity map in the observer's frame.

The advantage of the present perturbation approach is that the influence of such factors as the Doppler term in the radiative transfer equation, the run of quantities with radius and their radial gradients on the local and spatially integrated line profile can be separately investigated by considering the corresponding terms in (3.7) and (3.13). Fig. 6.10 shows the variation of the specific intensity with the angle ψ at $r = 10R_{\rm wd}$ in the disk with the parameters mentioned above. The solid curve represents the solution of the zero order equation whereas the dashed curves show the changes caused by the higher order corrections. In Fig. 6.11 the spatially integrated line profiles are shown. The solid curve depicts the flux an observer would see when he

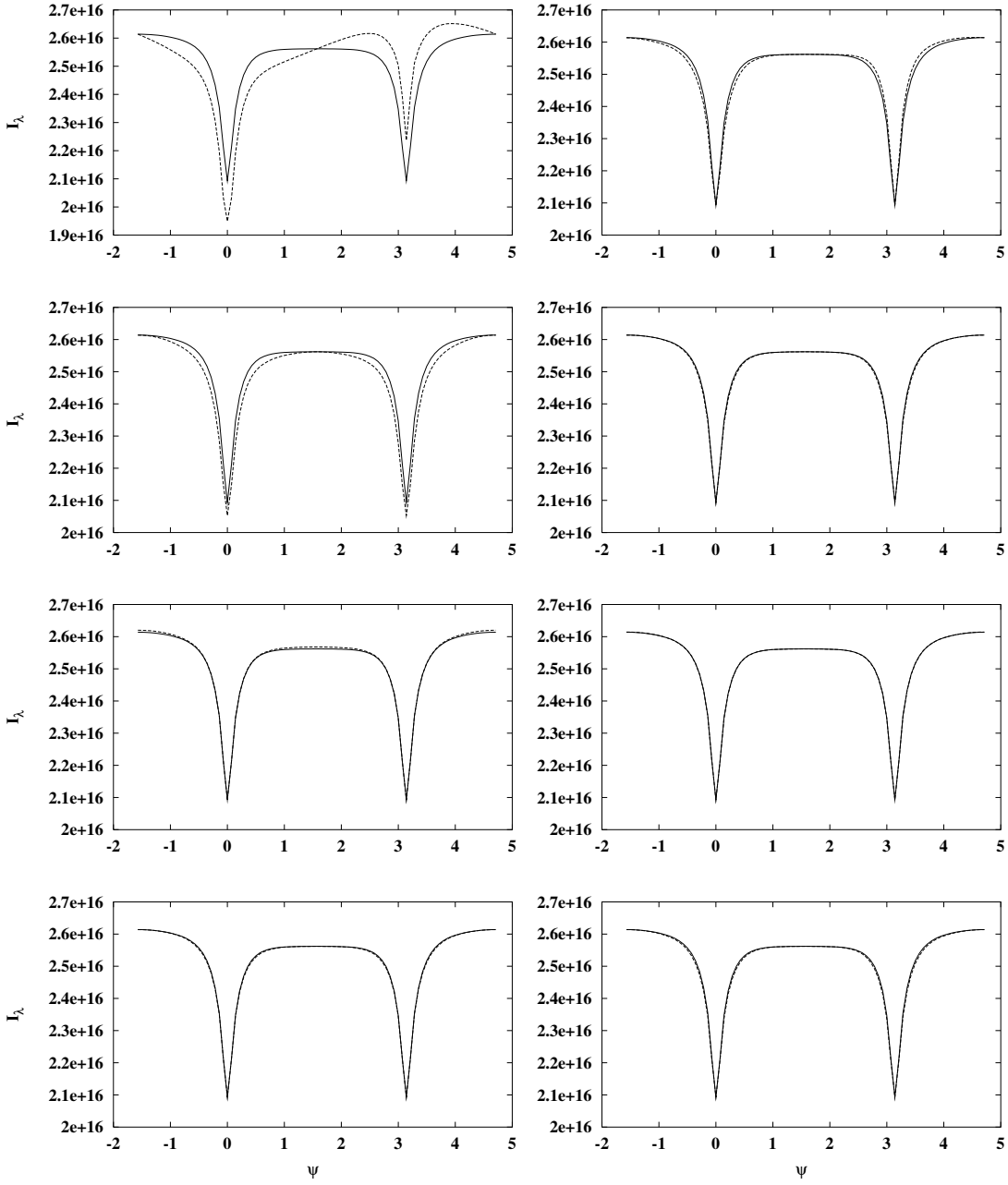

Fig. 6.10: The variation of the emerging intensity with the angle ψ at $r = 10R_{\rm wd}$ in the observer's frame. The solid curves correspond to the solution of the zero order equation $I^{(0)}$. The dashed curves show an effect of the different terms in equations (3.7) and (3.13): *1st row, left*: $I_{\rm c}^{(1)}$; *1st row, right*: $I_{\rm s}^{(1)}$; *2nd row, left*: $I_{\rm c}^{(2)}$; *2st row, right*: second part of $I_{\rm c2s}^{(2)}$; *3rd row, left*: $I_{\rm 2s}^{(2)}$; *3rd row, right*: first part of $I_{\rm c2s}^{(2)}$; *4th row, left*: $I_{\rm s}^{(2)}$; *4th row, right*: $I_{\rm s2c}^{(2)}$. The corresponding trigonometric functions in (3.7) and (3.13) are included in each term. The data are for $\mu = 0.8$, $\xi_0 = 10$, $\varepsilon = 0.5$.

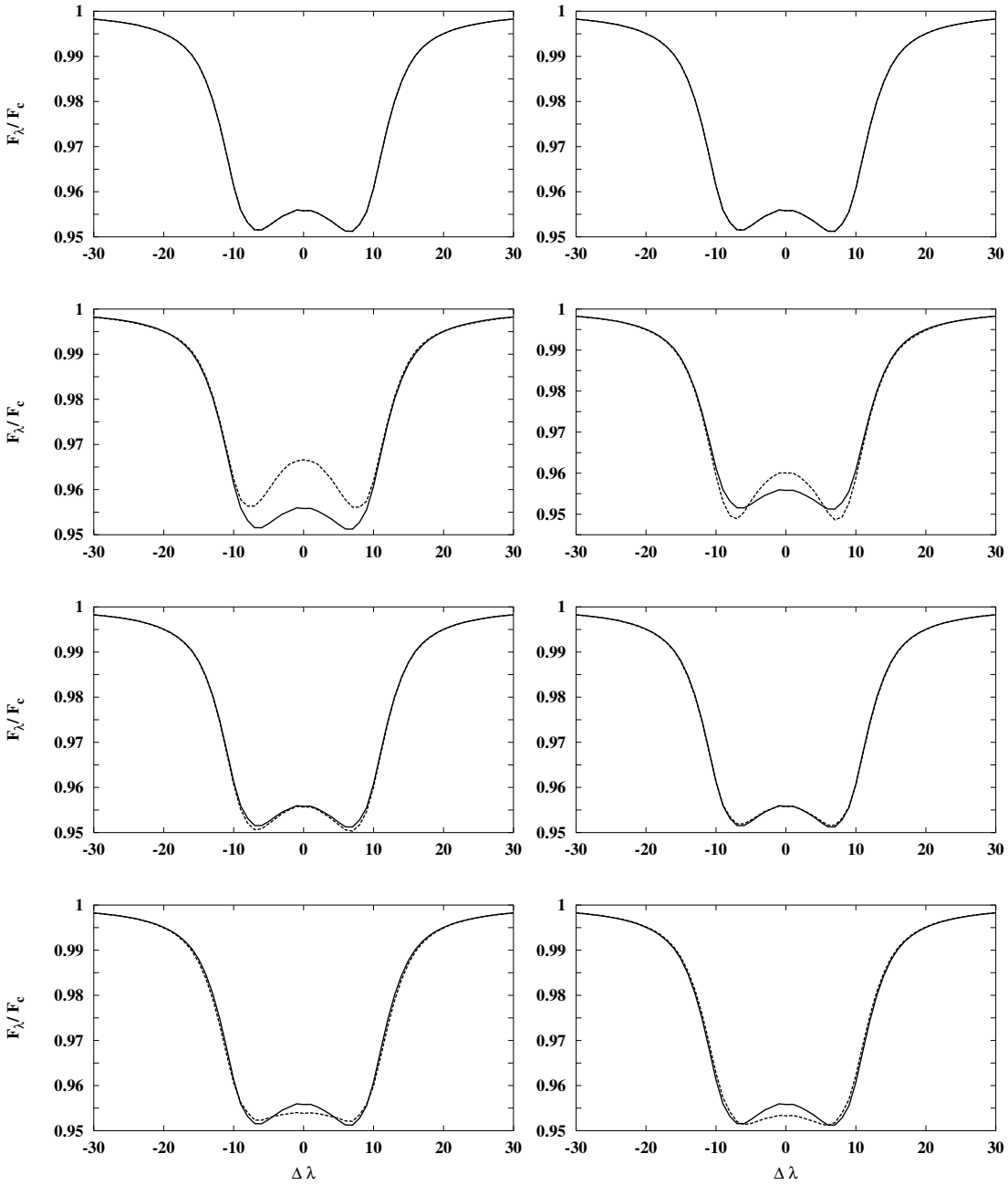

Fig. 6.11: The integrated line profile of a disk with parameters: $\mu = 0.8$, $\xi_0 = 10$, $\varepsilon = 0.5$. The solid curves represent the solution of the zero order equation. The dashed curves show the changes caused by the higher orders corrections. The arrangement of the graphs is the same as in Fig. 6.10.

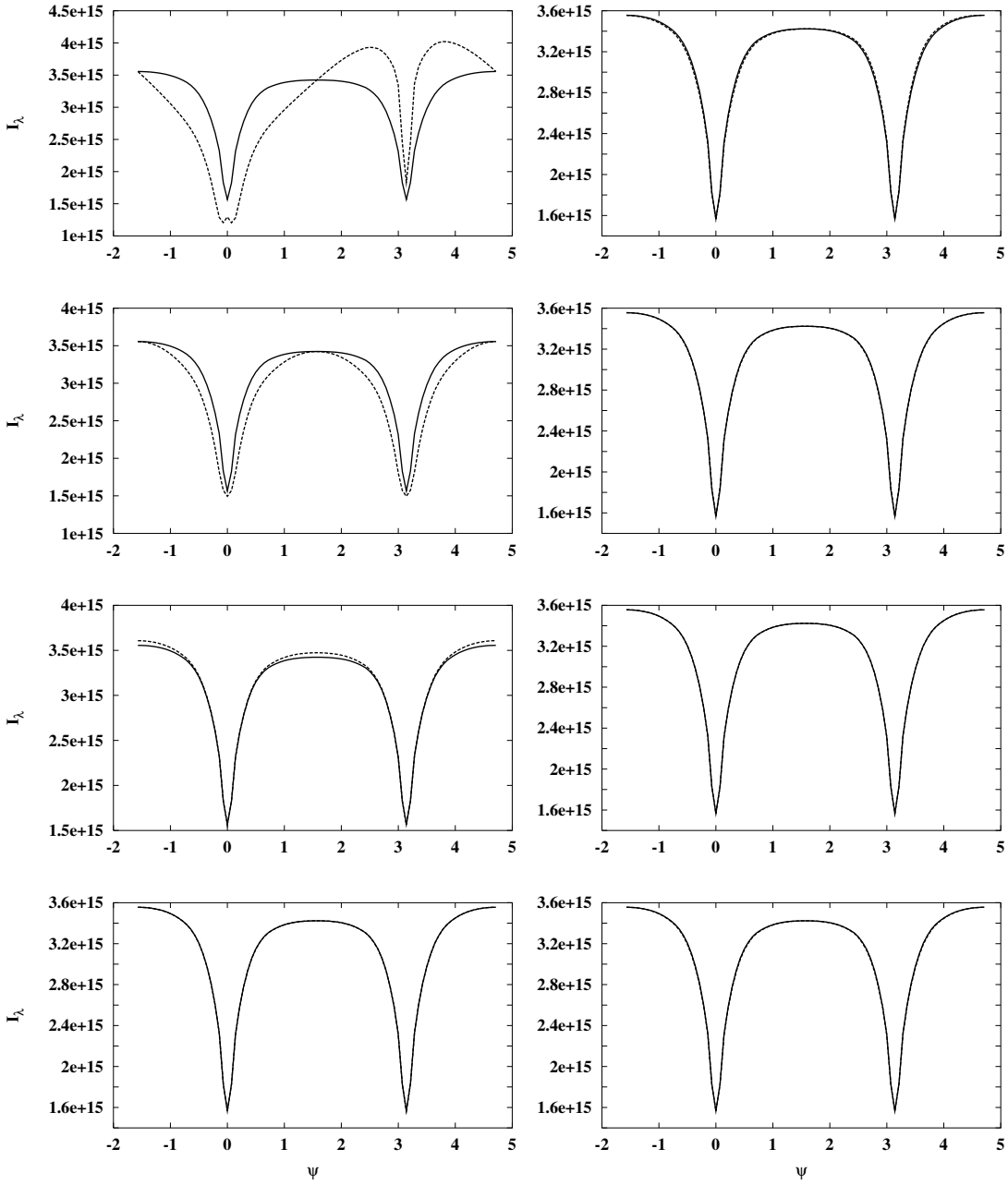

Fig. 6.12: The variation of the emerging intensity with the angle ψ at $r = 10R_{\rm wd}$ in the observer's frame. The solid curves correspond to the solution of the zero order equation $I^{(0)}$. The dashed curves show an effect of the different terms in (3.7) and (3.13): *1st row, left*: $I_{\rm c}^{(1)}$; *1st row, right*: $I_{\rm s}^{(1)}$; *2nd row, left*: $I_{\rm c}^{(2)}$; *2st row, right*: second part of $I_{\rm c2s}^{(2)}$; *3rd row, left*: $I_{\rm 2s}^{(2)}$; *3rd row, right*: first part of $I_{\rm c2s}^{(2)}$; *4th row, left*: $I_{\rm s}^{(2)}$; *4th row, right*: $I_{\rm s2c}^{(2)}$. The corresponding trigonometric functions in (3.7) and (3.13) are included in each term. The data are for $\mu = 0.7$, $\xi_0 = 100$, $\varepsilon = 0.02$.

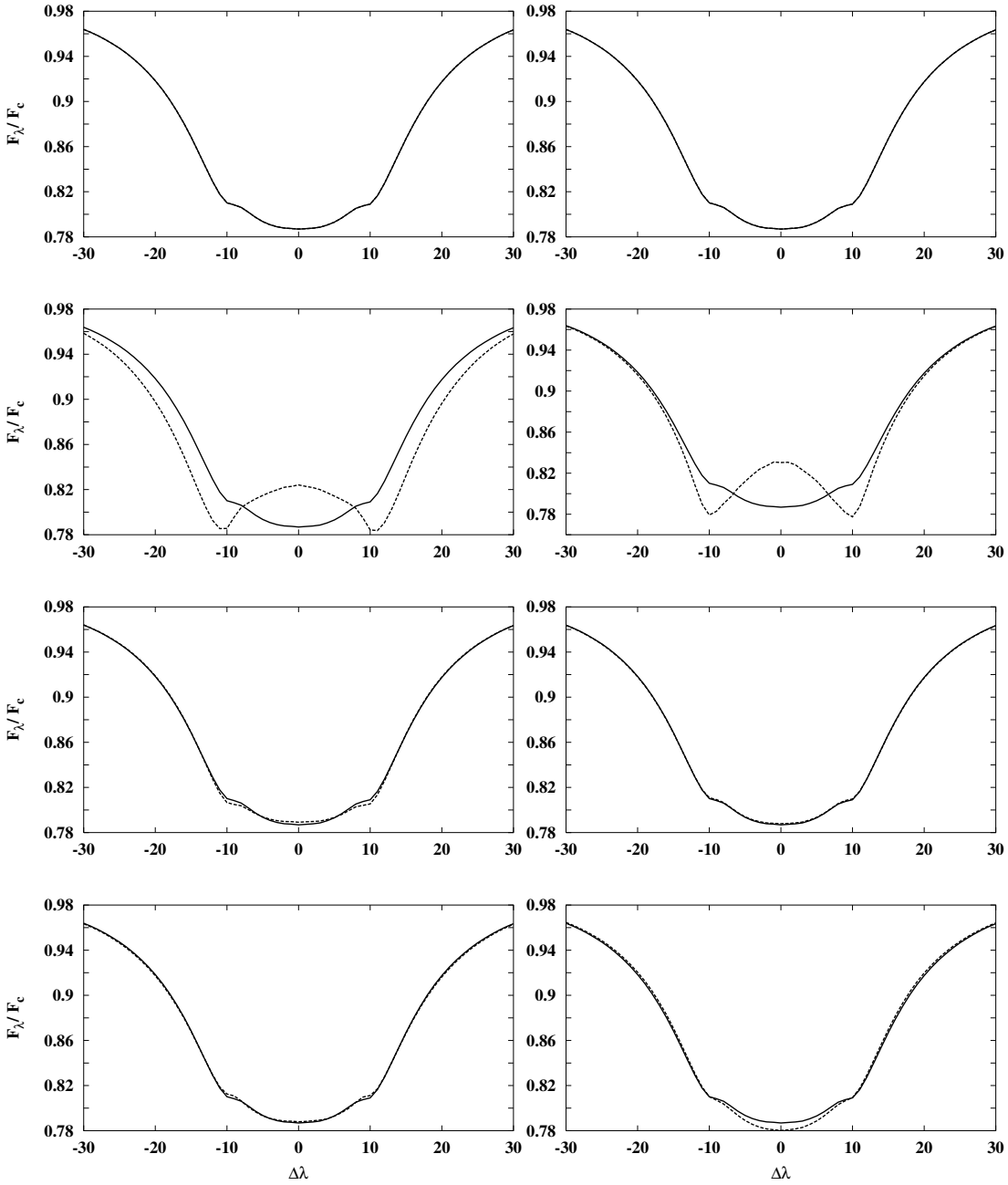

Fig. 6.13: The integrated line profile of a disk with parameters: $\mu = 0.7$, $\xi_0 = 100$, $\varepsilon = 0.02$. The solid curves represent the solution of the zero order equation. The dashed curves show the changes caused by the higher orders corrections. The arrangement of the graphs is the same as in Fig. 6.12.

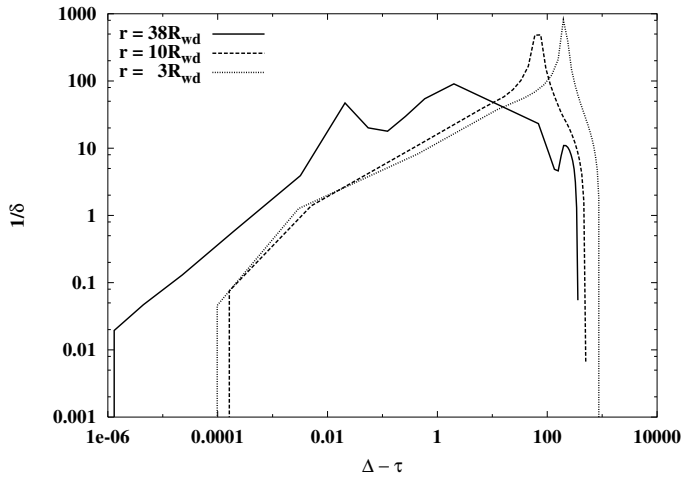

Fig. 6.14: Variation of $1/\delta = \left|\frac{\partial T}{\partial z} \Big/ \frac{\partial T}{\partial r}\right|$ with optical depth at different radii.

considers the disk as a system of independent rings, each of them radiating as a plane-parallel slab. The line profile is distorted when the different motions of the rings, their interactions with each other etc. are taken into account. Such distortions are illustrated by the dashed curves. The same quantities are shown in Figs. 6.12 and 6.13 but for the disk with parameters: $\xi_0 = 100$, $\varepsilon = 0.02$ and $\mu = 0.7$.

The changes made by the first order corrections are shown in the first rows of all figures. The largest changes in the local line profile are caused by $I_{\rm c}^{(1)}$ (Eq. (3.11)). The large damping constant and a slow disk rotation make the effect of $I_{\rm s}^{(1)}$ (Eq. (3.12)) not so prominent. The closer we approach to the central object, the larger the distortions of the zero order solution become, making the perturbation approach irrelevant for the calculation of the radiation field in this region. Both functions vary with angle in such a way that after the integration over the angle ψ their contributions to the integrated line profile equal zero identically. Thus the second order corrections become of the prime interest. Each of them plays a certain role in the process of the line formation. The changes made by $I_{\rm c}^{(2)}$ (Eq. (3.20)) and the second term of $I_{\rm c2s}^{(2)}$ (Eq. (3.24)) are shown in the second rows. Being dependent on the radial gradients of the first order solutions they tend to deepen the central depression of the spatially integrated line profile making it V-shaped with the sharp peaks. The peak separation can appear even when the intrinsic broadening does not dispose of it. The peak separation becomes larger in the comparison with the zero order solution. Significant changes in the local line profile are caused mainly by $I_{\rm c}^{(2)}$. The effects of $I_{\rm 2s}^{(2)}$ (Eq. (3.22)) and $I_{\rm s2c}^{(2)}$ (Eq. (3.23)) show up mostly in the line center as shown in the forth rows. In

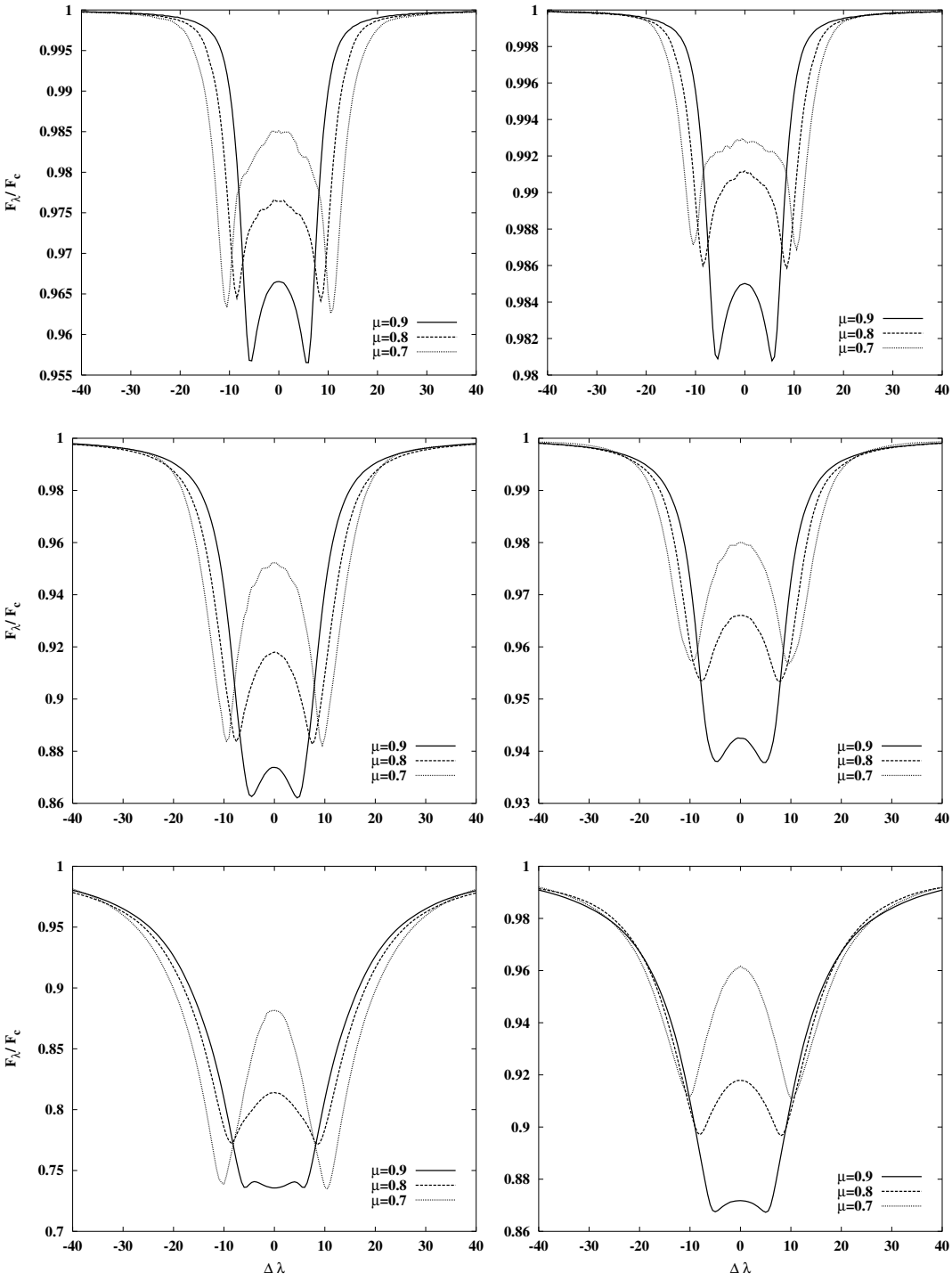

Fig. 6.15: Line profiles of the disk viewed at different inclinations for the different combinations ε and line strength ξ_0. *Left-hand part:* $\varepsilon = 0.02$. *Right-hand part:* $\varepsilon = 0.5$. *Top row:* $\xi_0 = 1$. *Middle row:* $\xi_0 = 10$. *Bottom row:* $\xi_0 = 100$.

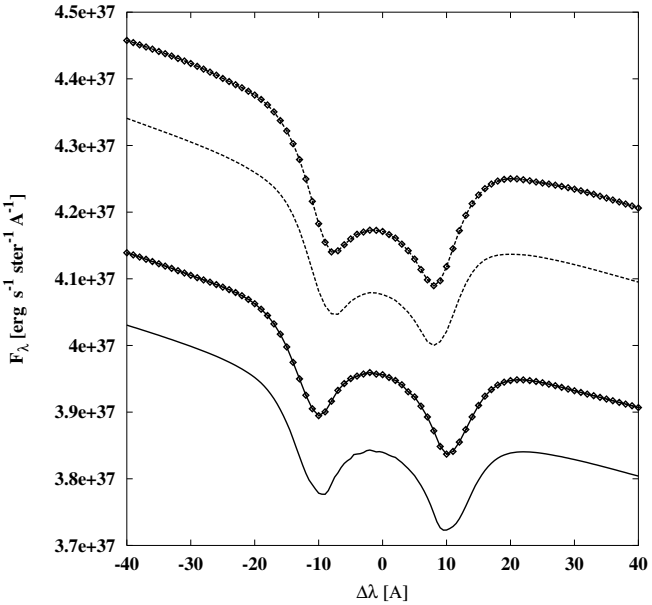

Fig. 6.16: Results obtained by means of the two-stream approximation (*with filled squares*) and the separable approximation methods (*without squares*). A disk with $\varepsilon = 0.5$ and $\xi_0 = 10$ is viewed at inclinations $\mu = 0.8$ (*dashed*) and $\mu = 0.7$ (*solid*).

contrast to the previous case these functions result in a shallow U-shaped valley between the peaks. The single-peaked lines become stronger. Because of the large damping constant and slow disk rotation the effects of these terms on the local line profile are not prominent. Remaining terms, namely $I_{\rm s}^{(2)}$ (Eq. (3.21)) and the first part of $I_{\rm c2s}^{(2)}$ (Eq. (3.24)) are of minor importance because of the small contributions to the line profile. The changes caused by them are shown in the third rows.

The final results where all the second order corrections taken into account are presented in Fig. 6.15 for the disk with the different combinations of parameters. The left column exhibits unusual variations of the line profile with inclination. The central depression becomes much deeper and appears even above the local continuum level at some inclinations. It seems to be strange also that the line peaks become larger in the disk viewed at larger inclinations. Such behaviors show up for all considered ε. The larger ε we take, the smaller μ is necessary to see these effects. The reason of such wrong variations consists in $I_{\rm c}^{(2)}$ and the second term of $I_{\rm c2s}^{(2)}$. Their absolute values increase when μ decreases and at some inclinations their contributions to the total solution become significant. However, as it follows from the principles of the perturbation theory, the higher order corrections must be much

smaller than the solution of the zero order equation. The opposite means that some criteria of the applicability of the perturbation approach are not fulfilled. Careful investigation of the temperature distribution has shown that the radial temperature gradients are much smaller than the gradients in the vertical direction in the layers where the continuum forms ($\Delta - \tau \approx 1$) as represented in Fig. 6.14. In the upper layers where the line radiation originates this relation does not hold anymore. Thus the perturbation approach breaks down, which is the main reason of the odd results.

Fig. 6.16 shows line profiles of the disk viewed at two different inclinations. The solid and dashed curves correspond to the results obtained by means of the application of the separable approximation method for the solution of the zero order equation. The two-stream approximation method used in the zero order of the perturbation theory gives the results depicted by the curves with the filled squares. As one can see the agreement between these two results is rather well. The systematic difference between the continuum levels does not exceed 3% which is very good bearing in mind those serious simplifications used in the two-stream approximation method. The shape of the peaks and the central depression are in the good agreement too. Thus the two-stream approximation can be successfully applied to obtain results with a reasonable accuracy. The calculations of the line profiles in the two-stream approximation takes less time (a factor of 4) because of the less CPU-time needed to solve the zero order equation.

Chapter 7

Discussion and conclusions

Accretion disks are found in a wide variety of astrophysical situations. Although their importance is obvious, the understanding of their spectra, density, temperature and velocity distributions is still quite limited. One of the reasons is unsatisfactory modeling of the vertical structure of these objects and, in particular, the radiation field. Attempts to interpret spectra of the accretion disks adopting the black body or stellar atmosphere theory are not successful as it was mentioned in the Introduction. Instead of this, the calculation of the spectra consistently gives more accurate model structure and predicted emergent radiation. In spite of the big progress in the development of the multidimensional radiative transfer codes, their incorporation into the self-consistent scheme meets problems related mainly to the bounded ability of the present computers. The representation of the accretion disk by a system of non-interacting concentric rings radiating as a plane-parallel static media simplifies the problem because 1D versions of the corresponding equations are used. Although such an approach gives quite accurate results (Shaviv & Wehrse 1991; El-Khoury & Wickramasinghe 2000; Nasser et al. 2001), some discrepancies between them and observations are still present.

In this thesis a perturbation solution of the multidimensional radiative transfer equation has been proposed. The zero order equation is the plane-parallel radiative transfer equation used in all mentioned above self-consistent calculations. The problem is no longer one-dimensional when the higher order perturbation equations are considered. These equations describe the interactions of the rings composing the accretion disk making the solution more realistic. Test calculations have shown that the changes in the continuum level as well as in the line profiles of the disk emergent radiation caused by the higher order corrections may be significant. Consequently, some changes may appear in the parameter estimation of an accretion disk if such the perturbation approach will be applyed, for example in the models of El-Khoury & Wickramasinghe (2000) or Nasser et al. (2001).

It is advantageous to use the radiative transfer equation with the Doppler term since in this case the system of differentially moving rings is described more properly and the influence of the velocity gradients on the radiation field is taken into account. In the models of the accretion disk used in the thesis the effect of the Doppler term on the final solution was not so prominent as for example the effect of the radial gradients. The reason is the slow disk rotation and the large damping constant.

One of the advantage of the present perturbation approach is the explicit dependence of the specific intensity on the directional angle ϕ (in the case of homogeneous disk there exists also the explicit dependence on radius r). The sources of the anisotropy of the radiation field such as the shear broadening or the temperature distribution are clearly seen and their effects can be investigated separately.

The solution of the radiative transfer equation is very fast due to the known solutions of the higher order perturbation equations and largely analytical methods applied to solve the zero order equation. In the model presented here we use a grid which consists of 99 points in the vertical direction, 40 radii and 40 wavelength points. For one value of μ the calculations takes 280 sec on a HP C240 computer. This includes the calculation of the mean intensity J in the 5th approximation order for the upper part of the disk (175 sec), the zero and first order specific intensities and all needed derivatives at all grid points (90 sec), and all the second order intensities on the disk surface (15 sec). Note that subsequent calculations for other inclinations take significantly less CPU-time since the most expensive calculation of J has been already carryed out.

Unfortunately the perturbation approach cannot be used for the calculation of the radiation field of all accretion disks. Only those disks whose rotational velocity is much less than the speed of light and the vertical gradients are much larger than the radial ones can be considered as such candidates. Accordingly, for the rings very close to the central object ($r < 3R_{\rm wd}$) or for the regions near the surface of the disk (optical depth measured from the surface is much less than unity) where the vertical temperature changes may be very small and radial gradients dominate, the perturbation approach can hardly be applied. The latter especially disappoints since many lines originate in such a region. The slight consolation is that there is no theory at the moment which can properly describe the processes in such critical regions (boundary layer, corona).

To solve the zero order equation two methods were used. One of the applied methods is the two-stream approximation method which is rather frequently used in applications. Under the simplifying assumption of this approach we have found the analytical solution of the plane-parallel radiative transfer equation in media with large variety of the internal distributions

of the de-excitation coefficient ε (linear, parabolic, with spikes etc.). To our knowledge this problem could be solved so far only numerically. Having obtained the analytical solutions for the different behaviors of ε, the solution of the inverse problem becomes possible. In particular, the deduction of the internal distribution of ε from observational data is facilitated in the case of isothermal media, since the characteristic behavior of the solution refers to the certain behavior of ε only. As an example, we have found the corresponding parameters of the constant and linear distributions of ε precisely. We have also considered the problem with the stochastic distribution of ε and proposed a new numerical method for its solution. In general, the two-stream approximation method provides us with the results whose accuracy strongly depends on the inclination of the chosen streams. The comparison with the exact solution has shown that in optically thick slabs a sufficient accuracy of 10% is achieved only when $\mu_0 \approx 0.35 \ldots 0.65$. In the optically thin media significant discrepances appear at grazing incidence.

Another method applying for the solution of the plane-parallel radiative transfer equation is the more sophisticated separable approximation method. The inhomogeneous integro-differential equation is solved without any discretization of the transport and integral operators. Since this method is largely analytical, the solution is fast even on small computers. The highly precise results can be obtained without much effort. The comparisons with the results of other methods have shown good agreement for a wide range of parameters.

Appendix A

Solution of equation (4.39)

Let us introduce new variables $\mathbf{\Phi}$ and $\mathbf{\Psi}$ [1]

$$\mathbf{J}_j = \mathbf{\Phi}_j - \mathbf{\Psi}_j, \qquad (j = 1, ..., N) \tag{A.1}$$

which obey the following recurrent equations

$$\begin{aligned} \mathbf{\Phi}_j &= \mathbf{U}_j \mathbf{\Phi}_{j-1}, & \mathbf{\Phi}_0 &= \mathbf{J}_0, \\ \mathbf{\Psi}_j &= \mathbf{U}_j \mathbf{\Psi}_{j-1} + \mathbf{K}_j B_{j-1}, & \mathbf{\Psi}_0 &= 0 \end{aligned}$$

Using notations

$$\begin{aligned} \mathbf{U}(j,k) &= \mathbf{U}(j,i+1)\mathbf{U}(i,k), \qquad (k \le i \le j), \\ \mathbf{U}(j,j) &= \mathbf{U}_j \end{aligned}$$

we get

$$\begin{aligned} \mathbf{\Phi}_j &= \mathbf{U}(j,1)\mathbf{\Phi}_0, \\ \mathbf{\Psi}_j &= \mathbf{B}(j,1) = \mathbf{U}(j,2)\mathbf{K}_1 B_0 + \mathbf{U}(j,3)\mathbf{K}_2 B_1 + ... \\ &+ \mathbf{U}_j \mathbf{K}_{j-1} B_{j-2} + \mathbf{K}_j B_{j-1}. \end{aligned}$$

The solution for j-th layer thus becomes

$$\mathbf{J}_j = \mathbf{U}(j,1)\mathbf{J}_0 - \mathbf{B}(j,1). \tag{A.2}$$

The value of $\mathbf{J}$ at the boundary reads

$$\mathbf{J}_N = J_N \mathbf{g} = \mathbf{U}(N,1)\mathbf{f}\, J_0 - \mathbf{B}(N,1).$$

[1] The designations used in this appendix are given in subsection 4.2.4. With the exception of few cases we do not distinguish row and column vectors. The matrix product means that $\mathbf{xUy} = \sum_{i,j}^{N} x_i U_{ij} y_j$ and $\mathbf{xy} = \sum_i^N x_i y_i$, where $\mathbf{x}$ and $\mathbf{y}$ are N-component vectors and $\mathbf{U}$ is an $N \times N$ matrix.

Multiplying both sides by the row vector $\mathbf{e}$ we get

$$J_0 = \frac{\mathbf{eB}(N,1)}{\mathbf{eU}(N,1)\mathbf{f}}.$$

The substitution of J_0 into (A.2) gives

$$J_j = \mathbf{fJ}_j = \mathbf{fU}(j,1)\mathbf{f} \cdot \frac{\mathbf{eB}(N,1)}{\mathbf{eU}(N,1)\mathbf{f}} - \mathbf{fB}(j,1) = \frac{A(N,j,1)}{\mathbf{eU}(N,1)\mathbf{f}}.$$

Taking into account the following identity

$$\mathbf{B}(N,1) \;=\; \mathbf{U}(N,j+1)\mathbf{B}(j,1) + \mathbf{B}(N,j+1)$$

with

$$\mathbf{U}(N,N+1) = 1, \qquad \mathbf{B}(N,N+1) = 0$$

and

$$\mathbf{f} \cdot \mathbf{f}^\top + \mathbf{h} \cdot \mathbf{h}^\top = I$$

we get the expression of $A(N,j,1)$

$$\begin{aligned}
A(N,j,1) &= (\mathbf{fU}(j,1)\mathbf{f})(\mathbf{eB}(N,1)) - \\
&- (\mathbf{eU}(N,1)\mathbf{f})(\mathbf{fB}(j,1)) \\
&= (\mathbf{fU}(j,1)\mathbf{f})(\mathbf{eU}(N,j+1)\mathbf{B}(j,1)) + \\
&+ (\mathbf{fU}(j,1)\mathbf{f})(\mathbf{eB}(N,j+1)) - \\
&- (\mathbf{eU}(N,j+1)\mathbf{f})(\mathbf{fU}(j,1)\mathbf{f})(\mathbf{fB}(j,1)) - \\
&- (\mathbf{eU}(N,j+1)\mathbf{h})(\mathbf{hU}(j,1)\mathbf{f})(\mathbf{fB}(j,1)) \\
&= (\mathbf{fU}(j,1)\mathbf{f})(\mathbf{eB}(N,j+1)) + \\
&+ (\mathbf{eU}(N,j+1)\mathbf{h})(\mathbf{fW}(j,1))
\end{aligned}$$

and thus the equation (4.40). The introduced term $\mathbf{fW}(j,1)$ is given by

$$\begin{aligned}
\mathbf{fW}(j,1) &= (\mathbf{fU}(j,1)\mathbf{f})(\mathbf{hB}(j,1)) - (\mathbf{hU}(j,1)\mathbf{f})(\mathbf{fB}(j,1)) \\
&= (\mathbf{fU}^\top(j,1)\mathbf{f})(\mathbf{hB}(j,1)) - (\mathbf{fU}^\top(j,1)\mathbf{h})(\mathbf{fB}(j,1)) \\
&= \mathbf{fU}^\top(j,1)\sigma\mathbf{B}(j,1),
\end{aligned}$$

where we have used an identity

$$\mathbf{f} \cdot \mathbf{h}^\top - \mathbf{h} \cdot \mathbf{f}^\top \;=\; \sigma.$$

Taking into account the property

$$\mathbf{U}^\top(j,i)\sigma\mathbf{U}(j,i) = \sigma,$$

we have

$$\begin{aligned}
\mathbf{fW}(j,1) &= \mathbf{fU}^{\top}(j,1)\sigma[\mathbf{U}(j,2)\mathbf{K}_1 B_0 + \mathbf{U}(j,3)\mathbf{K}_2 B_1 \\
&+ ...\mathbf{U}(j,j)\mathbf{K}_{j-1} B_{j-2} + \mathbf{K}_j B_{j-1}] \\
&= \mathbf{fW}_1\, B_0 + \mathbf{fU}^{\top}(1,1)\mathbf{W}_2\, B_1 + ... \\
&+ \mathbf{fU}^{\top}(j-1,1)\mathbf{W}_j\, B_{j-1},
\end{aligned}$$

where $\mathbf{W}_j$ is defined in (4.42).

Appendix B

Approximation of $E(t)$

B.1 Stieltjes-Markov method

In order to represent $E(t)$ in equation (5.24) in the form of a finite sum

$$E(t) \approx E_N(t) = \sum_{n=1}^{N} \frac{a_n t}{1 + A_n t} \tag{B.1.1}$$

one can apply the Stieltjes-Markov method (see Perron 1957).

Let us introduce a measure $\phi(dx)$ on interval $[0, 1]$ in such a way that

$$\int_0^1 \phi(dx) f(x) = \frac{2}{\Delta f_\lambda} \sum_{m=0}^{\infty} \frac{1}{1 + y_m^2} \cdot f\left(\frac{1}{1 + y_m^2}\right). \tag{B.1.2}$$

For the approximate evaluation of the integral we use a quadrature formula

$$\int_0^1 \phi(dx) f(x) \simeq \sum_{n=1}^{N} c_n f(x_n) \tag{B.1.3}$$

where x_n are zeros of polynomials of degree N which are orthogonal with respect to $\phi(dx)$, i.e.

$$\int_0^1 \phi(dx)\ P_m(x) P_l(x) = 0 \qquad \text{for} \qquad m \neq l,$$

and the weights c_n are given by

$$c_n = \frac{Q_N(x_n)}{P'_N(x_n)}$$

where $Q_k(x)$ are associated polynomials of degree $(N-1)$

$$Q_k(s) = \int_0^1 \phi(dx) \frac{P_k(s) - P_k(x)}{s - x}.$$

The polynomials $P_k(x)$ can be constructed in the following way. Let us calculate $2N+1$ moments

$$\begin{aligned} m_k(\Delta) &= \int_0^1 \phi(dx) x^k = \frac{2}{\Delta f_\lambda} \sum_{m=0}^{\infty} \left(\frac{1}{1+y_m^2} \right)^{1+k} \\ &= \frac{1}{k!} \left(-\frac{\partial}{\partial v} \right)^k \left. \frac{\tanh\left(f_\lambda \Delta \sqrt{v}\right)}{\sqrt{v}} \right|_{v=1} \end{aligned} \tag{B.1.4}$$

A matrix H with elements

$$H_{ij} = m_{i+j}, \qquad (i,j = 0, ..., N)$$

is symmetric and positive definite. The Cholesky decomposition gives an upper-triangular matrix r with the property that H can be represented as $H = r^\top r$. Then the elements

$$p_{kl} = \left(r^{-1} \right)_{kl}^\top \tag{B.1.5}$$

define the coefficients of the polynomial $P_k(x)$

$$P_k(x) = \sum_{l=0}^{k} p_{kl} x^l.$$

The associated polynomial can be written as

$$Q_k(x) = \sum_{l=0}^{k-1} x^l \sum_{i=l+1}^{k} p_{ki}\, m_{i-l-1}.$$

Let us introduce the notation

$$\begin{aligned} t &= \frac{s}{1+s}, \qquad s = \frac{t}{1-t}, \qquad 0 \le s \le \infty, \\ x &= \frac{1}{1+y^2}, \qquad 0 \le x \le 1, \qquad y = \sqrt{\frac{1-x}{x}}. \end{aligned}$$

Then we have

$$E(t) = \frac{4\beta}{\Delta f_\lambda} \sum_{m=0}^{\infty} \frac{1}{C(iy_m)} \frac{t}{1+y_m^2 t} = \frac{4\beta}{\Delta f_\lambda} \sum_{m=0}^{\infty} \frac{1}{1+y_m^2} \frac{1}{C(iy_m)} \frac{s}{\frac{1}{1+y_m^2} + s}.$$

According to (B.1.2) and (B.1.3) we get

$$\begin{aligned} E(t) &= \int_0^1 \phi(dx) \frac{\beta}{C\left(i\sqrt{\frac{1-x}{x}}\right)} \frac{s}{x+s} \simeq \sum_{n=1}^{N} \frac{c_n \beta}{C\left(i\sqrt{\frac{1-x_n}{x_n}}\right)} \frac{s}{s+x_n} \\ &= \sum_{n=1}^{N} \frac{c_n \beta}{C\left(i\sqrt{\frac{1-x_n}{x_n}}\right)} \frac{t}{x_n + (1-x_n)t}. \end{aligned}$$

Thus the coefficients in (B.1.1) become

$$a_n = \frac{c_n}{x_n} \cdot \frac{2\beta}{C\left(i\sqrt{A_n}\right)}, \qquad A_n = \frac{1}{x_n} - 1. \tag{B.1.6}$$

B.2 "Points method"

The coefficient a_n and A_n of the N-th separable approximation can be found by solving the system of algebraic equations:

$$E_N(t_l) = \sum_{n=1}^{N} \frac{a_n t_l}{1 + A_n t_l}, \quad (l = 1, ..., 2N) \tag{B.2.1}$$

where $\{t_1, ..., t_{2N}\}$ are points from the interval $[0, 1]$. The solution of (B.2.1) can be obtained in the following way. We have

$$\frac{E(t_l)}{t_l} \prod_{k=1}^{N} (1 + A_k t_l) = \sum_{n=1}^{N} a_n \prod_{k \neq n} (1 + A_k t_l). \tag{B.2.2}$$

Let us introduce the notation

$$\begin{aligned} &\prod_{k=1}^{N} (1 + A_k t_l) = \sum_{s=0}^{N} t_l^s u_s, \\ &u_0 = 1, \quad u_s = \sum_{1 \leq i_1 < ... < i_s \leq N} A_{i_1} \cdot A_{i_2} \cdot ... \cdot A_{i_s}, \\ &\prod_{k \neq n}^{N} (1 + A_k t_l) = \sum_{s=0}^{N} t_l^s u_s|_{A_n = 0} = \sum_{s=1}^{N} t_l^{s-1} v_s^{(n)}, \\ &\sum_{n=1}^{N} a_n \prod_{k \neq n} (1 + A_k t_l) = \sum_{s=1}^{N} t_l^{s-1} b_s, \qquad b_s = \sum_{n=1}^{N} a_n v_s^{(n)}. \end{aligned}$$

Then we can write (B.2.2) as the following

$$\sum_{s=1}^{N} t_l^{s-1} b_s - \sum_{s=1}^{N} t_l^{s-1} E(t_l) u_s = \frac{E(t_l)}{t_l}. \tag{B.2.3}$$

Let us introduce $N \times N$- matrices and N-component vectors

$$\begin{aligned} Q^{(1)} &= Q^{(1)}_{ls} = t_l^{s-1}, \qquad H^{(1)} = H^{(1)}_{ls} = t_l^{s-1} E(t_l), \\ Q^{(2)} &= Q^{(2)}_{ls} = t_{N+l}^{s-1}, \qquad H^{(2)} = H^{(2)}_{ls} = t_{N+l}^{s-1} E(t_{N+l}), \\ f^{(1)} &= f^{(1)}_l = \frac{E(t_l)}{t_l}, \qquad f^{(2)} = f^{(2)}_l = \frac{E(t_{N+l})}{t_{N+l}}. \end{aligned}$$

So that the system of linear equations (B.2.3) can be rewritten in a form

$$\begin{aligned} Q^{(1)} b - H^{(1)} u &= f^{(1)}, \\ Q^{(2)} b - H^{(2)} u &= f^{(2)}. \end{aligned} \tag{B.2.4}$$

Eliminating b we obtain the vector $u = (u_1, ..., u_N)$

$$u = \left[(Q^{(1)})^{-1} H^{(1)} - (Q^{(2)})^{-1} H^{(2)} \right]^{-1} \left[(Q^{(2)})^{-1} f^{(2)} - (Q^{(1)})^{-1} f^{(1)} \right].$$

The roots of the following polynomial

$$(-x)^N + u_1 (-x)^{N-1} + ... + u_N = (-1)^N \prod_{n=1}^{N} (x - A_n) = 0$$

correspond to the constants $A_1, ..., A_N$. The last step is the solution of the matrix equation

$$C\, a = f^{(1)}$$

with

$$C_{ls} = \frac{1}{1 + A_s t_l}, \qquad (l, s = 1, ..., N)$$

in order to get the coefficients $a = (a_1, ..., a_N)$.

Bibliography

Abramowitz M., Stegun I. A., 1972, Handbook of Mathematical Functions, Dover Publication Inc., New York

Adam J., 1990, A&A **240**, 541

Adam J., Störzer H., Shaviv G., Wehrse R., 1988, A&A **193**, L1

Auer L. H., Mihalas D., 1970, MNRAS **149**, 65

Bath G. T., Evans W. D., Papaloizou J., Pringle J. E., 1974, MNRAS **169**, 447

Bosma P. B., de Rooij W. A., 1983, A&A **126**, 283

Caldwell J., Perks A. J., 1981, ApJ **249**, 258

Cannizzo J. K., Cameron A. G. W., 1988, ApJ **330**, 327

Cannizzo J. K., Wheeler J. C., 1984, ApJS **55**, 367

Cannon C. J., 1985, The Transfer of Spectral Line Radiation, Cambridge University Press, Cambridge

Chandrasekhar S., 1950, Radiative Transfer, Dover Publication Inc., New York

Chen X., 1995, MNRAS **275**, 671

Efimov G. V., von Waldenfels W., Wehrse R., 1995, J. Quant. Spectrosc. Radiat. Transfer **53**, 59

Efimov G. V., von Waldenfels W., Wehrse R., 1997, J. Quant. Spectrosc. Radiat. Transfer **58**, 355

El-Khoury W., Wickramasinghe D. T., 2000, A&A **358**, 154

Frank J., King A. R., Raine D. J., 1992, Accretion Power in Astrophysics, Cambridge University Press, Cambridge, second edition

Gierens K. M., Traving G., Wehrse R., 1986, J. Quant. Spectrosc. Radiat. Transfer **37**, 361

Gu Y., Jefferies J. T., Lindsey C., Avrett E. H., 1997, ApJ **484**, 960

Haggag M. H., Machali H. M., 1985, Ap&SS **111**, 189

Haggag M. H., Machali H. M., El-Labany S., Attia M. T., 1989, Ap&SS **149**, 13

Herter T., Lacasse M. G., Wesemael F., Winget D. E., 1979, ApJS **39**, 513

Horne K., Marsh T. R., 1986, MNRAS **218**, 761

Hubeny I., 1987, A&A **185**, 332

Hummel W., Vrancken M., 2000, A&A **359**, 1075

Jones P. D., Bayazitoglu Y., 1992, J. Quant. Spectrosc. Radiat. Transfer **48**, 424

Kalkofen W., 1984, Methods in Radiative Transfer, Cambridge University Press, Cambridge

Kalkofen W., 1987, Numerical Radiative Transfer, Cambridge University Press, Cambridge

Kamke E., 1965, Differentialgleichungen, I. Gewöhnliche Differentialgleichungen, Akadem. Verlagsges., Leipzig

Kanschat G., 1996, Ph.D. thesis, Heidelberg University

Kiplinger A. L., 1979, ApJ **234**, 997

Kiplinger A. L., 1980, ApJ **236**, 839

Klein R. I., Castor J. I., Greenbaum A., Taylor D., Dykema P. G., 1989, J. Quant. Spectrosc. Radiat. Transfer **41**, 199

Kurucz R. L., 1979, ApJS **40**, 1

Kříž S., Hubeny I., 1986, Bull. Astron. Inst. Czech. **37**, 129

la Dous C., 1989, A&A **211**, 131

Lin D. N. C., Williams R. E., Stover R. J., 1988, ApJ **327**, 234

Lindsey C., Jefferies J. T., 1990, ApJ **349**, 286

Maier U., 1994, in R. Rannacher, S. Turek, R. Wehrse (eds.), Numerical Methods for Multidimensional Radiative Transfer Problems

Mayo S. K., Wickramasinghe D. T., Whelan J. A. J., 1980, MNRAS **193**, 793

Menshchikov A. B., Henning T., 1997, A&A **318**, 879

Menzel D. H., 1966, Selected Papers on the Transfer of Radiation, Dover Publication Inc., New York

Meyer F., Duschl W. J., Frank J., Meyer-Hofmeister E. (eds.), 1989, Theory of Accretion Disks, Kluwer Academic Publishers

Meyer F., Meyer-Hofmeister E., 1982, A&A **106**, 34

Mihalas D., 1978, Stellar Atmospheres, Freeman, San Francisco, second edition

Mihalas D., Weibel Mihalas B., 1984, Foundation of Radiation Hydrodynamics, Oxford University Press, Oxford

Murray N., Chiang J., 1996, Nature **382**, 789

Narayan R., Yi I., 1994, ApJ **428**, L13

Nasser M. R., Solheim J. E., Semionoff D. A., 2001, A&A **373**, 222

Ng K. C., 1974, J. Chem. Phys. **61**, 2680

Nikoghossian A. G., Pojoga S., Mouradian Z., 1997, A&A **325**, 813

Olson G. L., Auer L. H., Buchler J. R., 1986, J. Quant. Spectrosc. Radiat. Transfer **35**, 431

Papkalla R., 1995, A&A **295**, 551

Peraiah A., 1984, in Methods in Radiative Transfer, ed. W. Kalkofen, 281, Cambridge University Press, Cambridge

Perron O., 1957, Die Lehre von den Kettenbrüchen, Band II, B. G. Teubner Verlagsgesellschaft, Stuttgart

Richling S., Meinköhn E., Kryzhevoi N., Kanschat G., 2001, A&A submitted

Schmidt M., Wehrse R., 1987, in Numerical Radiative Transfer, ed. W. Kalkofen, 341, Cambridge University Press, Cambridge

Schrage J., 1999, Master's thesis, Heidelberg University

Schultz J., 2000, A&A **364**, 587

Schwarzenberg-Czerny A., Rozyczka M., 1977, Acta Astron. **27**, 429

Shakura N. I., Sunyaev R. A., 1973, A&A **24**, 337

Shaviv G., Wehrse R., 1991, A&A **251**, 117

Sonnhalter C., Preibisch T., Yorke H. W., 1995, A&A **299**, 545

Spagna, Jr. G. F., Leung C. M., 1987, J. Quant. Spectrosc. Radiat. Transfer **37**, 565

Steinacher J., Henning T., Menshchikov A., 1997, in D. T. Wickramasinghe, L. Ferrario, G. V. Bicknell (eds.), Accretion Phenomena and Related Outflows, IAU Colloquium 163, Vol. **121**, 807

Stenholm L. G., Störzer H., Wehrse R., 1991, J. Quant. Spectrosc. Radiat. Transfer **45**, 47

Stover R. J., 1981, ApJ **248**, 684

Stover R. J., Robinson E. L., Nather R. E., Montemayor T. J., 1980, ApJ **240**, 587

Turek S., 1993, Imp. Comp. Sci. Eng. **5**, 201

Tylenda R., 1981, Acta Astron. **31**, 127

van der Vorst H. A., 1992, SIAM, J. Sci. Statist. Comput. **13**, 631

Väth H. M., 1994, A&A **284**, 319

Vinsome P. K. W., 1976, in Proceedings of the 4th Symp. on Reservoir Simulations, Soc. of Petroleum Engineers, Boulder, 149

Wade R. A., 1984, MNRAS **208**, 381

Wade R. A., 1988, ApJ **335**, 394

Wehrse R., 1981, MNRAS **195**, 553

Wehrse R., Baschek B., von Waldenfels W., 2000, A&A **359**, 780

Williams G. A., Shipman H. L., 1988, ApJ **326**, 738

Williams R. E., 1980, ApJ **235**, 939

Williams R. E., Ferguson D. H., 1982, ApJ **257**, 672

Wolf S., Henning T., Stecklum B., 1999, A&A **349**, 839

Wood K., Bjorkmann J. E., A. W. B., Code A. D., 1996, ApJ **461**, 828

Young P., Schneider D. P., Shectman S. A., 1981, ApJ **244**, 259

Acknowledgments

I would like to express my sincere gratitude to Prof. Dr. Rainer Wehrse, who supervised this thesis, for his guidance, helpful advices and for leaving me enough freedom to develop the work my own way. I am very grateful to him for many interesting discussions and numerous valuable comments.

Words cannot express my deep thanks to Prof. Dr. Garii Efimov, who gave me the chance to study in Heidelberg, for all his support during these years. I am grateful to him for the guidance and motivations and for all discussions which made the content of this work so interesting.

I thank very much Prof. Dr. Rolf Rannacher for accepting to be the second referee of my thesis.

Many thanks to Katherine Manson for the thorough reading of the manuscript.

I would like to thank all the members of the Institut für Theoretische Astrophysik, especially all those in the group of Prof. Dr. Rainer Wehrse and Prof. Dr. Bodo Baschek for the pleasant work atmosphere.

Special thanks to Dr. Nickolay Dobrodey for his help and valuable advices which made my life in Germany much easier.

I gratefully acknowledge financial support by the Graduiertenkolleg at the Interdisciplinary Center for Scientific Computing at Heidelberg University and by the Deutsche Forschungsgemeinschaft.

And last but not least, I would like to thank my parents and my sister whose support allowed me to work on this thesis.